Distribution Agreement

In presenting this thesis or dissertation as a partial fulfillment of the requirements for an advanced degree from Emory University, I hereby grant to Emory University and its agents the non-exclusive license to archive, make accessible, and display my thesis or dissertation in whole or in part in all forms of media, now or hereafter known, including display on the world wide web. I understand that I may select some access restrictions as part of the online submission of this thesis or dissertation. I retain all ownership rights to the copyright of the thesis or dissertation. I also retain the right to use in future works (such as articles or books) all or part of this thesis or dissertation.

Signature:

_____ _____

Kavinda J. Nissanka Date

Slow geophysical flows of complex particulate matter

By

Kavinda J. Nissanka
Doctor of Philosophy

Physics

Justin C. Burton, Ph.D.
Advisor

Gordon Berman, Ph.D.
Committee Member

Eri Saikawa, Ph.D.
Committee Member

Daniel Sussman, Ph.D.
Committee Member

Eric Weeks, Ph.D.
Committee Member

Accepted:

Kimberly J. Arriola, Ph.D., MPH
Dean of the James T. Laney School of Graduate Studies

Date

Slow geophysical flows of complex particulate matter

By

Kavinda J. Nissanka
B.S., University of Illinois at Urbana-Champaign, IL, 2018

Advisor: Justin C. Burton, Ph.D.

An abstract of
A dissertation submitted to the Faculty of the
James T. Laney School of Graduate Studies of Emory University
in partial fulfillment of the requirements for the degree of
Doctor of Philosophy
in Physics
2024

Abstract

Slow geophysical flows of complex particulate matter

By Kavinda J. Nissanka

The Earth's surface is continuously shaped by the flow of materials. From microns to kilometers, seconds to millennia, geophysical process exist across a vast range of spatial and temporal scales. Seemingly quiet hill slopes and roaring volcanoes are both extremely complex non-equilibrium systems, which intersect with and impact our lives. Understanding the fundamental physics at play in geophysical flows is crucial to predicting, controlling, and responding to these natural phenomenon. This dissertation reports the suite of experiments I have conducted to understand and examine two geophysical flows: the sedimentation of mass-polar spheroids, and the quasistatic flow of the world's largest floating granular material, ice mélange. These systems both contain complex particle shapes and exist in non-inertial regimes, but are driven externally far from equilibrium. Sedimentation is a process that occurs in low Reynolds number flows, and is important in controlling many industrial and terrestrial processes of micron to millimeter sized particles. I report on experimental observations of sedimenting objects which deviate from uniform spheres in such a way as to mimic realistic geophysical particles. I show that a center-of-mass offset changes individual particle dynamics, interparticle interactions, and the distribution of many particles in suspension. On the opposite side of the length scale, ice mélange is a floating conglomeration of icebergs, dirt, and sea ice that sits at the interface between tidewater glaciers and the open ocean in narrow fjords. Because of confinement and jamming, ice mélange can impact the total ice mass flux out of tidewater fjords. I study ice mélange using scaled down laboratory experiments to extract the most salient parameters and features controlling its behaviour. By examining surface velocity fields, thickness profiles, and its buttressing strength, I showcase the importance of friction and particle shape for ice mélange. Importantly, I demonstrate that the force the mélange exerts on the terminus scales as $F \approx H_0^2$, which is the thickness at the terminus. I also show the importance of fluctuations, and the limitations of continuum model's ability to capture these fluctuations. Integration of this knowledge into models of the cryosphere can improve the accuracy of sea level rise predictions. Overall, the phenomena I studied here showcase a wealth of non-equilibrium dynamics, complex particle interactions, and unexpected behaviors.

Slow geophysical flows of complex particulate matter

By

Kavinda J. Nissanka
B.S., University of Illinois at Urbana-Champaign, IL, 2018

Advisor: Justin C. Burton, Ph.D.

A dissertation submitted to the Faculty of the
James T. Laney School of Graduate Studies of Emory University
in partial fulfillment of the requirements for the degree of
Doctor of Philosophy
in Physics
2024

Acknowledgments

Along with the submission of this thesis, I would like to acknowledge those who have played an important role in my Ph.D. career.

First, I would like to express my deepest gratitude to my advisor Professor Justin C. Burton. I could not have asked for a better advisor and role model for these last six years of my scientific career. Justin's patience, kindness, support, and unwavering belief in me has given me the knowledge, confidence, and drive to be the scientist I am today. I've enjoyed our conversations about physics, food, and living a fulfilling life, and I am happy to be able to not only call him my advisor, but also my friend. Justin's ability to motivate and inspire students through his upbeat personality, passion for research, and depth of knowledge has left a lasting impression on me, and the time I have spent with him will be appreciated for the rest of my life.

I'd like to thank the members of my committee, Professors Gordon Berman, Eri Saikawa, Daniel Sussman, and Eric Weeks for their invaluable insights and advice on my research projects. I truly appreciate their thoughtfulness, support, and ability to give pointed and constructive feedback. Their inputs have helped mature my work from fledgling ideas into fully developed scientific works. I would also like to acknowledge several of our collaborators, with whom I've built a strong scientific network. Special thanks to Professors Jason Amundson, Alex Robel, and Ching-Yao Lai, and Doctor Yue Meng for their insightful discussions.

Next, I'd like to thank the many members of the Burton lab, both new and old, for all the help they have provided me, be it in the lab, with writing, or just discussing life: Professor Joshua Méndez-Harper, Doctors Xiaolei Ma, Guga Gogia, Yannic Gagnon, Dana Harvey, and Ran Ranjiangshang. I'd also like to thank the students I had the oppurtunity to mentor for teaching me how to be an effective leader and teacher: Nandish Vora, Mingxuan Liu, and Tony Li.

The friends I have made at Emory and outside have all played an integral part in

my Ph.D. career. While I don't have the space to list all of you, I truly appreciate your support and the good times we've shared together, and each and every one of you holds a special place in my heart.

Finally, and most important of all, I'd like to thank my parents Jayabarathy Kingsley and Kingsley Nissanka, and brother Thehan Nissanka for their love, kindness, encouragement, and unwavering support. Without them, I would have never had motivation to follow my dreams.

Kavinda Nissanka

Emory University, Atlanta, USA

Spring 2024

Contents

List of Figures

List of Tables

Chapter 1

Introduction

1.1 Earth's geophysical flows

The surface of the Earth is continuously shaped by fluid flows across many different shapes, sizes, and speeds. Solid materials are eroded, transformed, transported, and deposited continuously across the terrestrial landscape. Some of the most extreme natural examples of these processes include avalanches, rivers and river deltas (Fig. 1.1a), pyroclastic flows (Fig. 1.1b), tornadoes, hurricanes, landslides, and sandstorms. But even the most mundane system, the ground on which we stand on, holds an abundance of challenging scientific problems. The ground is not a simple single phase material. It is composed of large scale solid matter, such as rocks, and large swathes of ice (whose physical structure can change based on its location and history). These are broken down by a multitude of processes, including biological activity, thermal and capillary stresses, shear from flows of air, water, and gravity, and chemical reactions. The large, solid materials are eroded and torn apart until they become aggregates of grains [3, 6]. Depending on the natural phenomenon, these aggregates can be composed of particles on the micron scale (clay platelets, bacteria, sand) all the way up to particles on the meter to kilometer scale (icebergs, boulders).

As the climate continues to warm and weather patterns continue to fluctuate wildly, our understanding and ability to predict these surface processes will be crucial to the development and safety of our communities [6].

Several different disciplines are connected through the study of the Earth's surface. Engineers creating human infrastructure need to know how their structures are coupled to the dynamics and changes of the landscape. The interplay between humans and the surface we live on is a fundamental tenet of environmental science. For example, Fig. 1.1c showcases the impact of plastic pollution on the most vulnerable communities. The complexity and diversity of particle length scales, compositions, and dynamical timescales provide a wealth of problems for soft matter physics, environmental chemistry, and ecology to investigate. In this work, we will focus on the physics aspects of geophysical flows, namely how do particle shape and strong dissipation influence the manner in which these flows sculpt the Earth's surface. Physics often seeks to unify processes across different scales. Testing geophysical phenomenon in a laboratory provides an exciting opportunity to view some of Earth's most dangerous yet captivating processes in a controlled environment. Often, we seek to take a given phenomenon and break it down into its most essential physical components. For example, do we need our particles to be spherical or does their shape matter? What role does an interstitial fluid play in a given system? How strongly do we need to perturb the system to observe changes in the dynamics? Do we need to match the right temperatures? How about material properties, such as density, tensile strength, or conductivity? These questions and more must be addressed for every experiment. Then we try to model these processes using mathematical tools and approximations, with physical insights and intuition guiding our choices. For geophysical flows, this usually means trying to establish a rheological framework for a given system (how will the system flow in response to external driving), and determining not only what regimes the flows can exist in, but also what parameters can transition the flow from

one to another. These parameters can include particle shape, fluid viscosity, temperature, particle interactions, and external energy inputs. This work examines two geophysical processes, sedimentation of objects who are not uniform in shape or density, and the flows of ice mélange (Fig. 1.1d) in front of marine terminating glaciers. These processes are separated by large temporal and spatial scales, but we can use the versatility of physics to elucidate their impact on the terrestrial landscape.

Sedimentation is a processes that shapes many of Earth's water ground interfaces. The study of sedimentation has a long and storied history, dating all the way back to Stokes in the 1800's [7], where he first described the steady state velocity of small particles falling in a fluid with a large viscosity. As a specific case of particulate transport, sedimentation is concerned with particulates suspended in a fluid (typically water) that are advected by an external flow until gravity drives their settling to a boundary. On Earth's surface, sedimentation is one step in the formation of sedimentary rock and contributes to the evolution of rivers and deltas. Typically, particles are eroded from loose rock or swept along by meltwater from glaciers and transported through the air or water. They eventually settle on the beds of rivers, or exit into large bodies of water through deltas. The loose particles at the riverbeds are turned into sedimentary rock through the process of lithification. Closer to the mouths of rivers, in deltas, estuaries, and mouths, sediments are driven by gravity into deeper waters due to the density difference between the sediment-laden flow and the ambient water [8]. These turbidity currents drive sediments into deeper waters, depositing them on the seafloor or lake beds. An example of these currents can be seen in Fig. 1.1a. The accumulation of particles will alter the landscape of these marine systems. The process of accumulation after particles are advected by the currents occurs within the regime of sedimentation. Predicting, controlling, and monitoring sedimentation rates and amounts is key in combating many environmental risks, such as siltation, flooding, and collapse of coastal ecosystems, which arise from both natu-

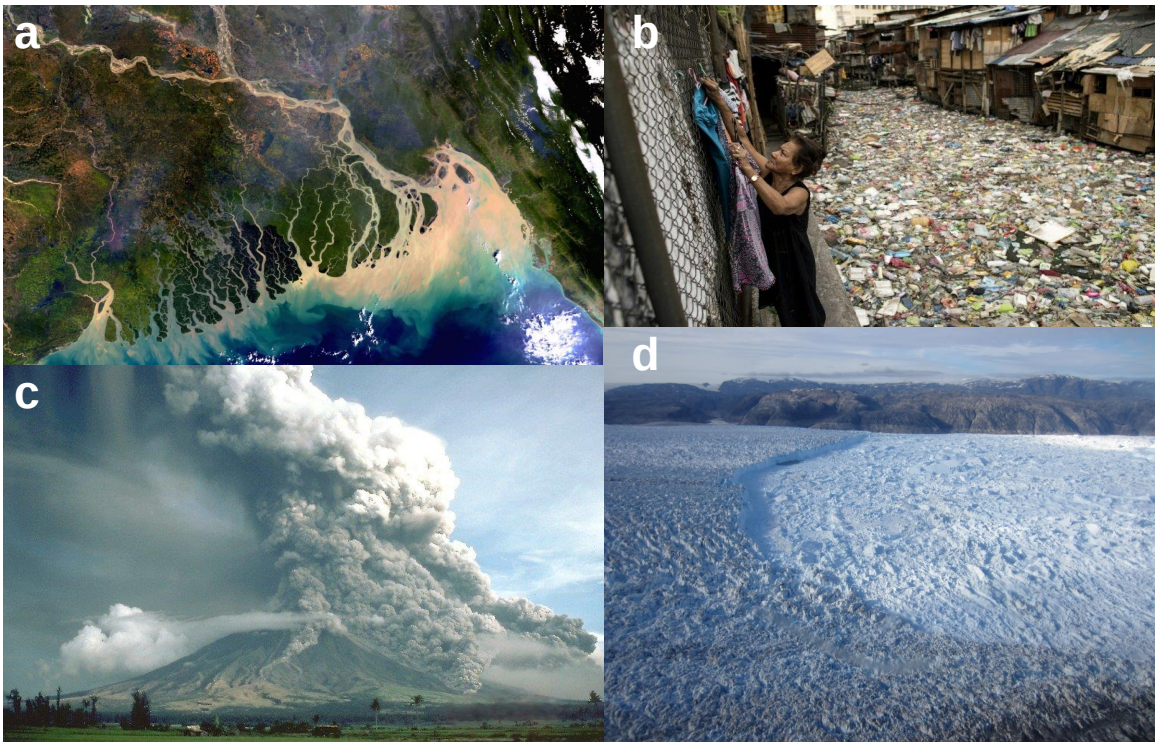

Figure 1.1: Examples of geophysical flows on the Earth's surface. (a) Satellite image of the Ganges-Brahmaputra river delta along Bangladesh's coastline, courtesy of the European Space Agency. Sediment plumes driven by turbidity and gravity currents can be seen extending out into the ocean. (b) A small creek flowing between the makeshift homes of a Manila slum is choked with a thick layer of garbage. Man made pollutants create daily challenges for our most vulnerable communities. (c) Pyroclastic flows of the 1984 Mayon Volcano eruption in the Philippines. Geophysical flows are able to rapidly shape the Earth's surface violently and catastrophically. (d) The interface between a glacier terminus (left) and ice mélange (right) at Helheim glacier in the Sermersooq municipality of Eastern Greenland. On the opposite end of the spectrum from pyroclastic flows, some geophysical flows shape the Earth over much longer timescales.

ral forces and human pollution and interference. Sedimentation has many industrial uses as well, including wastewater treatment, mining, and cell separation [9, 10].

We now move on from the micron to millimeter scale geophysical flows to what is perhaps the world's largest granular material, ice mélange. Created from a polydisperse collection of calved icebergs, sea ice, and brash ice in narrow fjords, ice mélange is part of the pathway for the flux of mass from glaciers to the open ocean. In the world's largest fjords (Sermeq Kujalleq (Jakobshavn Isbræ)), ice mélange can extend for up to 10 km away from the terminus, covers the full 5 km width of the fjord, and is several hundreds of meters deep, with its "grains" ranging in size from several meters to kilometers. Integrating ice mélange into global climate models will give us more accurate estimations on the rates of sea level rise. For perspective, Greenland, where most ice mélange exists, holds approximately 7.2 m of sea level rise in total, and is predicted to release up to 180 mm before 2100. About 30% to 60% of this amount is expected to come from marine terminating glaciers in Greenland, and ice mélange sits right at this interface. The understanding of the feedback loop between mélange and the glacier terminus will give us more accurate predictions on sea level rise. Remote sensing data of ice mélange suggests that it can control the calving rates and freshwater input into fjords [11–17]. Current models take an empirical approach to the effect ice mélange has on glacier termini. They reproduced observed seasonal calving dynamics using models that prescribe periodic changes in the mélange buttressing strength [18–25]. However, this doesn't provide a way to predict the impact of ice mélange from observed data or granular mechanics. Integrating our understanding of granular media into the dynamics of ice mélange will improve the accuracy of our climate models. One might at first try to model ice mélange as an ice shelf, but because of ice mélange's granular nature, there are several characteristics that make it different than an ice shelf. Mélange is porous, which allows water to intrude between the grains. This changes the stress boundary condition at the bottom surface

of the mélange. The intrusion of water also changes the pressure distribution within the system, where gravity and buoyancy dictate that all mélange below the waterline moves up, and all mélange above gets pulled down, leading to a maximum of pressure at the waterline. Finally, because mélange is a conglomeration of grains, it is allowed to jam and rearrange to relieve stresses throughout the system. This modulates the forces it exerts on the glacier terminus over a short timescale, something that continuum ice shelf models cannot capture.

Although the rest of this work will focus on the two previous systems, there are a few interesting phenomenon in other regimes that will help round out this description of geophysical flows. There are phenomenon on the centimeter to meter scale, including pyroclastic flows [26], landslides [6], creeping hill slopes [27], and even ant rafts [28]; systems on the colloidal length scale, like clay and bacterial suspensions, and systems on the kilometer scale, like ice sheets and ice shelves. At the colloidal length scales, there is a coupling between hydrodynamic, chemical, and mechanical forces that leads to low porosity, cohesion, and large yield stresses. Because these are suspensions of fluids, small colloidal particles (10^{-9}–10^{-7} m), and larger sand or silt grains (10^{-6}–10^{-4} m), there is a interplay between multiple length scales that makes it a challenging problem to address. For example, increasing the clay content in sedimentary rocks by 30% leads to a 10^6 fold decrease in the permeability of the rock [29]. Similar to blocking the pores on your skin, this decrease in porosity will change subsurface hydrology, impeding motion of fluid into and out of the material. Geophysical flows on the centimeter to meter scale are commonly studied in the regime of near criticality, where they are far from equilibrium and can access different physical regimes through tuning their temperature, stresses, and densities. Landslides occur when the soil loses its rigidity, which stems from a decrease in its volume fraction. Pyroclastic flows, fast moving hot turbulent mixtures of rocks, gases, and ash that come from volcanic eruptions show remarkably complex dynamics, again due to the

interplay between many length scales and being near criticality. Ice sheets and ice shelves demonstrate the interplay between timescales, where they move as viscous fluids over large timescales, but are brittle and and fracture like a solid material on short timescales. Geophysical flows are exciting because they exist across a wide variety of temporal and spatial scales, and exhibit behaviours in several different physical regimes.

1.2 Non-inertial flow regimes

Many processes on the Earth's surface exist over long timescales, such as erosion and deposition of sediments, the movement of glaciers, and the creep of hill slopes. Long timescales allow for the relaxation and dissipation of energy throughout the system, causing inertial, or momentum based, effects to be dampened out. The constituent pieces of these systems are typically in a force balance. In general, forces in the system come from the deformations of the fluid or continuum material, the inertia of the fluid, and external body forces. Assuming the conservation of mass and momentum, we can write a generic set of equations for flowing and deforming materials:

$$\nabla \cdot \boldsymbol{v} = 0, \tag{1.1}$$

$$\nabla \cdot \boldsymbol{\sigma} + \boldsymbol{F}_{ext} = \rho \left(\frac{\partial \boldsymbol{v}}{\partial t} + \boldsymbol{v} \cdot \nabla \boldsymbol{v} \right). \tag{1.2}$$

where $\boldsymbol{\sigma}$ is the *stress tensor* of the material, which describes the magnitudes and directions of stress (force per unit area) in the material, $\boldsymbol{F}_{ext}$ are any external body forces acting on the material, ρ is the density of the material, and $\boldsymbol{v}$ is the velocity of the material. The stress tensor is a second order tensor with nine components. Each component σ_{ij} can be visualized as the stress pointing along an axis x_j on the surface with normal vector pointing in the direction x_i on a infinitesimal cube of material. The right hand side is typically called the *material derivative*, and (in this

case) describes how the momentum of the system is carried by the flow. We can expand the stress tensor into two quantities, $\boldsymbol{\sigma} = -P\boldsymbol{I} + \boldsymbol{\tau}$, known as the pressure ($P = -\frac{1}{3}\mathrm{Tr}(\boldsymbol{\sigma})$) and the deviatoric stress ($\boldsymbol{\tau}$). Pressure captures the total normal stresses in the material, while the deviatoric tensor captures the shear stresses and deformations. We make this transformation because pressure is typically a relevant quantity of interest, and the deviatoric stress can be tailored to express the unique qualities of different continuum materials/fluids. Making this substitution will also allow us to make clearer parallels to our systems of interest. Equation 1.2 then becomes:

$$-\nabla P + \nabla \cdot \boldsymbol{\tau} + \vec{F}_{ext} = \rho \left(\frac{\partial \boldsymbol{v}}{\partial t} + \boldsymbol{v} \cdot \nabla \boldsymbol{v} \right) \tag{1.3}$$

To make this equation usable for a specific system, one has to identify the constitutive relationships for the pressure and deviatoric stress tensor. For most fluids in terrestrial water systems, we can assume that they are incompressible viscous Newtonian fluids, which implies the following properties of the stress tensor: it is Galilean invariant, it is isotropic, and its velocity obeys Eq. 1.1. Galilean invariance stipulates the tensor must be the same in any inertial reference frame. This means only spatial derivatives of the flow velocity enter into the stress tensor, $\nabla \boldsymbol{v}$. Isotropy implies that the stress tensor looks the same no matter your orientation in the fluid. The first order object that we can write down that has these properties is the strain rate tensor, $\dot{\boldsymbol{\epsilon}} = \frac{1}{2}\left(\nabla \boldsymbol{v} + \nabla \boldsymbol{v}^T\right)$. So, we build a constitutive equation of the form $\boldsymbol{\tau} = 2\eta\dot{\boldsymbol{\epsilon}} = \eta\left(\nabla \boldsymbol{v} + \nabla \boldsymbol{v}^T\right)$. Here, η is the material's resistance to deformations and flow, which we define as the dynamic viscosity of the material. Substituting this expression into Eq. 1.3 and simplifying, we arrive at the well known *Navier-Stokes* equation:

$$-\nabla P + \eta \nabla^2 \boldsymbol{v} + \boldsymbol{F}_{ext} = \rho \left(\frac{\partial \boldsymbol{v}}{\partial t} + \boldsymbol{v} \cdot \nabla \boldsymbol{v} \right). \tag{1.4}$$

Non-dimensionalization of the equation extracts a parameter which is helpful in identifying flow regimes, called the Reynolds number. The Reynolds number, Re, describes the ratio of inertial forces within the fluid to the effect of viscous damping, and is typically written as $Re = \frac{\rho v R}{\eta}$. Here, R is a characteristic length scale in the system, which in this context will be the size of a particle immersed in the flow. First discovered and used by Osborne Reynolds in 1883 [30], the Reynolds number divides the flow regimes of incompressible fluids into three major regimes; Stokes flow ($Re \ll 1$), laminar flow ($Re \sim 10 - 1000$), and turbulent flow ($Re \gg 1000$), the exact numbers for laminar and turbulent flow are dependent on the specific geometry of the system. If the flow is within the Stokes regime, then the right hand side of Eq. 1.4 becomes zero. This gives us the governing equations for incompressible, Newtonian fluids in Stokes flow (alternatively called low Reynolds number flow):

$$\nabla \cdot \boldsymbol{v} = 0, \tag{1.5}$$

$$\eta \nabla^2 \boldsymbol{v} + \boldsymbol{F}_{ext} = \nabla P. \tag{1.6}$$

Sediment particles in terrestrial waterways are found within the length scale of 10^{-5}–10^{-3} m [31]. Using the values for water, $\rho = 1000$ kg/m^3, $\eta = 8.9 \times 10^{-4}$ Pa·s, and using the measured velocities of sediment laden river delta flows [32] of approximately $v = 0.2$ m/s, we get a $Re \approx 1$–10. This is generally higher than typical Stokesian dynamics Reynolds numbers, however this is assuming the particles are always moving at the speed of the river itself. During settling, particles may not be advected by the flow, and instead fall with their terminal velocity. Chapter 2 will discuss the derivation of the Stokes velocity, and for a typical aggregate of rock with density ~ 2000 g/cm^3, the terminal velocity would be $v \approx 2.5 \times 10^{-4}$ m/s, giving us a Reynolds number of $Re \approx 10^{-3}$, which is squarely in the Stokes regime.

Objects in low Reynolds number flows create fluid disturbances that fall off as $1/r$,

where r is the distance from the center of mass of the object. Typically, sphere-like objects (spheroids) are expected to sediment at a constant velocity and angle [33]. However, when groups of spheres sediment, mutual drag reduction allows some to speed up and drift closer to others, forming large clumps, or density variations. Theories and experiments differ because experiments typically observe an upper bound on the size of these velocity fluctuations, while the simple theory predicts no upper bound. This is commonly referred to as the Caflisch-Luke paradox, and is an on going problem of interest in sedimentation [34]. There are several proposed mechanisms that screen out velocity fluctuations in real systems, which include wall effects at the size of the experimental container [35], correlated particle positions arising from a pre-imposed structure factor [36, 37], polydispersity [38], stochasticity in the concentration [39], stratification [40], or shape effects [41–47]. Shape effects are of particular interest because they change the interactions between particles locally. For instance, many particles in river sediments are conglomerate rocks [48], and it has been shown that conglomerates of uniform spheres experience a different amount of drag than a single sphere [49]. This discussion is continued in section 1.3.

While granular materials are made of solid particles, the collective motion of the grains evokes the image of fluid like behaviour. This suggests that we might be able to use the same framework of Eq. 1.3 in creating granular flow models. However, the assumptions and form of the deviatoric stress tensor must be adjusted to reflect the physical properties of granular matter. Previously, we used a stress tensor form that is applicable for incompressible viscous Newtonian fluids. For our purposes, we assume granular flows are incompressible because we are typically dealing with dense granular systems. There exist generalized Newtonian fluids, where the stress and strain rate have the following relationship: $\boldsymbol{\tau} = \mu_{\text{eff}}(\dot{\boldsymbol{\epsilon}})\dot{\boldsymbol{\epsilon}}$, where μ_{eff} is an effective viscosity that depends on the strain rate. This generalization is robust enough to characterize several other types of fluids, such as power-law fluids, shear-thinning

or shear-thickening fluids, and Bingham fluids [50]. Viscous behaviours are used for materials that are flowing, but at low stresses, granular materials have been shown to have a solid like, linear elastic response to external forcing [51]. Linear elastic materials behave like springs, and are only dependent on the amount of *strain*($\boldsymbol{\epsilon}$) not the strain rate ($\dot{\boldsymbol{\epsilon}}$). The constitutive relation between stress and strain can be derived from Hooke's law, and is $\boldsymbol{\sigma} = 2\mu\boldsymbol{\epsilon} + \lambda \mathrm{Tr}(\boldsymbol{\epsilon})\boldsymbol{I}$, where μ and λ are material constants called elastic moduli or *Lamé coefficients*. Materials can also deform like a plastic, where they act like elastic materials at low stress, but then there is a sudden, irreversible deformation after their yield stress has been overcome. The three rheological frameworks can even be combined to describe viscoplastic (ketchup, toothpaste), viscoelastic (tendons and ligaments), or elastoplastic (most solids can take some deformation before being irreversibly broken) materials. For granular materials, they can withstand small deformations and hold their shape, but after a certain stress threshold is reached, they start to flow like a fluid. Thus, rheological models often use a viscoplastic rheology to describe granular materials, which assume the following form for the constitutive relation:

$$\boldsymbol{\tau} = \mu P \frac{\dot{\boldsymbol{\epsilon}}}{\dot{\boldsymbol{\epsilon}}_e} \tag{1.7}$$

where μ is now an effective coefficient of friction that is generally a function of the strain rate, and $\dot{\boldsymbol{\epsilon}}_e = \sqrt{1/2\left(\mathrm{Tr}(\dot{\boldsymbol{\epsilon}})^2 - \mathrm{Tr}(\dot{\boldsymbol{\epsilon}} \cdot \dot{\boldsymbol{\epsilon}})\right)}$ is the second invariant of the strain rate tensor. Viscoplastic rheologies have been used to describe a wealth of granular phenomenon [12, 52–57]. Finally, although we have have used the same continuum mechanical framework to connect these two disparate types of flows (sedimenting particles vs. floating granular materials), there are still major differences in how they are applied. For one, in sedimentation, we are concerned with the movement of particles suspended in a fluid, and so the continuum equations exist to give a

description of the forces the fluid applies to the particles, which we then use to build a model for the particle's motion. In quasistatic floating granular materials, we again have particles submersed in a fluid, however now the continuum model describes the behaviour of the grains, and the fluid's impact is limited to buoyant effects. As well, the dissipation of energy in sedimentation is mediated by the fluid and the drag it imparts on the particles, while in granular materials, it is the particle contact forces that provide the mediation.

Like fluids, granular materials also exhibit transitions between different dynamical regimes. The simplest way to imagine this is with sand in a bucket. As the grains of sand sit in a bucket, you can place an object on them and they will support the load without letting the object sink. But then you can tilt the bucket and the sand flows out of it like a fluid. The macroscopic behaviour of the material changed from something akin to a solid that can bear load, to a flowing fluid, without adjusting any microscopic parameters. So what changed in the material? The transition between these two behaviours is theorized to be a gradual change brought on by increasing the amount of external drive, whether that is shear rate, thermal activity, biological activity, or chemical reactivity [27, 55, 58–60]. Typically, a ratio between the timescale of macroscopic shear, $\dot{\gamma}^{-1}$ and the timescale of microscopic rearrangements, $I = \dot{\gamma} d \sqrt{\rho/P}$ is used to differentiate between the two regimes (here d is the grain size, ρ is the density of a constituent particle, and P is the pressure [59, 61]. Historically, the first studies found the transition from fluid like to quasistatic to lie in the range $I < 10^{-3}$–10^{-2}. The constitutive law based on the inertial number is the $\mu(I)$ rheology [52], and is a type of viscoplastic rheology (Eq. 1.7). The $\mu(I)$ rheology can quantitatively predict flows and stresses for granular flows above a yield stress criterion of the friction $\mu = \mu_s$, below which they predict zero motion within the material. However, granular materials still flow under the yield criterion, especially where there exists spatial or temporal inhomogeneity in the flow [27, 55, 58, 59, 62–65]. This regime is called

quasistatic granular flow, and for this work can be seen as an analog to Stokes flow in sedimentation. This regime is defined by the independence of stress to the shear rate, the divergence of interaction length scales, and an exponentially decaying shear rate profile whose decay length scales with the sizes of grains [58, 64, 65]. This decay is analogous to the instantaneous diffusion of momentum in Stokes flow, and creates the potential for long range effects within the system [59, 65]. There have been recent efforts to address the inconsistency of the $\mu(I)$ model by the introduction of an order parameter which describes how "fluid-like" the material is behaving [60, 66–68]. In general, the fluidity order parameter is assumed to follow diffusive dynamics, and whose value is tied to the rheology. The fluidity tries to tie together the fact that each regime has a different source of fluctuations. In the inertial regime, the flow of particles themselves generates the fluctuation locally [64]. In the quasistatic regime, the source of fluctuations come from the boundaries of the material instead [59, 69]. The boundaries are either at the confining walls of the system, or at the point of transition from quasistatic to inertial. Again, similar to low Reynolds number flows, the negligible effects of inertia in these "slow" materials means interactions at the boundaries (particle-fluid for sedimentation, and the previously mentioned boundaries for granular materials) are propagated throughout the system. Real geophysical flows are abound with interfaces between solid materials, water, air, and organic materials. Thus, the importance of understanding how these boundaries are coupled with the large scale behaviour of these flows cannot be understated.

1.3 Complex particles

When modelling geophysical flows from the grain scale, the natural starting point is to consider spherical, mono-disperse collections of particles as the constituents of the system. However, we know that real geophysical flows are anything but homogeneous,

uniform spheres [49, 70–73]. In Fig. 1.2a we see the sizes and shapes of sediments within Earth's terrestrial waterways. The wide breadth of sediment types and sizes makes it clear that the approximation of mono-disperse spheres is far from reality. Figure 1.2b shows an overhead view of icebergs in Sermilik Fjord, Greenland. The iceberg size varies on the order of 100s of meters, and their shapes are rough and jagged. It is this rough and jagged texture that allows the ice to interlock with each other and jam in fjords, applying a back stress onto the terminus of glaciers and inhibiting the calving of new icebergs. Particles also do not only interact with themselves. Geophysical flows are inherently multi-phase, and the interactions particles have with these flows is highly dependent on their shape (Fig. 1.2c). The shape and size distributions will change particle trajectories, fluid disturbances, inter-particle interactions, and their response to external stresses [41–47, 74–77]. But the amount of information needed about particle shapes are not equal across all systems. We seek to understand the salient shape and composition features which will give us the simplest model that describes a given phenomenon. For instance, during sedimentation, the linearity of the Stokes equation (Eq. 1.6) allows us to write down a linear relationship between the forces and velocities of an object in the fluid. More concretely, given the body forces and torques ($\vec{F}$ and $\vec{\tau}$) on the object, we can recover its velocities and angular velocities ($\vec{v}$ and $\vec{\omega}$) by:

$$\begin{pmatrix} \vec{v} \\ \vec{\omega} \end{pmatrix} = \begin{pmatrix} \boldsymbol{T}_{vF} & \boldsymbol{T}_{v\tau} \\ \boldsymbol{T}_{\omega F} & \boldsymbol{T}_{\omega\tau} \end{pmatrix} \begin{pmatrix} \vec{F} \\ \vec{\tau} \end{pmatrix}. \tag{1.8}$$

Here we've written down four sub-matrices that are solely dependent on the shape and mass distribution of the particle. These matrices, when taken together, are typically called the mobility matrix of a particle. In essence, they are similar to the Stokes drag formula, which determines the drag force felt by an object given its velocity, $\vec{F}_d = 6\pi\eta R\vec{v}$. The mobility matrix expands on this concept, and encapsulates both

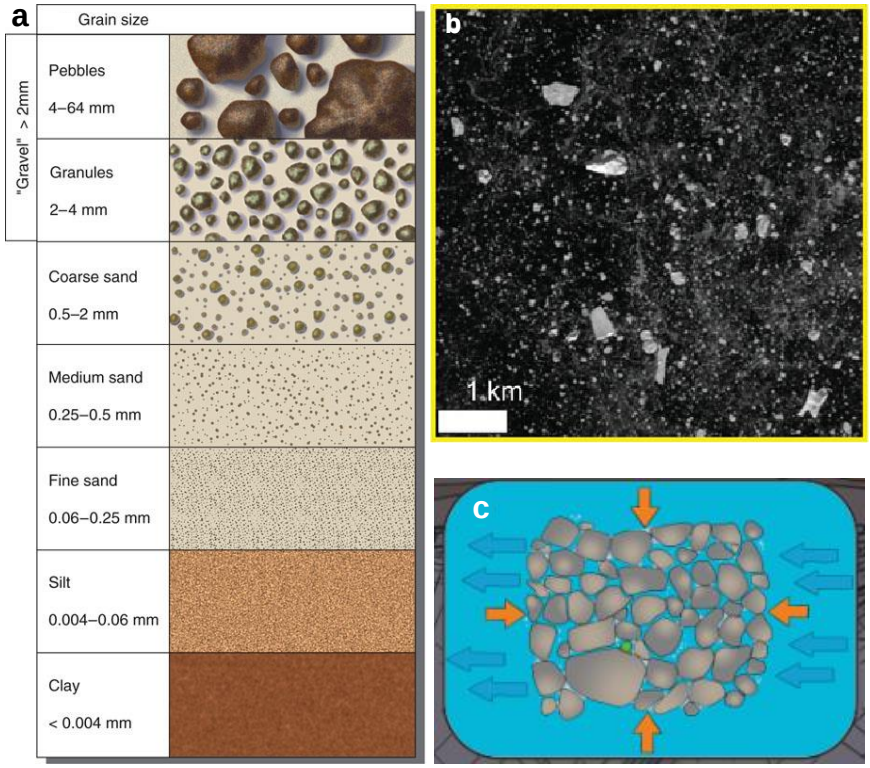

Figure 1.2: Examples of particle shape and size disparity in geophysical systems. (a) Classification of grain sizes in river sediments, most being within the Stokes limit. Adapted from the National Park Service [1]. (b) Satellite image of icebergs in Sermilik Fjord, Greenland, adapted from [2]. White shapes are icebergs, black is the surrounding water of the fjord. (c) Shows the interplay between particle shapes and sizes (grey shapes), external stresses (orange arrows), and external and interstitial flows (blue arrows), adapted from [3]. Earth's surface is composed of multiple phases, dimensions, scales, and processes.

translational and rotational drag, as well as any anisotropies in the particles shape, such as chirality or a non-uniform mass distribution. This governing equation leads to all sorts of complex behaviours, such as chaotic trajectories and Keplerian orbits [43, 78–82]. Chapter 2 will go over how a simple change to the mass density of a particle changes both its individual dynamics and the interaction between particles in a suspension, leading to uniform sediment layers.

Constitutive particles in granular geophysics are more likely to be jagged, polydisperse, and an aggregate of materials of different densities [49, 71–73]. However, modeling and experiments have been done on uniform, mono-disperse, spherical par-

ticles. While these are great parameters for establishing the baseline dynamics of granular materials, complex particle shapes and heterogeneous distributions of size and composition will change a host of macroscopic behaviours, such as the nature of the transition between quasistatic and inertial flows, the magnitude of fluctuations, yield stress, packing fraction, and viscosity [74, 83–87]. In chapter 3, we study the slow advance of a glacier terminus as it pushes ice mélange, the worlds largest granular material, through a rugged fjord. Laboratory techniques are used to mimic real world fjords, allowing us to measure and model previously unseen physical aspects of the mélange, such as its depth profile and time evolution of its terminus buttressing strength. The shape of the constituent particles in the mélange were observed to control the interactions with the boundary, which we saw can influence the flow regimes of granular materials in section 1.2.

Chapter 2

Sedimentation of Mass Polar Spheroids

This chapter is adapted from my previously published paper [88].

2.1 Background

Sedimentation is a longstanding and important problem in fluid dynamics. In its simplest form, particles far from equilibrium settle in a fluid through some external forcing, typically gravity, at low Reynolds number [7]. Throughout its storied history, one can observe a microcosm of physics problems that span multiple fields. Starting from basic hydrodynamics, the long range velocity fields generated by sedimenting particles lead to several interesting phenomena [7, 33, 78, 89, 90]. Examples include unbounded velocity fluctuations [34], chaotic behavior [78, 79], and periodic orbits [43, 80–82]. Sedimentation is found throughout nature; from silt and sand in a river, to biogenic particles in the ocean [91]. Most sedimentation work has been done on uniform particles or particles with simple symmetries. But within nature, most particles are not uniform. They can be rough and polygonal, and they can be made of many different materials, causing their mass to be distributed non-uniformly [73]. For

example, it has been found that some phytoplankton adjust their center of mass to respond to external environmental flows for better survival in turbulent environments [10].

Gravitational sedimentation at low Reynolds number (Stokes flow) is a special case of the Navier-Stokes equation where inertia is negligible. Because of this, Stokes flow is quasistatic and time reversible. For a single spherical particle of radius R and density ρ_p settling in an unbounded fluid of density ρ_f and viscosity η, balancing the Stokes drag force with gravitational and buoyant forces leads to the following expression for the steady state terminal velocity:

$$U_T = \frac{2}{9}\frac{\rho_p - \rho_f}{\eta} g R^2. \tag{2.1}$$

Here g is the gravitational acceleration. The addition of many other particles in the fluid complicates this picture. To leading order, the fluid disturbance at a distance r from a sedimenting sphere with velocity U_s and radius R scales as $U_s R/r$. In sedimenting suspensions of many particles, these long range hydrodynamic interactions complicate a local description of particle dynamics. Batchelor solved the problem of a diverging mean sedimentation velocity [92], but Caflisch and Luke pointed out that the velocity *fluctuations* were still unbounded as the system size increases [34].

To illustrate the Caflisch-Luke paradox, consider the variance of the sedimentation velocity of a group of N particles contained in a volume of size L. The volume fraction ϕ of particles is NV_p/L^3, where $V_p = \frac{4}{3}\pi R^3$ is the volume of a single particle. Within this region, if the particles are randomly and independently distributed, the fluctuation in particle number is simply $\sqrt{N}$. To find the velocity fluctuations, we can balance the total change in the Stokes' drag force over the suspension with the change in gravitational and buoyant forces due to these number fluctuations: $6\pi\eta L\Delta v \approx (\rho_p - \rho_f)V_p g\sqrt{N}$. Solving for Δv, we arrive at the fractional change in velocity,

$\Delta v/v_o = L^{1/2}\sqrt{\phi R^2/V_p}$. This would indicate that the velocity fluctuations depend on the system size, L. Simulations agree with these predictions in unbounded fluids [40, 93–97], while experiments generally observe a limit to the size of the fluctuations [89, 98–100].

To reconcile this paradox, several different physical mechanisms have been proposed. The long-ranged interactions must be screened out by some large length scale, or by changing the interactions themselves. For example, wall effects at the size of the experimental container [35], correlated particle positions arising from a pre-imposed structure factor [36, 37], polydispersity [38], stochasticity in the concentration [39], stratification [40], or shape effects [41–47]. The latter example is of particular interest since it is a local change to particle interactions. Shape effects can be captured within Stokes flow using a response matrix that only depends on particle geometry and couples to external forces and torques.

We start by considering the Navier-Stokes equation for an incompressible fluid in the low Reynolds number regime:

$$\vec{\nabla} P = \eta \vec{\nabla}^2 \vec{\mathbf{v}} + \vec{\mathbf{f}}_b, \tag{2.2}$$

$$\vec{\nabla} \cdot \vec{\mathbf{v}} = 0, \tag{2.3}$$

where P is the pressure, η is the dynamic viscosity, $\vec{\mathbf{v}}$ is the velocity field, and $\vec{\mathbf{f}}_b$ are any body forces per unit volume on the fluid, such as gravity. The linearity of these equations allows us to write the equations of motion for a single particle suspended in the fluid and subjected to an external force or torque as:

$$\vec{v}(t) = \boldsymbol{T}_{vF} \cdot \vec{F} + \boldsymbol{T}_{v\tau} \cdot \vec{\tau}, \tag{2.4}$$

$$\vec{\omega}(t) = \boldsymbol{T}_{\omega F} \cdot \vec{F} + \boldsymbol{T}_{\omega\tau} \cdot \vec{\tau}, \tag{2.5}$$

which can be written in matrix form as:

$$\begin{pmatrix} \vec{v} \\ \vec{\omega} \end{pmatrix} = \begin{pmatrix} \boldsymbol{T}_{vF} & \boldsymbol{T}_{v\tau} \\ \boldsymbol{T}_{\omega F} & \boldsymbol{T}_{\omega\tau} \end{pmatrix} \begin{pmatrix} \vec{F} \\ \vec{\tau} \end{pmatrix}. \tag{2.6}$$

Here $\vec{\omega}$ is the angular velocity of rotation about the center of geometry, $\vec{F}$ and $\vec{\tau}$ are the external forces and torques, respectively. The convention we use is the same as Witten and Diamant [42]. The shape dependent $\boldsymbol{T}$ matrices couple the velocities of the particle to external forces and torques. In the fixed lab frame, the matrices depend on the particle's orientation to the imposed flow. We can also put restrictions on the matrices by physical insight. The dissipated power of the object, $\vec{F} \cdot \vec{v} + \vec{\tau} \cdot \vec{\omega}$, must be positive, which implies the diagonal blocks, $\boldsymbol{T}_{vF}$ and $\boldsymbol{T}_{\omega\tau}$ must be symmetric, and $\boldsymbol{T}_{v\tau}$ and $\boldsymbol{T}_{\omega F}$ must be transposes of each other but not necessarily positive or symmetric. Taken together, these matrices comprise the *mobility matrix* $\boldsymbol{T}$ of an object. If you invert the relation, the matrix is called the resistance matrix. As an illustration, for a uniform sphere in an unbounded fluid, the mobility matrix is:

$$\begin{pmatrix} \vec{v} \\ \vec{\omega} \end{pmatrix} = \begin{pmatrix} \frac{1}{6\pi\eta R}\delta_{ij} & 0 \\ 0 & \frac{1}{8\pi\eta R^3}\delta_{ij} \end{pmatrix} \begin{pmatrix} \vec{F} \\ \vec{\tau} \end{pmatrix}, \tag{2.7}$$

where δ_{ij} is the Kronecker delta.

The dynamics of a single particle are determined by the time evolution of $\boldsymbol{T}$. As the particle moves through the fluid, its orientation can change with respect to the center of mass velocity. The orientation of the particle relative to the force determines what $\boldsymbol{T}$ looks like in the lab frame. Analogously, if we move to the body frame of the particle, $\boldsymbol{T}$ becomes fixed and the force and torque become time dependent. The motion of the particle cannot change the magnitude of the force, so only the force's direction changes with time. Depending on the symmetries of $\boldsymbol{T}$, different

classes of trajectories can be found. For a comprehensive list of these trajectories and symmetries, refer to Doi and Makino [46], Krapf et al. [45], and Witten and Diamant [42].

In the case of gravitational sedimentation, asymmetric particles with mass distribution polarity will undergo rotation in response to external forcing [42]. This is because the total form and skin drag on the particle can apply a net torque when the center of mass is in a different location than the geometric center of the particle. Consequently, an external force leads to a net torque, and the particle will rotate so that the external force is parallel to an eigendirection of $\boldsymbol{T}_{\omega F}$ [42]. The response of a single particle can have important implications for the sedimentation dynamics of many particles. Recent work has theoretically explored the sedimentation of "mass polar" prolate spheroids, whose center of mass lies along the major axis away from the geometric center [41]. These particles are defined by two parameters: the ratio of major to minor axes, κ, and the center of mass offset from the geometric center, χ. Using a linear stability analysis of a uniform suspension of particles in Stokes flow, they predicted a repulsive interaction for $\kappa > 1$ (prolate), and an attractive interaction for $\kappa < 1$ (oblate). The effect is surprisingly enhanced for smaller values of χ. These effects, over a large collection of particles, can either enhance particle clustering and velocity fluctuations ($\kappa < 1$), or inhibit them ($\kappa > 1$).

Inspired by Goldfriend et al. [41, 101, 102], we experimentally tested these predictions by fabricating prolate, mass polar "dimers" and "trimers." The particles were composed of multiple spheres of varying materials bonded together. Our experiments tracked the position and rotation of pairs of particles in a quasi-2D environment. First, we examined the motion of single particles in order to quantify the mobility matrix. Using the symmetry properties of prolate spheroidal particles, we derive an analytic solution for the particle dynamics that shows excellent agreement with the experimental data. Then, by sedimenting pairs of particles in the same quasi-2D

environment, we found that prolate particles experienced an effective repulsion that increased with κ and decreased with χ, in agreement with Goldfriend et al. [41]. Finally, we sedimented hundreds of particles in a 3D container and analyzed the distribution of their post-sedimented positions. The inherent repulsion manifested as wider spatial distributions of particles on the floor of the experimental apparatus. This shows local changes in particle interactions have a large effect on global sedimentation patterns.

2.2 Experimental Methods and Particle Fabrication

Composite particles were fabricated by gluing together smooth ball bearings using a cyanoacrylate based glue. Each sphere had a diameter of 2 mm, and the material and mass density of each sphere were chosen to produce various numerical values of χ. We used the minimal amount of glue possible to adhere the spheres by applying a low-viscosity glue instead of a viscous glue. The remaining thin layer of glue that extended away from the contact point possibly affected the motion of the sedimentation of the particles, but the repeatability of the experiments indicates that this has only a minimal effect. The materials used were aluminum, stainless steel, copper, tungsten carbide, zirconium dioxide, and Delrin. Spheres were glued in either a dimer ($\kappa = 2$) or linear trimer ($\kappa = 3$) configuration. The accessible range of χ was 0.0-0.43. To analytically calculate χ for any linear chain of n spherical particles, we assumed all particles were "light" with density ρ_l except for a single "heavy" particle with density ρ_h positioned at the end of the chain. The result is:

$$\chi = \frac{1}{n}\frac{(n-1)|\rho_h - \rho_l|}{\rho_h + (n-1)\rho_l}, \quad n \geq 2. \tag{2.8}$$

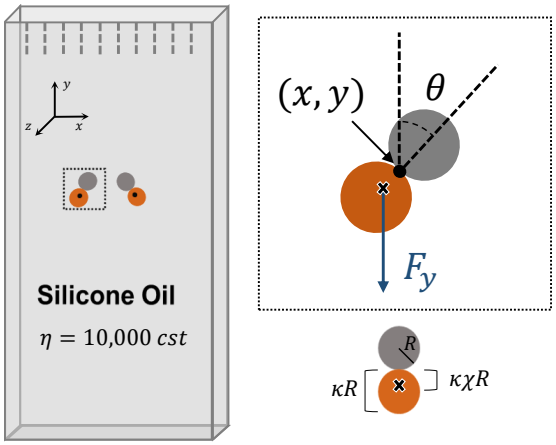

Figure 2.1: Schematic diagram of our quasi-2D experimental setup. The tank dimensions are 19 cm × 15 cm × 0.4 cm. The top of the tank has a gating mechanism that allowed us to drop multiple particles simultaneously. The mechanism consists of a slotted piece of acrylic and a metal rod in a U shape. By moving the prongs of the rod, the horizontal part can be rotated out of the plane, releasing the particles simultaneously. The schematic on the right depicts a $\kappa = 2$ composite particle and coordinates in the lab frame. θ is defined as the angle between the composite particle's major axis and the vertical direction. The orange sphere has a larger mass density in this case, so the center of mass is shifted away from the center of geometry (black cross) to the position indicated by the black cross. On the bottom right, a physical representation of κ and χ is shown on an example particle. The center of mass of the particle is offset by an amount $\kappa\chi R$. For all our experiments, $R = 1$ mm, and the typical Reynolds number was $\sim 10^{-4}$.

The center of mass is displaced by a distance $\kappa\chi R$, for a physical representation of κ and χ, see Fig. 2.1.

Two sets of experiments used a quasi-2D tank made out of cast acrylic (Fig. 2.1). We laser cut sheets of cast acrylic and used SCIGRIP® 4 acrylic plastic cement to glue them together to create a tank of dimensions 19 cm high, 15 cm wide, with a gap of thickness 4 mm. The tank was filled with pure silicone oil of kinematic viscosity 10,000 cSt and density of 0.971 g/cm^3. A gating mechanism was placed at the top of the chamber consisting of a thin rectangle of acrylic with 2.5 mm holes spaced out evenly. The holes helped to align the particles so that the initial orientations are fixed before sedimentation. A thin metal rod held them in place and facilitated a simultaneous release of the particles at the beginning of an experimental run.

Material Combinations	ρ_l (g/cm^3)	ρ_h (g/cm^3)	κ	χ
St+St	7.82	7.82	2	0
Cu+St	7.82	8.92	2	0.033
St+ZrO_2	5.68	7.82	2	0.080
Cu+ZrO_2	5.68	8.92	2	0.11
Al+Pl	1.42	2.79	2	0.16
Tc+St	7.82	15.63	2	0.17
St+Al	2.79	7.82	2	0.24
Cu+Pl	1.42	8.92	2	0.36
Cu+St+St	7.82	8.92	3	0.030
Tc+Cu+Cu	8.92	15.63	3	0.11
St+Al+Al	2.79	7.82	3	0.18
Cu+Pl+Pl	1.42	8.92	3	0.25
St+St+St	7.82	7.82	3	0

Table 2.1: The different types of particles used in out experiments along with their corresponding κ and χ values. Materials used are: steel (St), aluminum (Al), copper (Cu), Delrin plastic (Pl), tungsten carbide (Tc), and zirconium dioxide (ZrO_2). Values of χ are kept to two significant digits.

After the particles were released, we imaged their sedimentation using a CCD camera (Point Grey) at 6 frames per second with a spatial resolution of 12 pixels per mm. After recording, we processed the images using ImageJ [103] for easier detection of each sphere in a composite particle. Images were first binarized with a brightness threshold, then each sphere was separated with a watershedding algorithm. The resulting image was eroded, leaving us with easily-trackable objects composed of white pixels. Particle tracking and linking between frames were done with TrackPy [104]. The resulting trajectories of the individual spheres were used to calculate various quantities associated with the dynamics of the composite particles.

The second set of experiments were done in a cylindrical 3D chamber of diameter of 12 cm and a height of 21 cm (see Sec. 2.4). The chamber was fabricated from a cast acrylic tube with wall thickness 12 mm. The chamber was also filled with silicone oil of the same viscosity (10,000 cSt). We placed 100 particles of a single κ and χ combination in the fluid and sealed the chamber so that there were no trapped

air bubbles. Particles were allowed to sediment under gravity to the bottom of the chamber, and the distribution of particles was imaged from above. We then flipped the chamber and repeated the experiment 50 times for each set of particles. Due to finite-size wall effects driving convection and particles resting on top of one another, identifying the individual spheres from each particle was not feasible, as done in the 2D experiments. Thus, images were cropped and binarized and the spatial distributions of black pixels were analyzed.

The quasi-2D geometry allows us to easily track the position and rotation of particles, but it also imposes a form of screening for the interactions between particles. The divergence of velocity fluctuations in suspensions arises from the $1/r$ decay of velocity around a sedimenting particle, however, in confined 2D environments the fluid flow decays as $1/r^2$. A detailed discussion of the differences can be found in Beatus et al. [105]. The faster decay allows convergence of the velocity fluctuations found in 3D, meaning that the majority of the screening is provided by the confining walls of our chamber. Although this is important for a statistically large number of particles, our results show that mass polarity strongly affects sedimentation dynamics in both 2D and 3D geometries.

2.3 Results and Discussion

2.3.1 Single Particle Dynamics

After fabricating the composite, prolate particles, we observed the sedimentation of single, isolated particles to better understand their dynamics and to extract the terms in the mobility matrix (Eq. 2.6). The response of a single particle to an external force or torque informs its effective interactions with neighboring particles [41, 42]. For example, a rod-shaped particle of uniform mass density will sediment without a change in its initial angle [33, 42]. This results in a diagonal drift. However, the mass polar-

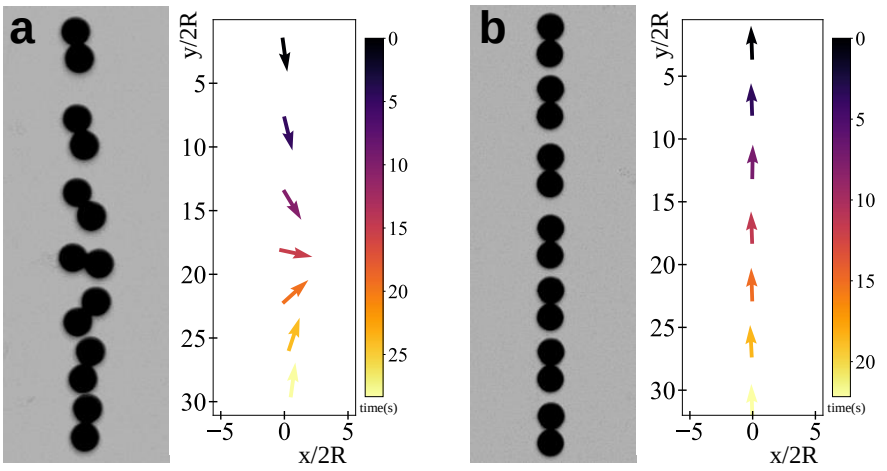

Figure 2.2: Two representative examples of the particle trajectories in our single particle experiments. $x = 0$ is defined as the geometric center of the particle at the earliest time. Panel (a) shows a particle with $\chi > 0$ (Cu+St, see Table 2.1). The left part of the panel is a composite image of the particle during the length of the experiment. The right graph shows the corresponding particle orientations, with the arrows pointing from the heavier sphere (Cu) to the lighter sphere (St). The color bar represents time. Gravity points downward in all pictures. Panel (b) shows a particle with $\chi = 0$ (St+St).

ity of our objects causes them to align with the external gravitational field, meaning that a mass polar object will rotate until its center of geometry lies directly above its center of mass ($\theta = 0$). For our experiments, mass polar particles were released from an initial angle of $\theta = \pi$, so that they rotated a total of π radians throughout the sedimentation process. A trajectory for a single $\kappa = 2$ particle composed of Cu+St (see Table 2.1) is shown in Fig. 2.2a. Particles with larger values of χ rotated much more rapidly due to the larger gravitational torque applied to the geometric center of the particle. This can be compared with a St-St particle in Fig. 2.2b, which shows no preference for rotations since it has no mass polarity ($\chi = 0$). For particles with $\chi = 0$, we occasionally observed "fluttering", or oscillations of angular orientation during sedimentation. This was likely due to interactions with the walls of the experimental chamber during slight rotations out of the quasi-2D plane of the experiment [106, 107].

To quantitatively capture the coupling between the external force and dynamics of single particles, we applied the mobility matrix formalism (Eq. 2.6). Because we are using a quasi-2D geometry, the complexity of the problem is reduced since the particle can only rotate in the plane. However, the mobility coefficients will be different from those measured in an unbounded, 3D fluid. With two planar walls, our experimental setup is most similar to a Hele-Shaw cell, where the mobility matrix formalism has already been successfully implemented [108] and tested [109]. Because we are considering symmetric prolate particles, the mobility matrix in the body frame (indicated by superscript b) is reduced to:

$$\begin{pmatrix} v_x^b \\ v_y^b \\ \omega_z^b \end{pmatrix} = \frac{1}{6\pi\eta R} \begin{pmatrix} a_t & 0 & 0 \\ 0 & b_t & 0 \\ 0 & 0 & \dfrac{3a_r}{4R^2} \end{pmatrix} \begin{pmatrix} F_x^b \\ F_y^b \\ \tau_z^b \end{pmatrix}, \tag{2.9}$$

where v_x^b and v_y^b are the translational velocities in the body frame and ω_z^b is the angular velocity perpendicular to the plane of motion. F_x^b and F_y^b are the components of the gravitational force in the body frame, and τ_z^b is the external torque from gravity about the particle's center of geometry (see Fig. 2.1). The dimensionless translational mobility coefficients b_t and a_t represent mobility along the major and minor axes of the particle ($b_t > a_t$). The dimensionless rotational mobility coefficient is a_r. These coefficients should be identical for all of our particles with the same κ and R, regardless of the internal density distribution (χ). They characterize the drag from the external flow, which applies stress on the surface of the particle.

Our experimental data, however, are collected in the lab frame. Thus, we first rotate all vectors and the mobility matrix by an angle θ (Fig. 2.1) to obtain the

equations of motion in the lab frame:

$$\mathbf{\Omega} = \begin{pmatrix} \cos(\theta) & \sin(\theta) & 0 \\ -\sin(\theta) & \cos(\theta) & 0 \\ 0 & 0 & 1 \end{pmatrix} \tag{2.10}$$

$$\mathbf{\Omega} \cdot \begin{pmatrix} v_x^b \\ v_y^b \\ \omega_z^b \end{pmatrix} = \left(\mathbf{\Omega} \cdot \frac{1}{6\pi\eta R} \begin{pmatrix} a_t & 0 & 0 \\ 0 & b_t & 0 \\ 0 & 0 & \dfrac{3a_r}{4R^2} \end{pmatrix} \cdot \mathbf{\Omega}^{-1} \right) \mathbf{\Omega} \cdot \begin{pmatrix} F_x^b \\ F_y^b \\ \tau_z^b \end{pmatrix} \tag{2.11}$$

After multiplying and collecting terms, we use the substitutions $2c_1 = a_t + b_t$, $2c_2 = b_t - a_t$, and $c_3 = 3a_r/4$ to write the result in the following form:

$$\begin{pmatrix} v_x \\ v_y \\ \omega_z \end{pmatrix} = \frac{1}{6\pi\eta R} \begin{pmatrix} c_1 - c_2\cos(2\theta) & c_2\sin(2\theta) & 0 \\ c_2\sin(2\theta) & c_1 + c_2\cos(2\theta) & 0 \\ 0 & 0 & \dfrac{c_3}{R^2} \end{pmatrix} \begin{pmatrix} 0 \\ F_y \\ \tau_z \end{pmatrix}. \tag{2.12}$$

We have chosen this parameterization out of convenience. For example, in the case of a perfect sphere, $b_t = a_t$, thus $c_1 = 1$, $c_2 = 0$, and $c_3 = 3/4$ (Eq. 2.7). We have dropped the superscript since we are referring to the lab frame where the gravitational force only points in the y-direction. The matrix multiplication above gives us the following equations of motion for our particles in the lab frame:

$$v_x = \dot{x} = \frac{c_2\sin(2\theta)}{6\pi\eta R} F_y, \tag{2.13}$$

$$v_y = \dot{y} = \frac{c_1 + c_2\cos(2\theta)}{6\pi\eta R} F_y, \tag{2.14}$$

$$\omega_z = \dot{\theta} = \frac{c_3}{6\pi\eta R^3} \tau_z. \tag{2.15}$$

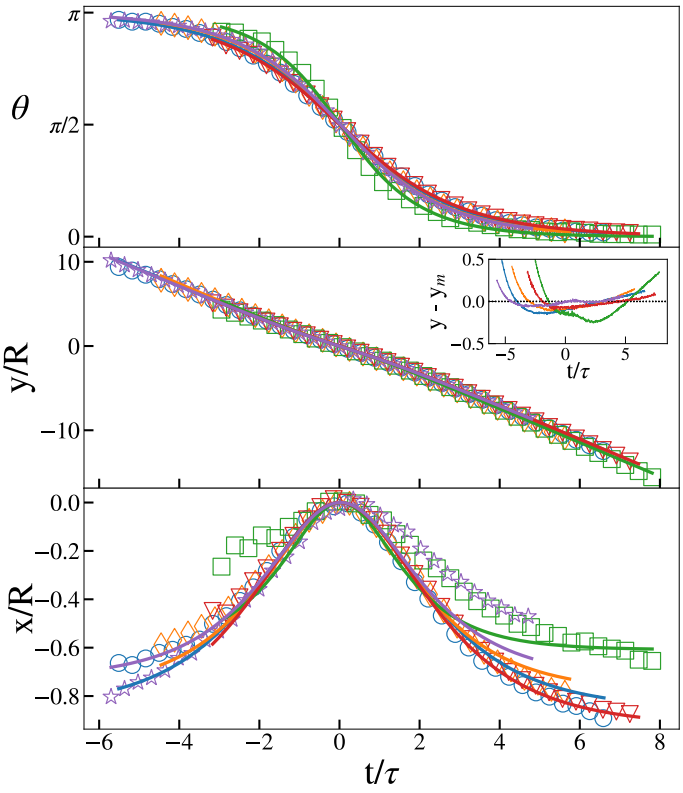

Figure 2.3: Data for 5 experiments with a single Al+Pl particle (Table 2.1). Only 5% of points are plotted for clarity. Initially, the heavy aluminum sphere begins above the lighter Delrin sphere. Open symbols represent data, and curves are model fits from Eqs. 2.23, 2.25, and 2.24. Different symbols and colors are separate experiments. Inset: residual difference between the model fit y_m and the data y for the vertical position of the particle.

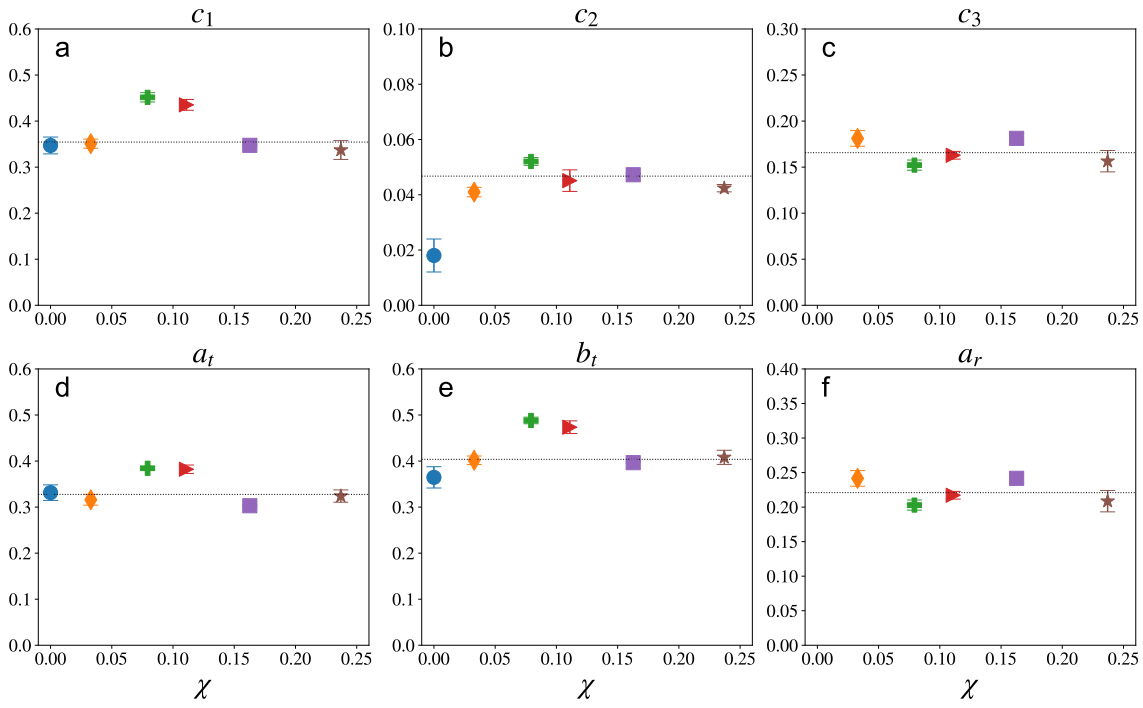

Figure 2.4: Best-fit parameters vs. χ from Eqs. 2.23-2.25 for single particle sedimentation experiments with $\kappa = 2$. The material combinations used were: circle, St+St; diamond, Cu+St; plus, St+ZrO_2; right triangle, Cu+ZrO_2; square, Al+Pl; star, Al+St (see Table 2.1). Each data point is the weighted mean of five different trials with error bars representing the standard error of the mean. Panels (a-c) show the parameters c_1-c_3 directly computed from the nonlinear regression of data in the lab frame. Panels (d-f) show the body frame coefficients: a_t, b_t, and a_r. St+St is missing from c_3 and a_r because of the limiting form of $\theta(t)$ when $\chi = 0$ (Eq. 2.26), which has no dependence on c_3.

The dotted variables denote differentiation with respect to time. Similar simplified equations for single particle dynamics in quasi-2D geometries have been derived by Bet et al. [108] and Ekiel-Jeżewska and Wajnryb [110]. In our experiments, the net force and torque on a particle will depend on the values of κ and χ. For $\kappa = 2$ particles, the net gravitational force, and torque about the center of geometry are:

$$F_y = -\frac{4}{3}\pi R^3(\rho_h + \rho_l - 2\rho_f)g \tag{2.16}$$

$$\tau_z = -\frac{4}{3}\pi R^4(\rho_h - \rho_l)g\sin\theta. \tag{2.17}$$

Equations 2.13-2.15 are coupled through θ, and can be solved analytically. However, the solution can be generalized by making the equations dimensionless. We used the sphere radius R for a characteristic length scale, and $\tau = R/U_T$ for the characteristic time scale, where U_T is the terminal velocity of the lighter sphere (Eq. 2.1). This nondimensionalization results in the following equations of motion, where all variables are considered dimensionless for clarity of notation:

$$\dot{x} = -K_1 c_2 \sin(2\theta) \tag{2.18}$$

$$\dot{y} = -K_1(c_1 + c_2\cos(2\theta)) \tag{2.19}$$

$$\dot{\theta} = -K_2 c_3 \sin(\theta) \tag{2.20}$$

$$K_1 = \frac{\rho_h + \rho_l - 2\rho_f}{\rho_l - \rho_f} \tag{2.21}$$

$$K_2 = \frac{\rho_h - \rho_l}{\rho_l - \rho_f} \tag{2.22}$$

Equation 2.20 can be immediately solved since it is independent of the other equations. The result is:

$$\cot\left(\frac{\theta(t)}{2}\right) = \cot\left(\frac{\theta_0}{2}\right)e^{K_2 c_3 t}, \tag{2.23}$$

where θ_0 is the initial value of θ at $t = 0$. Plugging this back into Eqs. 2.18 and 2.19 and simplifying algebraically, we get:

$$x(t) = x_0 + \frac{4c_2FK_1\cot(\theta_0/2)}{c_3K_2 - c_3F^2K_2\cot(\theta_0/2)^2} - \frac{2c_2K_1\sin(\theta_0)}{c_3K_2}, \tag{2.24}$$

$$y(t) = y_0 - \frac{K_1}{K_2c_3}\left((c_1+c_2)c_3K_2t + 2c_2\left(\cos(\theta_0) + \frac{1 - F^2\cot^2\left(\frac{\theta_0}{2}\right)}{1 + F^2\cot^2\left(\frac{\theta_0}{2}\right)}\right)\right), \tag{2.25}$$

where $F = e^{K_2c_3t}$ is a function of time, and used here for compactness. In the limit of particles with uniform mass density ($K_2 \to 0$, $\chi \to 0$), these functional forms simplify to:

$$\theta(t) = \theta_0, \tag{2.26}$$

$$x(t) = x_0 - c_2K_1t\sin(2\theta_0), \tag{2.27}$$

$$y(t) = y_0 - K_1t(c_1 + c_2\cos(2\theta_0)). \tag{2.28}$$

Equations 2.26-2.27 verify the prediction that for polar particles of uniform density, the angle of inclination doesn't change, and the particle drifts laterally in the x-direction [33].

After taking the inverse cotangent of Eq. 2.23 and using standard least-squares nonlinear regression, we can fit these analytic forms to the experimental data with very good agreement. Figure 2.3 shows 5 identical experiments and their corresponding fits. For $\theta(t)$, there are only 2 fitting parameters, c_3 and θ_0. Once they are determined by the fit, then $x(t)$ can be fit for the parameters c_2 and x_0. Finally, $y(t)$

can then be fit for c_1 and y_0. The curves are compared to each other by assigning $t = 0$ when the particles are completely horizontal, i.e. $\theta = \pi/2$. We also moved the x and y origin to correspond to $t = 0$. Open symbols represent data, and curves are the fits to Eqs. 2.23, 2.25, and 2.24. The fits for the x-position show more systematic deviation from the data, yet the overall displacement is also much smaller. For example, as shown in the inset in y vs. t, the residuals of these fits are comparable to the variability in x vs. t, which is a fraction of a particle radius in displacement. Although the source of the systematic asymmetry is unclear, we suspect that when particles are released from the gating mechanism, they are not perfectly parallel with the walls of the quasi-2D chamber. If a particle's alignment varies during the rotation from $\theta = \pi$ to $\theta = 0$, we would expect variations in the mobility coefficients (i.e., c_2) due to wall effects [35, 106], resulting in an asymmetry in $x(t)$ about $\theta = \pi/2$. Additionally, we do not expect errors in particle tracking to lead to systematic asymmetry even though the x-motion is on the order of the particle size. Tracking errors would manifest more as random noise rather than systematic deviations from theory. The data for θ, x, and y can also be fit simultaneously using a global least squares regression for all parameters, since parameters appear in multiple equations. We found less than 5% difference in the fitted parameter values using this method, so we have only chosen to report the results of the sequential fitting. Similar analytic solutions and quality of fits were recently found in the alignment of mirror-symmetric particles in a microfluidic device [108, 109].

One of the major assumptions of our model was that all coefficients are independent of χ, and only depend on the shape of the composite, prolate particles. This is evident from Eq. 2.9, since a_t, b_t, and a_r are dimensionless coefficients that only depend on the particle shape, not the density distribution. We confirmed this prediction using all fits of single particle experiments with $\kappa = 2$, as shown in Fig. 2.4a-c. The coefficients c_1, c_2, and c_3 are computed directly from nonlinear least-squares re-

gression of the data (Eqs. 2.18-2.20). For particles with $\chi = 0$ (uniform density), we used Eqs. 2.26-2.27 to fit the data. In this form, there is no torque from gravity, so c_3 cannot be determined and is not shown. However, c_1 and c_2 can be determined, but are not very reliable because of experimental artifacts that affect the angle (and thus translational velocity) during sedimentation. These artifacts include small differences in the distribution of glue used between the particles, rotations out of the quasi-2D plane, and other 2D confinement effects such as "fluttering" [35, 106, 107]. For finite χ, the particles rotate significantly due to gravitational torque, and c_1, c_2, and c_3 can be determined reliably. There appears to be some small systematic trend in c_1, but the overall variation is small and the data for all parameters is consistent with a constant value over the range $0 < \chi < 0.25$.

Using $2c_1 = a_t + b_t$, $2c_2 = b_t - a_t$, and $c_3 = 3a_r/4$, we computed the shape-dependent drag coefficients of our symmetric particles in the body frame, as shown in Fig. 2.4d-e. Here again, a_r cannot be determined from $\chi = 0$ data, and data with finite χ are most reliable. The average values of these mobility coefficients with $\chi > 0$ are shown by the dashed lines: $\bar{a}_t = 0.328 \pm 0.018$, $\bar{b}_t = 0.404 \pm 0.012$, and $\bar{a}_r = 0.221 \pm 0.008$. We suggest that these experimental values for the mobility coefficients can be compared directly to simulations of particles composed of spheres [111]. In comparison to sedimentation in an unbounded, 3D fluid, we expect our measured values of a_t, b_t, and a_r to be somewhat smaller since the particles experience a larger drag due to the confining walls.

2.3.2 Sedimenting Particle Pairs

Goldfriend et al. [41] theoretically examined a sedimenting suspension of mass polar spheroids using a continuum linear stability analysis. To briefly summarize their results, they considered a suspension of particles settling due to an external body force F in the direction of gravity in a fluid of viscosity η. A sinusoidal concentration per-

turbation was applied in a direction perpendicular to the force with amplitude $c(x)$ and a characteristic wavelength λ. These fluctuations in the concentration create velocity fluctuations, $U(x)$. Balancing the change in gravitational force of the suspension versus the change in the drag force gives: $c\lambda F \approx U\eta/\lambda$. By solving for the amplitude U, we see that $U \sim c\lambda^2 F/\eta$. The indefinite scaling of U with λ is a demonstration of the Caflisch-Luke paradox described in the introduction. These slabs of particles will also experience vorticity of the magnitude $U/\lambda \sim c\lambda F/\eta$. For uniform spheres, this will cause a rotation of the sphere, but no drift. However, self-aligning objects will be tilted away from their preferred alignment. This causes a drift in the x-direction with velocity $\sim \gamma RcF/\eta$, where $\gamma = \gamma(\kappa, \chi)$ is a proportionality constant determined by the shape and mass distribution of an individual particle. For positive γ, which requires $\kappa > 1$ [41], the relative velocity of the particles is positive, meaning they drift away from each other. This is the screening mechanism that stabilizes the suspension. For negative γ, which requires $\kappa < 1$, they drift towards each other, leading to unbounded growth of the instability.

In our experiments, we examined the particle-level interactions by measuring the relative separation of pairs of prolate ($\kappa > 1$) particles as they repel each other during sedimentation. We placed two particles heavy-side down in adjacent slots of the plastic gate so that their initial separation was 3.3 mm. Each experiment was conducted five times for reproducibility. Figure 2.5 shows a representative selection of settling trajectories for various values of κ and χ. These are composite images of the particles during sedimentation, spaced 3.33 s apart. The arrows to the right of each panel show the orientations of each particle during sedimentation, and the color represents time. First, particles with $\chi = 0$ heavily influenced each other. Their dynamics were typically characterized by one of the particles rotating or flipping completely. This particle often lagged behind the other one, which did not flip, but followed a curved trajectory. This can be seen in both Fig. 2.5a and Fig. 2.5d.

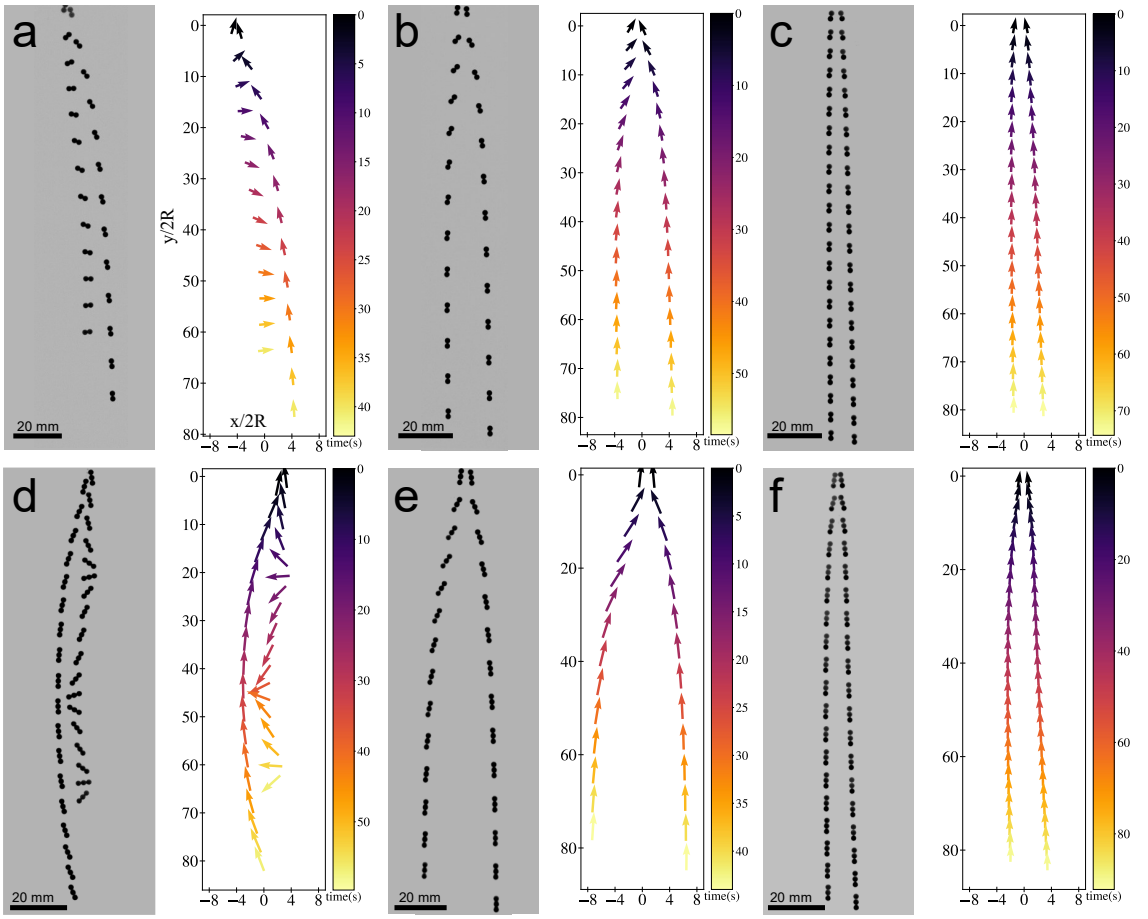

Figure 2.5: Experimental trajectories of two-particle interaction experiments. In each alphabetic panel, the image shows a composite of the particles' trajectories during sedimentation. The graph shows the orientation of the particles with arrows pointing from the heavier particle to the lighter particle(s). The color is used to show when two arrows are at the same time during their transit. $x = 0$ is defined as the halfway point between the particle centers on the first frame. Panels (a), (b), and (c) are $\kappa = 2$ particles, panels (d), (e), and (f) are $\kappa = 3$ particles. Panels (a) and (d) show particles with $\chi = 0$. Panels (b) and (e) show particles with the smallest χ, Cu+St (see Table 2.1). Panels (c) and (f) show particles with the largest χ, Cu+Pl (see Table 2.1).

The particles did not preferentially align to gravity, and instead produced a variety of dynamics. For example, the periodic variation in separation visible in 2.5d is reminiscent of Kepler orbits observed in sedimenting pairs of disks [43]. In fact, a periodic variation in the relative position between adjacent, sedimenting prolate particles was theoretically predicted by [82] (Fig. 4). On average, we did not observe a net repulsion or attraction between our particles with a uniform mass distribution ($\chi = 0$).

For particles with $\chi > 0$, there was an immediate rotation and repulsion between the particles leading to a horizontal separation that grew with time. Eventually the particles would align with the external gravitational field, and the separation saturated. This is shown in Figs. 2.5b-c for $\kappa = 2$ and Figs. 2.5e-f for $\kappa = 3$. The finite width of the quasi-2D chamber, $4R$, introduced a length scale that could potentially set an upper limit on the range of the repulsive interaction. However, we observed that the final separation between the particles could be as much as $30R$ (Fig. 2.5e) for smaller values of χ. The repulsive effect was most prominent for particles composed of materials with closely-matched densities (i.e. copper and steel). Although this may seem counter-intuitive at first, particles with $0 < \chi \ll 1$ can rotate away from vertical more easily, and thus experience a larger repulsion and horizontal drift. As $\chi \to 0$, we expect one of the particles to be able to flip entirely if they are close enough to interact strongly, leading to the periodic type of interactions observed for $\chi = 0$ (Figs. 2.5a and 2.5d). In this limit, the eventual behavior of the sedimenting particles should be determined both by χ and by the initial separation.

The inverse relationship between χ and the mutual repulsion was also predicted by Goldfriend et al. [41]. The authors found that the growth rate of the horizontal velocity fluctuations scaled as $\gamma = \kappa^{2/3}/3\chi$ for highly prolate particles ($\kappa \gg 1$). To quantify this effect in our experiments, we chose to measure the total change in horizontal separation, ΔH, between the particles' geometric centers in each experiment.

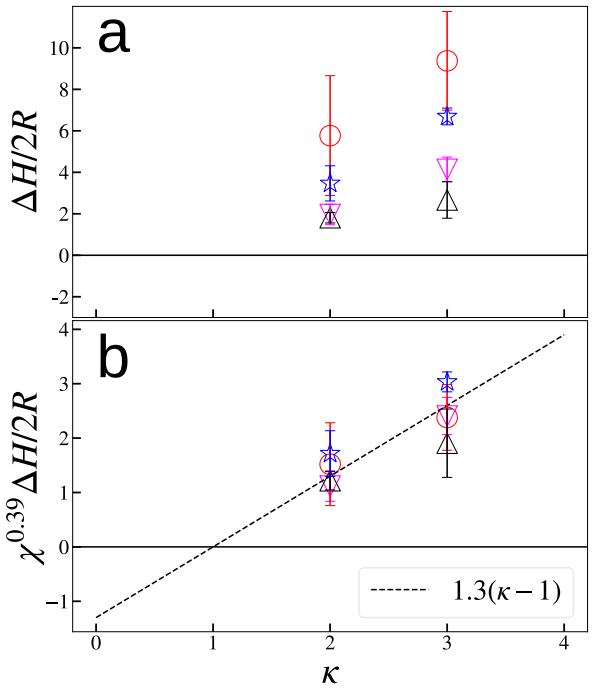

Figure 2.6: Graphs of our experimental response parameter, ΔH, versus κ. ΔH is defined as the difference between the final and initial horizontal separation. The colors and shapes represent different material combinations of the composite particles. By order of increasing χ, they are Cu+Pl (upright triangle), Al+St (upside down triangle), Tc+St (star), and Cu+St (circle) (see Table 2.1). Panel (a) is the raw data, with each data point being an average over five runs and error bars representing one standard deviation. Panel (b) is the same data collapsed using the best fit parameters obtained from Eq. 2.29.

This is plotted in Fig. 2.6a as a function of κ. Generally, the separation increased with κ. However, in order to compare between each set of experiments that corresponded to different values of χ, we multiplied the final separation by χ^{α}, where α was determined by simultaneous fitting of all the data to the following form:

$$\chi^{\alpha}\frac{\Delta H}{2R} = A(\kappa - 1), \tag{2.29}$$

where we have imposed the requirement that there be no repulsion for $\kappa = 1$ (i.e. single spheres). The fit was performed by subtracting the left and right hand sides of Eq. 2.29, squaring the difference, and summing over all data points. The best fit values for the parameters were $\alpha = 0.39 \pm 0.05$ and $A = 1.28 \pm 0.20$, where the errors represent one standard error. The fit shows very good agreement with the data, as plotted in Fig. 2.6b.

In general, the predictions from Goldfriend et al. [41] are in excellent qualitative agreement with our experiments, yet the scaling, $\alpha \sim 0.39$, is quite different than that predicted by Goldfriend et al. [41]: $\alpha \sim 1$. There are a few reasons that can explain this discrepancy: 1) γ represents an instantaneous response for an initially-uniform concentration of particles. Here we are using the final separation, ΔH, which is essentially an integral of the repulsion between the particles in time. 2) The quasi-2D environment should screen the long-ranged, $1/r$ hydrodynamic interactions [105], so one may expect a different theoretical scaling between γ and χ based purely on geometry. 3) Our quasi-2D chamber may introduce other effects that depend on the thickness of the chamber, for example, it is well known that the net viscous drag force on a sedimenting particle can be dependent on distance to a nearby wall [35, 106]. 4) Our particles are not perfect examples of the prolate and oblate ellipsoids discussed in Goldfriend et al. [41]. Despite these differences, the experimental data with different values of κ and χ can be reasonably collapsed using the dependence listed in Eq. 2.29.

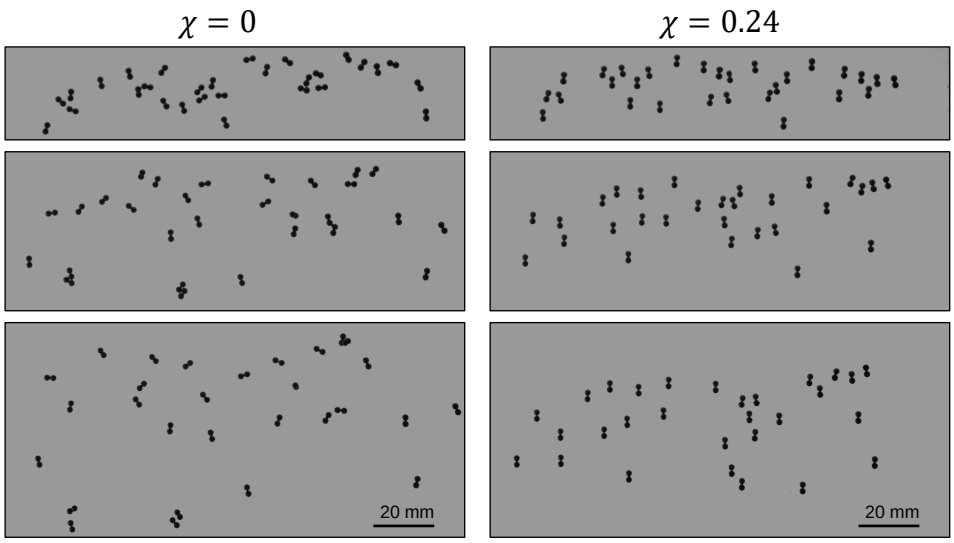

Figure 2.7: Series of 3 sequential images of 29 particles sedimenting in our quasi-2D chamber. The left column ($\chi = 0$) shows St+St particles, and the right column ($\chi = 0.24$) shows St+Al particles (Table 2.1). The top row shows images at the same vertical position near the top of the experimental chamber at early times, the middle row shows the same particles later in time, and the bottom row shows the particles near the end of the experiment, at the bottom of the chamber.

Lastly, we verified that this mutual repulsion led to more uniformly distributed suspensions of many particles. We filled our quasi-2D chamber with 29 particles with $\kappa = 2$. The left column Fig. 2.7 shows that for particles with $\chi = 0$, there is no preferential alignment to gravity, resulting in a large spread of particle separations, both vertically and horizontally. Particle can flip very easily, and often came into contact. Some of the particles experienced small rotations out of the plane as well. The right column of Fig. 2.7 illustrates that particles with $\chi = 0.24$ followed a more uniform spatial distribution. All particles tended to align with gravity, resulting in a mutual repulsion. When particles are in close proximity, they tilted away from the vertical and drifted apart, similar to Fig. 2.5. Surprisingly, the particles with $\chi = 0.24$ did not spread as much in the vertical direction as $\chi = 0$, suggesting that vertical fluctuations in concentration may be suppressed for $\chi > 0$. An intuitive explanation for this behavior stems from the variations in vertical velocities of particles. For

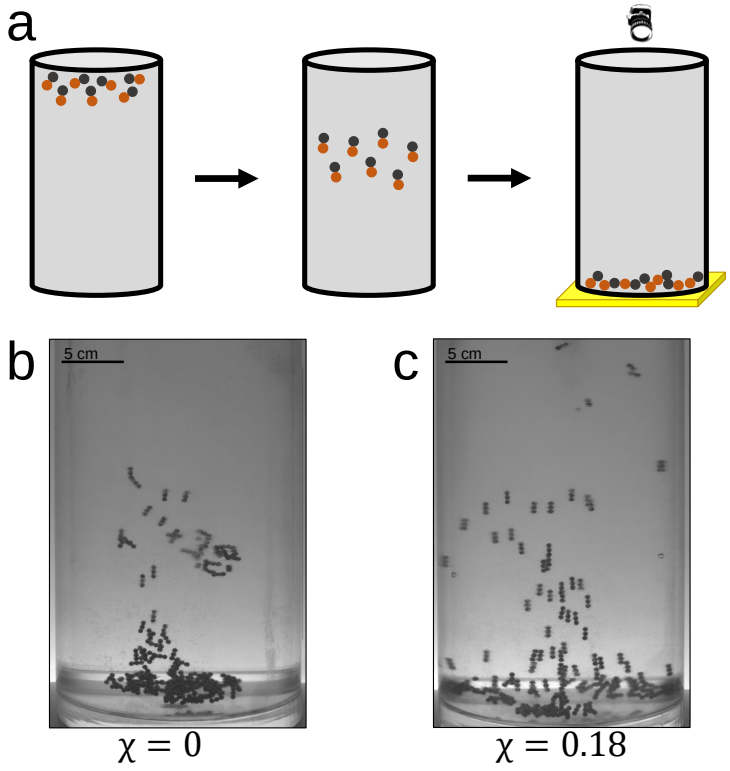

Figure 2.8: (a) Experimental procedure for 3D sedimentation. The sealed chamber was repeatedly flipped and imaged, as described in Sec. 2.2. (b) Sample image from the side during a single sedimentation experiment of particles with $\chi = 0$ and $\kappa = 3$ (St+St+St). (c) Sample image during sedimentation of particles with $\chi = 0.18$ and $\kappa = 3$ (St+Al+Al).

$\chi = 0$, particle rotations lead to a spread in vertical terminal velocities (Eq. 2.25), whereas particles with $\chi > 0$ are mostly aligned to gravity and sediment at the same rate. Although vertical fluctuations were not directly addressed in Goldfriend et al. [41], we hypothesize that the mutual repulsion in mass polar particles also suppresses the "clumping instability" observed in uniform suspensions [44] that leads to large vertical separations between particles.

2.4 3D Particle Suspensions

Although the effective repulsion between our prolate particles is apparent in a confined, quasi-2D environment, it is possible that the dynamical evolution of these par-

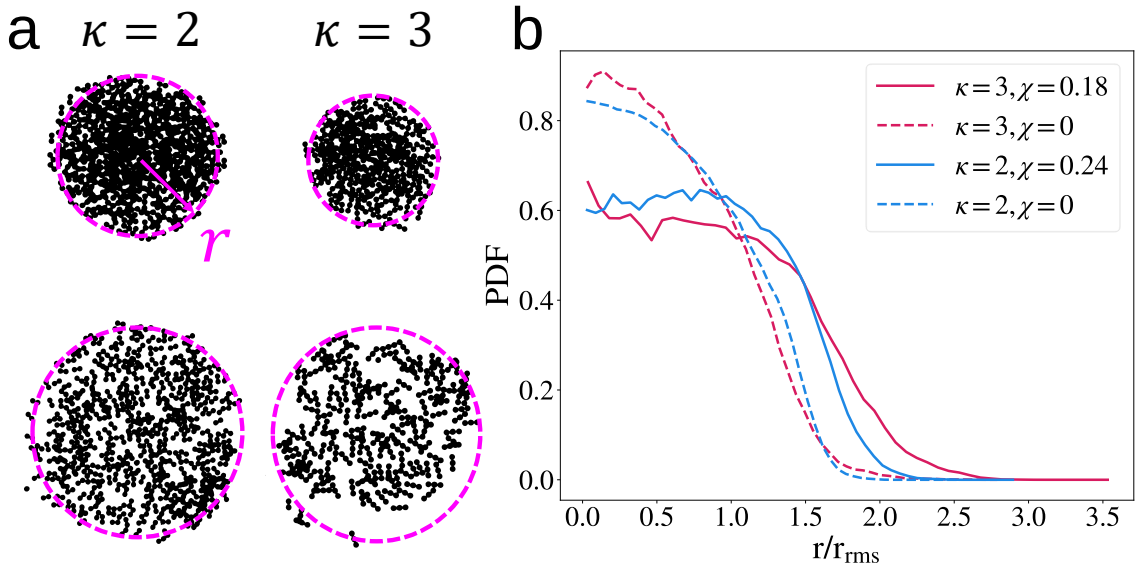

Figure 2.9: (a) Sample images of particles resting on the bottom of the 3D chamber after sedimentation. The left column shows $\kappa = 2$ particles with $\chi = 0$ (St+St; top) and $\chi = 0.24$ (St+Al, bottom). The right column shows $\kappa = 3$ particles with $\chi = 0$ (St+St+St; top) and $\chi = 0.18$ (St+Al+Al, bottom). We quantified the radial distribution of black pixels at a different radii r from the center of the sedimented pattern, as indicated by the magenta arrow. (b) Radial probability density function (PDF) of black pixels from the images. The radius has been normalized by r_{rms} for $\chi = 0$ (Eq. 2.30). The legend indicates the values of κ and χ for the different PDFs. Each curve was produced using data from 50 post-sedimented images.

ticles in 3D could hinder the repulsion since the particles have more motional degrees of freedom. Figure 2.8 illustrates the experimental procedure, described in Sec. 2.2, where particles are sedimented repeatedly and their resulting spatial distribution is imaged after each repeated experiment. For $\chi = 0$, particles tended to cluster during sedimentation, resulting in a rapid increase in their velocity due to mutual drag reduction at finite distances. For $\chi = 0.18$, there is a visible alignment of particle to the direction of gravity (vertical), and a broader spatial distribution with less clustering.

To quantify the post-sedimentation spatial distribution of particles, one would ideally extract the center of mass position of each particle and calculate the radial distribution function of their positions. However, after sedimentation we found that particles often overlapped by stacking in the vertical direction, making identifying the center of mass impossible. Instead, we choose to threshold the images so that particles became black pixels, and the background became white. Samples of these images are shown in Fig. 2.9. We then calculated the radial distribution function of the positions of the black pixels. This was done by first finding the center of mass of all black pixels, corresponding to $r = 0$ in each image, and then binning pixel positions radially along r. We divided the number of pixels in each bin range by the area of the annulus associated with the bin. In order to compare between $\kappa = 2$ and $\kappa = 3$, we also normalized the radial positions by the root mean squared radius of the data for $\chi = 0$, calculated by:

$$r_{rms} = \sqrt{\frac{1}{N}\sum_{r} r^2}. \tag{2.30}$$

Here, the sum runs over every black pixel in all 50 images associated with $\chi = 0$, and N is the sum total of all black pixels from all images with $\chi = 0$.

The resulting distribution functions are shown in Fig. 2.9. After normalizing the radial position, we see that all data for $\chi = 0$ collapses onto the same distribution

(dashed lines). As expected, when $\chi > 0$ (solid lines), these distributions broaden due to the net repulsion between the particles. Furthermore, particles with larger κ and smaller non-zero χ should experience a larger respulsion, as predicted by Eq. 2.29. This is consistent with our data, since the distribution for $\kappa = 3$, $\chi = 0.18$ is broader than for $\kappa = 2$, $\chi = 0.24$. We note that because the initial state of each round of sedimentation was set by the final state of the previous one, the sequential images of the final sedimentation pattern were not statistically independent. Nevertheless, we don't expect these effects to qualitatively change our results, and taken together, Fig. 2.8 and Fig. 2.9 confirm that the effective pairwise repulsion between mass polar particles also suppresses clumping in 3D.

2.5 Conclusion

Particles with mass polarity are forced to align with the direction of gravity during sedimentation. This alignment arises because the center of mass is displaced from the geometric center of each particle, resulting in a net torque imposed by the fluid flow. Our work examined the motion of single particles sedimenting in a viscous fluid, and we derived a simple analytic expression for the their motion in a quasi-2D environment. Fitting trajectories of the individual particles allowed us to reconstruct the parameters of the mobility matrix. When two or more prolate particles are present, we showed that they experience a mutual repulsion, as first described by Goldfriend et al. [41]. Surprisingly, this repulsion is strongest for small values of χ, i.e. when the center of mass is only slightly displaced from the center of geometry. The repulsion also increases as the particles become more asymmetric (more prolate, large κ). We also showed that this overall repulsion persists in 3D experiments with hundreds of particles.

There are still many open questions facilitated by this work. First, Goldfriend

et al. [41] showed that there should be a mutual attraction between particles for $\kappa < 1$. We found that our particle fabrication method, i.e. gluing individual spheres together, did not easily lend itself to making oblate particles with $\kappa < 1$. Such particles would cluster rapidly during sedimentation, and may dramatically increase the overall sedimentation rate of a suspension of particles. Additionally, Goldfriend et al. [41] predicted the existence of hyperuniformity in the density distribution of a sedimenting suspension. Our experimental results in 3D demonstrate a net repulsion and a more uniform concentration, yet we would need many more particles with accurate tracking in 3D to quantify hyperuniformity. One alternative route could be simulating many particles efficiently with a parameterized interaction based on our results. We hope our simplified mobility matrix may serve as a starting point for such idealized simulations of many interacting particles.

2.5.1 Future Outlook

This discussion has been focused on geometrically symmetric particles, albeit with rotational asymmetry provided by a center of mass offset. However, natural particles rarely ever exist as such idealized shapes [49, 71–73]. One avenue of investigation left open is the question of what happens when we relax the assumption of mirror symmetry. Particles without mirror symmetry are called chiral, and they are characterized by the fact that there does not exist a plane that, once mirrored across, a particle and its mirror cannot be mapped onto one another through simple rotations and translations. The prototypical example of a chiral object is the helix. Sedimentation of chiral objects has been studied extensively using theoretical measures [42, 45, 46, 101, 112, 113]. As we saw with mass polar objects, simple adjustments to the geometry of particles will cause them to translate or rotate when driven by an external force. Tuning specific parameters of the particles (e.g. density or size) can change the degree and form of response intrinsically. This allows control of particle

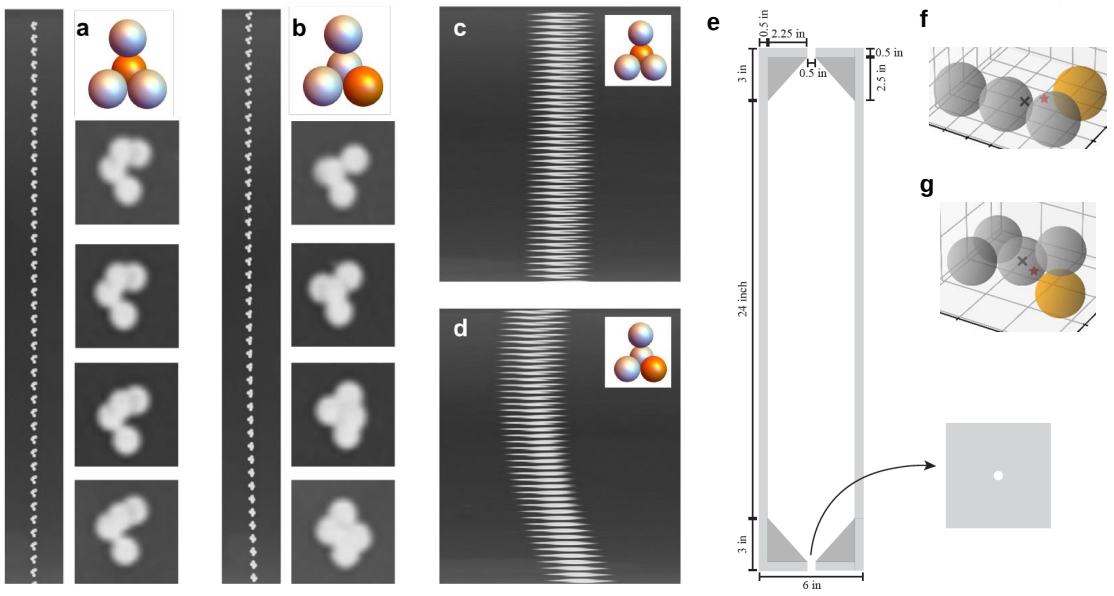

Figure 2.10: Showcase of chiral sedimentation experiments and new sedimentation tank. (a) and (c) A mass polar, non-chiral object with an unedited trajectory (a) and stretched trajectory (c). (b) and (d) A mass polar, chiral particle with an unedited trajectory (b) and stretched trajectory (d). Grey particles are aluminum, and orange particles are copper. All spheres are 2 mm in diameter. The stretched trajectory elucidates the drifting, spiral like motion predicted for chiral objects. (e) Schematic of new sedimentation tank, the base of the tank is a square. (f) and (g) Other chiral particle shapes that will be explored in future sedimentation experiments. The red star indicates the center-of-mass of the composite particle, the black X represents the geometric center of the object.

transport without the need for any external fields or driving. We physically realize chiral particles through a center-of-mass offset outside of the particle's symmetry plane, which has been predicted to produce a chiral response in sedimenting suspensions [42]. An example can be seen in Fig. 2.10a and 2.10b, where both particles are mass polar, but only the particle in 2.10b demonstrates a chiral response. To study chiral sedimentation, we have been developing new chiral particles and a new sedimentation chamber that provides several upgrades to our current experiments. A diagram of a few of our new particles can be seen in Fig. 2.10a, b, f, and g. We glue 2 mm spheres of different materials together, and we place the heavy sphere outside of the symmetry plane of the object, causing it to become chiral [42]. At least four particles are needed to create a chiral particle, because no matter how you glue three spheres together, they will always share a symmetry plane. Even for mass polar particles, three spheres cannot be glued together in such a way as to produce a chiral particle. For our chamber, we want to reduce the effects of the walls on our particles, since it is known that sedimenting particles close to boundaries experience a modified drag force that is dependent on the distance to the wall [35, 106, 114]. We also need a taller viewing area in an aim to capture multiple periods of particle rotations. The chamber is now a 15.24 cm x 15.24 cm x 76.2 cm rectangular box, seen in Fig. 2.10e, with a single input and output hole for particles to travel through. These holes allow us to retrieve particles easily after experiments, as we found pulling particles back out of our 2-D chamber was difficult and wasted a lot of silicone oil in the process. These holes can be sealed on the outside so that the tank may be flipped multiple times to allow repeated trials to be done on the same particle. Variations in the fabrication of particles won't be as impactful using this method since the same particle can be used for a set of experiments. The chamber will also be allowed to rotate about one of its short axes, with each flip being the start of a new sedimentation experimental run. As the particle sediments, we will image it with a single camera at a fixed

distance. However, the extraction of the 3-D orientation is necessary to quantify the particle's trajectory, so a procedure to resolve the orientation is needed. The brute force approach is to use a second camera and reconstruct the trajectories from both viewpoints. We can improve on this method because we know our particle shape in each experiment. The particles are simple enough to be modelled as a collection of spheres using Python. From there we can take projections of the particle and use least square regression to find the projection which maps it to an image from a single camera. On the next frame, another regression can be used to find the most likely orientation adjustment that leads from the previous frame to the current frame. The trajectory of the particles orientation can then be reconstructed from a single camera, but to get the full 3-D trajectory, a second camera would still be needed to recover all three spatial positions (x, y, and z). Design and implementation of the new experimental setup and data analysis methods is being undertaken by undergraduates in the lab, special thanks to Tony Li and Mingxuan Liu for their hard work. Our preliminary results (Fig. 2.10c and 2.10d) observe the predicted qualitative motion of chiral objects [42, 45, 46, 101], where their orientation spins continuously while sedimenting, leading to a periodic twirling motion.

Chapter 3

Experimental Investigations of Ice Mélange and the Flow of Floating Granular Materials

3.1 Introduction

Earth's landscape is continuously shaped by granular materials [6]. Natural examples include volcanic pyroclastic flows, avalanches, landslides, and sandstorms, but man-made materials such as plastic rafts and industrial waste are becoming increasingly important [115]. Granular materials can undergo sharp transitions between freely flowing and jammed states, accompanied by large variations in stress and a potential for catastrophic failure [56, 59, 60, 116–120]. Additionally, geophysical granular materials are often multiphase; they are strongly coupled to and transported by air or water [3]. Floating granular materials, such as logjams [75], river ice [121], sea ice [122], and volcanic pumice rafts [123], can jam in converging flows or narrowing geometries, and create hazards or ephemeral perturbations to the dynamics of Earth's aquatic interfaces. Even insects such as fire ants intentionally form granular rafts to

survive flooding [28]. Despite their ubiquity and importance, modelling floating granular materials remains a challenge due to the inherent difficulties in granular rheology [67] and the large variations in particle size and shape in geophysical environments [3].

Ice mélange is perhaps the world's largest floating granular material [15] and is formed from a polydisperse collection of broken icebergs, brash ice, and sea ice with "grain" sizes ranging from meters to kilometers. Ice mélange varies seasonally and exists in some form in most of Greenland's fjords. Approximately half of Greenland's ice sheet mass flux is accounted for by iceberg calving [124]. Greenland's ice sheet holds an ≈ 7 m worth of sea level increase, almost 10% of worldwide ice sheet mass. It is estimated that by 2100, the Greenland ice sheet will have contributed 79–167 mm of sea level rise, 30% to 60% of which is projected to come from calving at marine terminating glaciers [125, 126]. Importantly, remote sensing and field studies suggest ice mélange has a large impact on calving rates and the release of freshwater into fjords [11–17].

As tidewater glaciers are driven by gravity into the fjord, the terminus slowly pushes the buoyant ice mélange, compacting the granular material into a three-dimensional wedge. Resistance to flow is provided by rocky fjord walls or geometric constrictions. When granular materials are sheared, force chains between grains transmit stress from the boundary to the bulk [120]. In ice mélange, this manifests as a buttressing force on the glacier terminus, which can in turn impact glacial calving rates. Throughout the year, the changes in mélange properties and dynamics coincide with the retreat and advance of glacier termini. In the winter, the formation of sea ice leashes the loose iceberg clasts together, forming a rigid structure that inhibits glacier calving, allowing the advance of the glacier terminus [13, 16, 17]. In the spring and summer, when the ice melts, the mélange's ability to buttress is weakened, leading to more calving events, which increases the speed of glacial retreat [13, 16, 25, 127]. Pre-

vious studies have reproduced observed seasonal calving dynamics using models that prescribe periodic changes in the mélange buttressing strength [18–25]. However, this parameterization does not predict mélange buttressing strength from granular mechanics or from observed data.

While serious and sustained effort has gone into remote sensing and modeling of ice mélange, experimental work is limited [15]. Experiments allow us to break down the dynamics of ice mélange to the most important parameters, separating it from field conditions that have a coupled impact on its motion. More broadly, there are few studies describing how buoyant granular materials behave [128], and none that characterize internal or external stress. Ice mélange has a unique geometry in that one end is stress-free and open to the ocean, yet granular jamming still occurs further towards the glacier terminus. It is essentially an inverted granular pile. In granular piles after "run-out" ceases, gravitational body forces are balanced by internal stresses and friction at the walls and bottom of the containing vessel [129, 130]. Floating granular materials lack basal friction and only experience friction at the walls [128], yet their collapse and run-out behavior can be described quantitatively using a similar framework as dry granular materials. Zheng et al. [128] formed rectangular suspensions of millimeter-scale plastic beads held back by a removable lock gate. The experiments consisted of removing the gate and recording the run-out evolution of the pile until it reaches a nearly steady state, tracking the height and evolution of the front. One of the main findings was that the initial length of the rectangular pile influences the time it takes for the front of the pile to reach its steady state value, with longer lock lengths decreasing the rate of spreading. They found that there is a so-called "frozen" region near the closed end of the experiment where the height of the block does not change from its initial height. Yet the rectangular particle shape, wall friction, and quasistatic advancement of ice mélange make it distinct from run-out experiments where stress fluctuations aren't measured.

In this study we use laboratory experiments to simulate the quasistatic advancement of ice mélange in rectangular channels with frictional walls. In lieu of real ice, we fabricated centimeter-scale plastic buoyant particles which are then slowly pushed by a instrumented "glacier terminus" where forces can be monitored in real-time. Using simultaneous imaging from the side and from above, we extracted depth and surface velocity profiles across different particle shapes and frictional boundary conditions. We find that the most glaciological-relevant conditions, the thickness of the mélange at the terminus is sufficient to estimate the magnitude of the buttressing force, in agreement with recent field measurements [4]. However, the results can vary by a factor of 2-3 depending on the frictional wall condition (smooth vs. rough). Rough walls induce constant shear and rearrangements of the particles, whereas smooth walls lead to uniform plug flow. Additionally, we find that the thickness profile of the mélange along the length of the model fjord is well-described by a 1D, depth-averaged continuum model, which provides a prediction for the average buttressing force. However, the continuum model cannot capture the large force fluctuations, which are of the same magnitude as the mean force. The experiments are supported by granular DEM simulations, which show excellent agreement over multiple conditions. Our results suggest that the granular nature of ice mélange facilitates stochastic fluctuations in buttressing that can influence sub-seasonal controls on the timing and rate of iceberg calving.

3.2 Experimental Design and Methods

3.2.1 Experimental Methods

Figure 3.1 shows a schematic of our experimental setup. The model fjord was fabricated from cast acrylic and is 2 m long, 27 cm wide, and 30 cm in depth. The visible experimental viewing area is $\approx$ 1 m long, so there was an extra 1 m of space to allow

for particles and water to flow out of view. We performed experiments using both smooth, transparent acrylic walls, and removable, transparent, rough acrylic walls. The rough walls had a pattern of random packed, bi-disperse circles with diameters of 0.4 cm and 0.6 cm cut out using a laser cutter so that they acted like perforated sheets. This created a frictional surface where the corners and edges of particles were stuck, reducing slip at the walls. The perforated surface also allowed for imaging from the side to measure thickness profiles. We tested four particle shapes: irregular, spheres, rectangles, and squares. For the latter 2 particles, we are referring to their 2D cross-sections since they are both cuboids (Fig. 3.1b). All particles were made from polypropylene, which has a density similar to that of sea ice, 0.912 g/cm^3. The rectangular and square particles were laser cut to the specific shape and were 0.635 cm thick. The irregular particles were cut using a band-saw from bulk blocks of polyproylene, thus, their sizes were highly polydisperse, and ranged from 1.27 cm to 12.7 cm.

Our "glacier terminus" consisted of a cast acrylic plate and two shear strain sensors (Strain Measurement Devices, Inc.), as shown in Fig. 3.1a. The sensors were chosen for their rigidity and sensitivity, i.e., the terminus plate was solely fixed to the sensors using L-shaped brackets. This way the plate was only supported by the force sensors, and any extra force exerted on the plate was due to the mélange. The sensors were fixed to aluminum rails with L-shaped brackets, which were further attached to an aluminum rig that could freely slide back and forth. Linear motion of the terminus was achieved by use of an Arduino and two stepper motors. The rig had two tapped aluminum boxes, and two long threaded rods were fed into the boxes. The stepper motors were attached to the rods, and the speed of the terminus was then determined by the rotational speed of the motors. With this setup, the terminus speed, v_T, could be adjusted from 0.62 mm/s to 1.5 mm/s. Most experiments were performed at $v_T = 0.62$ mm/s. The Arduino and stepper motors were controlled by a custom

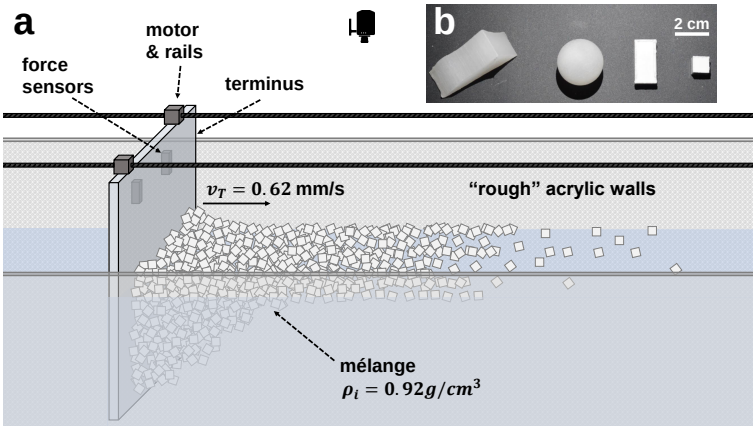

Figure 3.1: Cartoon diagram of our experimental setup. Panel **a** shows the whole setup. An acrylic plate acts as our "glacier" terminus. It is suspended by two sets of rails which are connected to stepper motors. We move the terminus at 0.62 mm/s. The terminus is connected to two shear force sensors (each rated up 10 N), which determine the total force on the plate by how much it gets deflected by the mélange. To both image the thickness profile of the mélange, and induce rearrangements and frictional forces from the walls, we fabricated our own "rough" acrylic sheets to act as our side walls. To image the mélange, we use two cameras, one positioned above to capture surface velocity fields, and one positioned on the side to capture thickness profiles. In panel **b**, we show examples of the types of particles used throughout our experiments. From left to right: Irregular, Spheres, Rectangles, and Squares. The irregular particles are not characterized, but range in size from 1.27 cm to 12.7 cm. Spheres have a diameter of 2.54 cm. Rectangles are 2.54 cm x 1.27 cm x 0.635 cm and squares are 0.953 cm x 0.953 cm x 0.635 cm.

LabView program (National Instruments). The voltage output of each force sensor was measured at 5,000 samples per second for 0.5 s, and the measurements were averaged to dramatically reduce noise and increase sensitivity. Thus the ultimate time resolution of our force measurements was 0.5 s. The strain sensors were calibrated using a pendulum with a known weight and an adjustable angle.

To image the motion of the mélange, we used two CMOS cameras whose time bases were synchronized. One camera was mounted 1.22 m above the mélange, and the other camera was mounted on a tripod approximately 1.83 m away. The camera frame-rate was fixed at 1 fps, and the resolution of each camera was 2048×2048 pixels. A large LED panel light was mounted on the back of the model fjord to facilitate imaging from the side. To synchronize the cameras to the force measurements, we applied a sharp impulse to the place that was visible in both cameras, and provided a reference time for both measurements. Profiles of the mélange from the side were extracted and processed using ImageJ Fiji [103]. Surface velocity fields were calculated using Lucas-Kanade optical flow techniques, implemented in Python using OpenCV [131, 132].

Each experiment consisted of filling the model fjord with fresh water until it reached a depth of 20 cm with the terminus submerged. The force measurement was then zeroed so that the force recorded was only due to the mélange. A large plastic plate was then placed at a angle of 27.5°, which initializes the mélange into a triangular wedge shape of length 36 cm and height 15 cm. The angle was arbitrarily chosen. We then poured the granular particles into the wedge where they formed a floating mélange. We kept the total mass of particles nearly the same in each experiment: 5.5 kg for squares and irregular particles, and 5.24 kg for rectangles. The large plate was then removed, and we initiated the terminus movement and synchronized the imaging and force measurements. The experiments ran for roughly 20 minutes while the mélange traversed the total length of the model fjord.

3.2.2 Glaciological Scaling

With any experiment intended to model geophysical phenomena, it is essential to compare the relevant dimensionless numbers. In particular, we compared several dimensionless numbers that determine the granular flow regime of our experiments in regards to field-scale ice mélange. The first number is the ratio between the typical size of an iceberg, d, to the width of the fjord, W. Using a typical iceberg size of $d \sim 25$ m, and the width of a large fjord such as Sermeq Kujalleq (Jakobshavn Isbræ), $W \sim 5$ km, the size ratio is $d/W \sim 0.005$. Using the smallest particle size in our experiments, $d = 0.953$ cm (squares), and the width of our model fjord $W = 27$ cm, the ratio $d/W \sim 0.035$. For the other two particle types, $d/W \sim 0.094$ (rectangles), $d/W \sim 0.047 - 0.470$ (polydisperse irregular). Thus, the most glaciologically relevant particle type is the smaller square particles, especially since jamming forces can increase significantly when d/W approaches unity [15]. In addition to size, there are dynamical dimensionless numbers as well. The buoyant particles near the surface will bob and rock at a specific frequency. This timescale should be compared to the motion of the terminus, i.e., the time it takes the terminus to move a typical particle size. The bobbing and rocking frequencies (f_{bob}, f_{rock}) of a buoyant, rectangular iceberg are given in Burton et al. [133]:

$$f_{\text{bob}} = \frac{1}{2\pi}\sqrt{\frac{g\rho_w}{d\varepsilon\rho}}, \tag{3.1}$$

$$f_{\text{rock}} = \frac{1}{2\pi}\sqrt{\frac{g(6\rho_i^2 - 6\rho\rho_w + \varepsilon^2\rho_w^2)}{d(1+\varepsilon^2)\rho\rho_w}}. \tag{3.2}$$

Here d is the dimension of the long edge of the rectangular iceberg, ε is the aspect ratio of the iceberg, g is the acceleration due to gravity, and ρ_w (ρ) is the density of water (ice). We define the quasistatic regime as the limit where $v_T/(df_{\text{bob}}) \ll 1$ and $v_T/(df_{\text{rock}}) \ll 1$. This means that the characteristic timescale for buoyant iceberg motion is much faster than the time it takes for the terminus to move by a distance d.

Since Eq. 3.2 depends sensitively on the geometry of the iceberg, we will only consider the bobbing motion for simplicity. Using Sermeq Kujalleq (Jakobshavn Isbræ) as an example again, we assume $v_T = 30$ m/day, $d = 25$ m, and $\varepsilon = 1$, resulting in $v_T/(df_{\text{bob}}) = 1.3 \times 10^{-4}$. For our square particles, $v_T = 0.62$ mm/s, $d = 9.5$ mm, and $\varepsilon = 1$, then $v_T/(df_{\text{bob}}) = 1.2 \times 10^{-2}$. Irregular and rectangular particles are similar or smaller than this value. Although the experimental value of $v_T/(df_{\text{bob}})$ is roughly two orders of magnitude greater than real ice mélange, both are much less than unity, implying that both lie squarely in the quasistatic regime. Amusingly, we note that the velocity of our model terminus, $v_T = 0.62$ mm/s, is equivalent to 54 m/d, close to the actual velocity of a fast moving glacier terminus.

The two aforementioned dimensionless numbers solely described the granular scale properties of the mélange and its relation to the movement of the glacier terminus without considering hydrodynamics. Possible hydrodynamic effects that could influence ice mélange motion include fluid drag and iceberg wave interactions [14, 133, 134]. In the water, the Reynolds number characterizes the ratio of inertial to viscous forces, $\text{Re} = \rho_w v_T d/\eta$. Here, η is the dynamic viscosity of water (≈ 1 mPa·s), and we have used the terminus velocity as the velocity scale. An typical iceberg moving at the velocity of the glacier terminus would result in a local Reynolds number of $\text{Re} \sim 10^4$. This indicates that flows are mostly turbulent. Using the square particles from our laboratory experiments, the Reynolds number is $\text{Re} \sim 10$, which indicates laminar flow. However, Re only characterizes the hydrodynamic regime of the flow, and doesn't indicate the strength of total forces on an iceberg. Instead, we use the Froude number (Fr), which measures the strength of drag forces on a partially submerged object to gravitational and buoyant forces. Defining $\text{Fr} = v_T/\sqrt{gd}$, the iceberg-scale Froude number is $\text{Fr} \sim 10^{-5}$, and for laboratory experiments, $\text{Fr} \sim 10^{-3}$. In both cases, $\text{Fr} \ll 1$, which means that hydrodynamic forces stemming from the slow advancement of the terminus are negligible. Thus, the surrounding water's role is es-

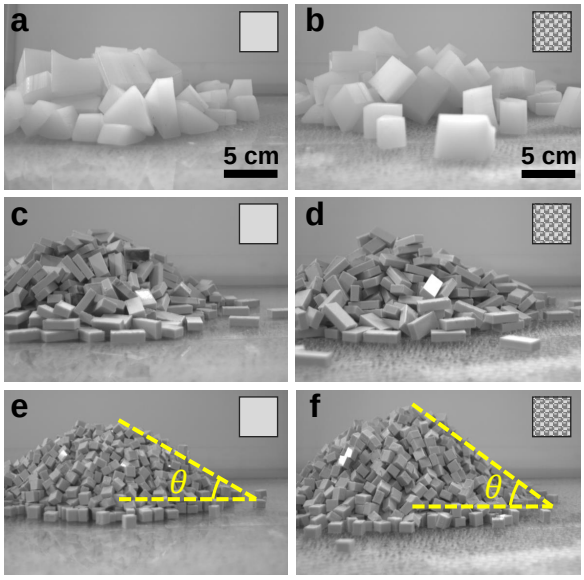

Figure 3.2: Images showing the angle of repose for three different particle types on both smooth and rough surfaces. The particles types (from top to bottom) were: irregular, rectangles, and squares. Panels **a**, **c**, and **e** show piles generated on smooth, acrylic surfaces. Panels **b**, **d**, **f** show piles generated on our fabricated "rough" acrylic surfaces. The angle of repose, θ, can be used to calculate a static coefficient of friction using Mohr-Coulomb theory: $\mu_p = \tan\theta$.

sentially a modified gravitational field (with buoyancy below the water line). For ice mélange, hydrodynamic forces will be important during rapid iceberg rearrangements or during iceberg calving [133, 134], which happen on a much higher velocity scale than terminus motion. These forces rapidly dissipate kinetic energy, but otherwise do not affect the quasistatic motion of ice mélange. Sub-glacial plumes that drive circulation in fjords could also apply hydrodynamic forces on individual icebergs [135], but we do not consider stratification in our current experimental study.

3.2.3 Friction in dense ice mélange

In dense granular materials, the maximum shear stress is proportional to the confining pressure, and the constant of proportionality is defined as a generalized friction coefficient, μ_p. However, μ_p depends on both material properties and particle shape. Highly irregular particles typically have a larger value of μ_p than spherical particles

due to interlocking [74, 83]. Additionally, there is a separate coefficient of friction at the wall of our model fjord, μ_w. Geometry also plays a role in determining frictional force by influencing the number of particle-wall contacts and the shape of the wall roughness. Thus, we employed two separate methods to characterize μ_p and μ_w. The first was a typical granular column collapse using equal masses (1 kg) of square, rectangular, and irregular particles confined inside a cylinder of radius 16 cm. Similar experiments have been used previously to measure internal friction in granular materials [130, 136]. We slowly removed the cylinder, which allowed the particles to spread radially outward and form a conical pile. We examined both the rough and smooth surfaces used as fjord walls in our ice mélange experiments. Figure 3.2 shows examples of the end state of the experiments where each pile was arrested and no longer flowing. We measured the approximate repose angle, θ, from the slope that the pile made with the horizontal surface, and interpreted it using Mohr-Coulomb theory to measure the friction coefficient: $\mu_p = \tan\theta$. We found that μ_p was nearly the same for smooth and rough surfaces, yet varied considerably with particle shape (Fig. 3.3a). This may be expected since μ_p is predominantly a measure on internal granular friction between particles. Square particles consistently had the largest μ_p. We suspect that this was mostly due to the ability of rectangular particles to align with their largest flat faces parallel to each other and the horizontal surface.

Our second method employed a simple sliding experiment to measure the maximum static friction between the particles and the walls of our chamber, albeit in a dry environment instead of a wet one. We filled a cylinder of radius 12.5 cm and mass 295 g with the following masses of particles: squares (345 g), rectangles (330 g), and irregulars (530 g). This was done on a 30 cm x 60 cm plate that was either rough or smooth, similar to the walls of the fjord in our ice mélange experiments. We then raised one end of the plate slowly using a jack until the column of material started to slide. We recorded the angle when sliding occurs, and using the force balance be-

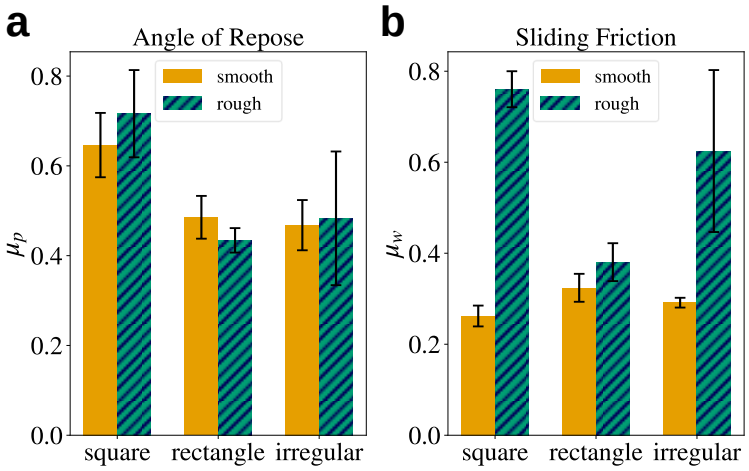

Figure 3.3: (**a**) Coefficient of internal friction ($\mu_p = \tan\theta$) measured using the angle of repose after the collapse of a granular column. (**b**) Coefficient of wall friction (μ_w) measured during sliding experiments in a confining cylinder. Solid colors in both panels represents friction measured on smooth surfaces, and hatched colors represent friction measured on rough surfaces. Error bars were calculated from 3 repeated experiments.

tween gravity and friction, we estimated the μ_w between the packed particles and the surface. This was done three times for each combination of particle type and plate friction. The data is summarized in Fig. 3.3b. On rough surfaces, the coefficient of friction was much higher, except for the rectangular particles. Again, we believe that this was because rectangles can easily align to the basal plane, resulting in less sharp corners penetrating the crevasses of the rough surface. The squares and irregulars did not align naturally, resulting in a much larger value of μ_w. Irregular particles had a larger error bar because the particles were much larger and polydisperse, leading to different contact patterns with the surface in different repeated experiments.

3.2.4 1D Depth-Averaged Model of Ice Mélange Thickness

Densely-packed granular materials transmit stress through individual contact forces between particles. Nevertheless, there have been many successful attempts to model granular materials using continuum approximations, often with complex, nonlocal

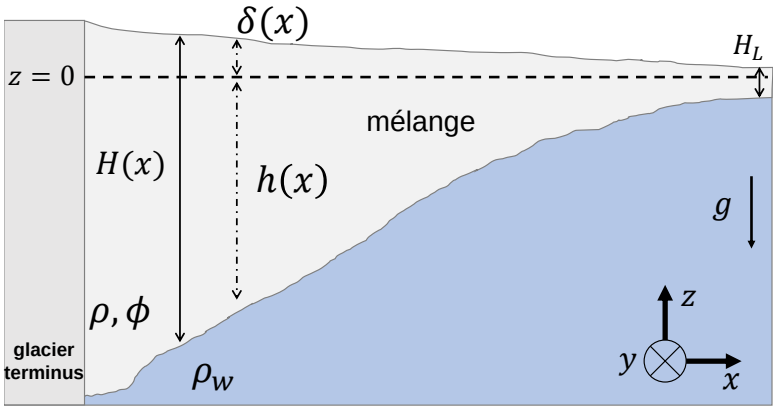

Figure 3.4: Diagram and visual description of the variables in our model. ρ and ρ_w are the densities of the ice and water respectively. ϕ is the packing fraction of the mélange. g is the magnitude and direction of the acceleration due to gravity. $\delta(x)$ is the height of the mélange above the water line, $h(x)$ is the depth of the mélange below the water line. H_L is the height of the mélange at its end, which is also the characteristic size of an iceberg in the mélange.

rheologies [12, 52, 60, 67]. The most relevant dimensionless number for determining the regime of granular flow is the inertial number,

$$I = \dot{\epsilon} d \sqrt{\rho / P}, \tag{3.3}$$

where $\dot{\epsilon}$ is the effective strain rate for the flow, ρ is the mass density of the packed granular material, and P is the average pressure. For the ice mélange in our experiments, $I \leq 10^{-3}$, meaning that the flow is well within the quasistatic regime, and inertial effects are small. Since granular rheologies typically have the effective friction coefficient (μ_p) increase with inertial number, we will assume that a roughly constant value of μ_p can capture the salient features of ice mélange flow.

In our experiments, the measurements of the thickness profiles of the ice mélange can be used to infer the frictional properties of the granular materials. To accomplish this, we developed a continuum, one-dimensional, depth-averaged model that provides a prediction for the thickness profile. The model is similar to other recent continuum models of ice mélange [4, 12]. Figure 3.4 illustrates the geometry and important

physical quantities in our model. Our approach is similar to Amundson and Burton [12], with a few updated assumptions and methods. The main assumptions of the model are: the flow is quasistatic so that the thickness profile doesn't change over time, the only driving stress is gravity, the fjord width W is constant, the packing fraction ϕ is constant, and the variation of pressure and thickness is small across with fjord width (y-direction) when compared to variations along the fjord length (x-direction). With these assumptions, the stress balance becomes

$$\frac{\partial \sigma_{ij}}{\partial x_j} = \rho \phi g_{\text{eff}} \delta_{iz}, \tag{3.4}$$

where σ_{ij} are components of the stress tensor, repeated indicies indicate summation, δ_{ij} is the Kronecker delta, and g_{eff} is the effective gravitational acceleration, which is different above ($g_{\text{eff}} = g$) and below ($g_{\text{eff}} = (1 - \rho/\rho_w)g$) the waterline. We also assume that the mélange is in hydrostatic balance, meaning that there are no vertical shear forces. With these assumptions, all components of the stress tensor are zero except for σ_{xx}, σ_{yy}, σ_{zz}, and σ_{xy}. The leading force balance equations then become

$$\frac{\partial \sigma_{xx}}{\partial x} + \frac{\partial \sigma_{xy}}{\partial y} = 0, \tag{3.5}$$

$$\frac{\partial \sigma_{zz}}{\partial z} = \rho \phi g_{\text{eff}}. \tag{3.6}$$

Solving for σ_{zz} is straightforward, and results in the following piece-wise expression:

$$\sigma_{zz}(x, z) = \begin{cases} -\rho \phi g (\delta(x) - z) & z \geq 0 \\ -(\rho_w - \rho) \phi g (h(x) + z) & z < 0 \end{cases} \tag{3.7}$$

We note that σ_{zz} is zero at the top (δ) and bottom ($-h$) of the fjord since granular contact forces are minimal here. The stress is largest right at the waterline ($z = 0$). In typical ice sheet models, the pressure in the material increases with depth, and is a

maximum at the lower boundary of the ice sheet [137]. However, because ice mélange allows water to intrude within the material, the contact forces already reflect the balance of gravitational and buoyant forces on each particle in the mélange.

We define the pressure with the trace of the stress tensor: $P = -(\sigma_{xx}+\sigma_{yy}+\sigma_{zz})/3$. We will refer to this as the "granular pressure" of our ice mélange. We then take the total stress tensor and partition it into the pressure and the deviatoric stress: $\sigma_{ij} = \sigma'_{ij} - P\delta_{ij}$, where σ'_{ij} is a traceless tensor. Because we are assuming the mélange is quasistatic, there are no deformations to the length or thickness, and thus $\sigma'_{xx} = \sigma'_{yy} = \sigma'_{zz} = 0$. Using these facts, we can rewrite Eqs. 3.5 and 3.6 as:

$$\frac{\partial \sigma'_{xy}}{\partial y} = \frac{\partial P}{\partial x}, \tag{3.8}$$

$$P = -\sigma_{zz} = \begin{cases} \rho\phi g(\delta - z) & z \geq 0 \\ (\rho_w - \rho)\phi g(h + z) & z < 0 \end{cases}. \tag{3.9}$$

The total height of the mélange is $H(x) = \delta(x) + h(x)$, and since we know that the pressure must be continuous at $z = 0$, we can solve for both δ and h in terms of the total thickness H. After some algebra, we arrive at $\delta(x) = H(x)(\rho_w - \rho)/\rho_w$ and $h(x) = H(x)(\rho/\rho_w)$. To proceed further, we depth average both equations by integrating over z from $-h$ to δ:

$$\int_{-h}^{\delta} \frac{\partial \sigma'_{xy}}{\partial y} dz = \int_{-h}^{\delta} \frac{\partial P}{\partial x} dz. \tag{3.10}$$

For the left-hand side of Eq. 3.10, the we can easily switch the order of integration and differentiation. However, because δ and h are functions of x, we need to be careful with the right hand side. Using the Leibniz rule in this case, we can also switch the order of integration and differentiation since P is zero at $z = \delta$ and $z = -h$. Defining

the depth averaged quantities, $\bar{\sigma}_{xy}$ and $\bar{P}$, the result is

$$\bar{\tau}_{xy} = \frac{1}{H}\int_{-h}^{\delta} \tau_{xy} dz, \tag{3.11}$$

$$\bar{P} = \frac{1}{H}\int_{-h}^{\delta} P dz = \frac{1}{2}\rho\left(1 - \frac{\rho}{\rho_w}\right)\phi g H, \tag{3.12}$$

$$\frac{\partial\left[H\bar{\tau}_{xy}\right]}{\partial y} = \frac{\partial\left[H\bar{P}\right]}{\partial x}. \tag{3.13}$$

Because we assume $H(x)$ and $\bar{P}(x)$ do not vary with y, we can immediately integrate our equation over the y direction. On the right hand side of Eq. 3.13, we pick up a factor of W. The left hand side can be readily integrated, resulting in $H\left(\bar{\tau}_{xy}|_{\frac{W}{2}} - \bar{\tau}_{xy}|_{-\frac{W}{2}}\right)$. To further solve for $H(x)$, we need to introduce a relationship between $\bar{\tau}_{xy}$ and $\bar{P}$. The simplest granular rheology to relate these quantities requires the shear stress to be proportional to the pressure with a single, unchanging friction coefficient. Thus, we choose the relationship $\bar{\tau}_{xy}(\pm W/2) = \mp\mu_w \bar{P}$, where μ_w is the friction coefficient at the wall, and the shear stress points in the negative x-direction, since the mélange is being quasistatically advanced forward. Finally, using the fact that $\bar{P} \propto H$, we arrive at the final equation and solution for the thickness profile $H(x)$:

$$-\frac{2\mu_w}{W}\left[H\bar{P}\right] = \frac{\partial\left[H\bar{P}\right]}{\partial x}, \tag{3.14}$$

$$H(x) = H_0 e^{-\frac{\mu_w}{W}x}, \tag{3.15}$$

where H_0 is the thickness at $x = 0$. This simplified model shows that the thickness of a quasistatically-pushed, three-dimensional ice mélange should vary exponentially along the length of the fjord. Our continuum model also suggests that the mélange thins indefinitely and reaches zero thickness, yet real granular materials have a finite grain size, and the mélange can never be thinner than the characteristic iceberg size d. We note that given Eq. 3.14, the relationship between thickness and pressure

(Eq. 3.12) cannot be altered to have $\bar{P} \to 0$ at finite thickness H since the product $H\bar{P}$ must follow an exponential, which only tends to zero at $x = \infty$. Alternatively, one can alter the simple rheology at the walls ($\bar{\tau}_{xy}(\pm W/2) = \mp\mu_w \bar{P}$) to account for the finite grain size near the end of the mélange. In Amundson and Burton [12], the rheology was altered to introduce a stress at the end of the mélange ($x = L$) to fix the thickness. In Burton et al. [15], the rheology was altered by introducing a finite shear stress at the end of a two-dimensional mélange so that the shear stress was larger than the pressure. This was motivated by the Janssen effect in grain silos [138], where the pressure saturates at increasing depths, and friction supports the weight of the material. Here, we make an empirical modification to Eq. 3.15 by adding a constant, d, that represents the mélange thickness at infinite distance, which should ultimately be the same as the grain size. This allowed us to fit all of the data uniformly. As we will show, this simple exponential fit is sufficient for the experimental data, and results in measured friction coefficients that mostly agree with our independent sliding experiments, shown in Fig. 3.3.

3.3 Results and Discussion

3.3.1 Experimental Mélange Thickness Profiles

In the field, direct visual measurements of the thickness profile of ice mélange are impossible. The freeboard height, δ, can be related to the total thickness assuming a hydrostatic balance in our model, $\delta(x, y) = H(x, y)(1 - \rho/\rho_w)$. This relationship has been used to estimate ice mélange thickness in an number of studies [4, 70, 139]. In our experiments, we can image the thickness profile and its time evolution over a distance equivalent to ~ 100 particle lengths. Figs. 3.5a-3.7a show a time-lapse of the thickness profile during a representative experiment for three different particle types. Figure 3.5a also shows the initialization state of the ice mélange, which is

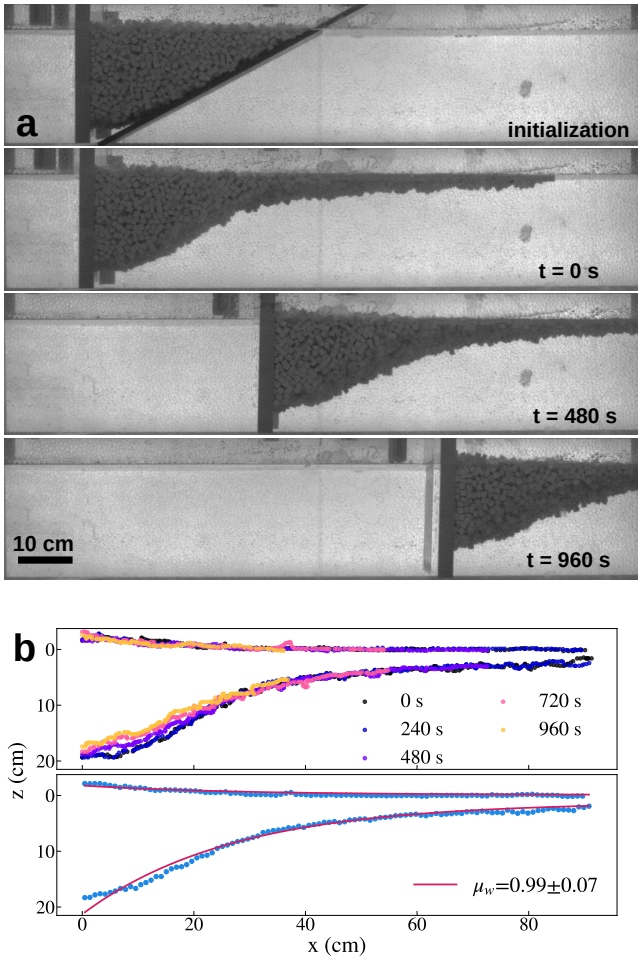

Figure 3.5: Evolution of the mélange thickness profile and fitting with our 1D model for square shaped particles. Panel (a) are raw experimental images at the given timestamps with initial mélange structure shown at the top. Panel (b) shows the extracted thickness profile for five timesteps (top) and the resulting binned data (blue dots) with a best fit curve for μ_W from Eq. 3.15 (solid red) on the bottom.

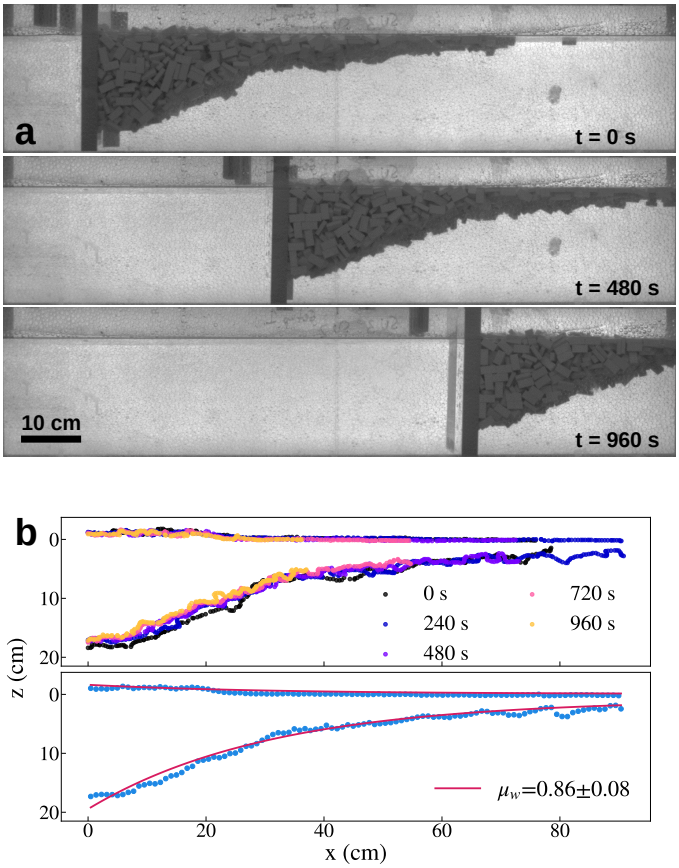

Figure 3.6: Evolution of the mélange thickness profile and fitting with our 1D model for rectangular shaped particles. Panel (a) are raw experimental images at the given timestamps. The initial mélange structure is the same as shown in Fig 3.5. Panel (b) shows the extracted thickness profile for five timesteps (top) and the resulting binned data (blue dots) with a best fit curve from Eq. 3.15 (solid red) on the bottom.

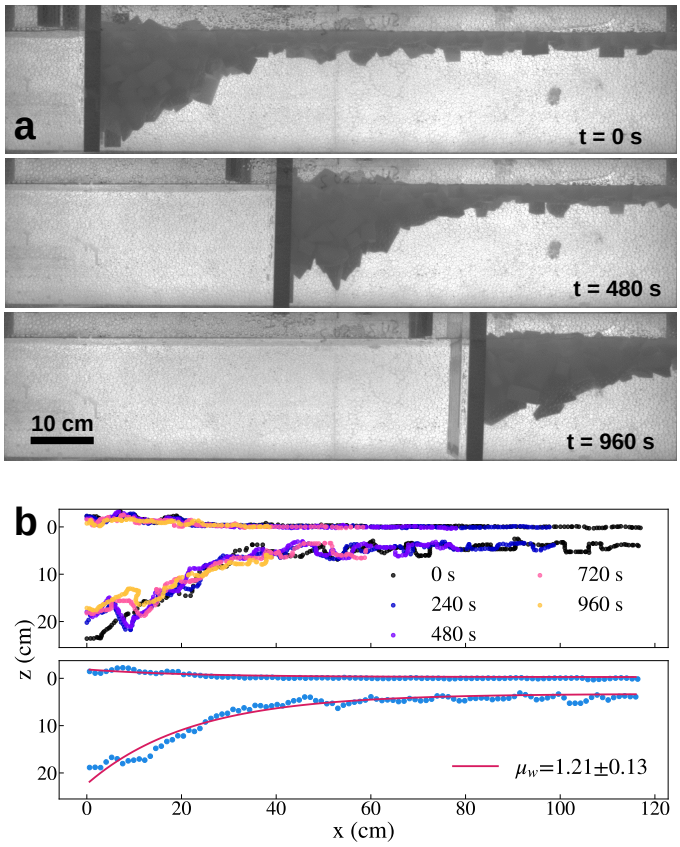

Figure 3.7: Evolution of the mélange thickness profile and fitting with our 1D model for irregularly shaped particles. Panel (a) are raw experimental images at the given timestamps. The initial mélange structure is the same as shown in Fig 3.5. Panel (b) shows the extracted thickness profile for five timesteps (top) and the resulting binned data (blue dots) with a best fit curve from Eq. 3.15 (solid red) on the bottom.

the wedge shape described in section 3.2.1. There are a few important observations that are illustrated by the images. The mélange thickness decreases slightly across the duration of the experiment, but eventually tends to a steady-state. Consistently, there is a bulge in the shape near the terminus. There are two reasons for this. There is a yield stress that the granular material must overcome to deform, and this can affect its shape near the terminus, similar to what has been observed in floating granular collapse experiments Zheng et al. [128]. Also, the region near the terminus is being pushed uniformly, and as a consequence, must have a different velocity profile across the width of the fjord. This will be discussed in more detail in section 3.3.2.

Figures 3.5b-3.7b shows thickness profile data and fits produced by Eq. 3.15, with the correction for the grain size:

$$H(x) = (H_0 - d)e^{-\frac{\mu_w}{W}x} + d, \tag{3.16}$$

In each figure, the top graph shows profiles of the mélange at different points in time. These curves are the functions $\delta(x)$ and $-h(x)$, assuming hydrostatic balance. The data was acquired by clicking off points in the images using ImageJ software [103]. The blue data in the bottom graph are the binned and averaged data of all profiles in the the top graph, and are used to fit Eq. 3.16. The fit is good, but shows systematic deviations near the terminus, as expected since the shear stress at the fjord walls must be different near the terminus, i.e. the mélange must move with the terminus uniformly. The fitted values of μ_w show qualitative agreement with μ_w measured using sliding and angle of repose experiments (Fig. 3.3). However, all fit values for μ_w were proportionally larger than the measured values from Fig. 3.3b. Although, the motion of the melange near the fjord walls is not pure sliding, as in Fig. 3.3. For example, if there is no-slip on the walls, then the wall friction similar to a static coefficient of friction. This coefficient would generally be larger than a

sliding or kinetic coefficient of friction. The particles also rotate significantly when sheared near the wall, which is not present in the sliding experiments. Overall, the model shows reasonable agreement with salient features of the experimental profiles, and provides a way to estimate frictional parameters from thickness profiles alone.

3.3.2 Surface Velocity Fields

Granular materials are known to display large fluctuations in velocity as they are quasistatically deformed. This is an indication that the material is jammed. Stress is built up and subsequently released through rapid rearrangements of the individual particles. Ice mélange displays similar behavior, as evidenced by stochastic fluctuations in lab experiments [15], and dynamic "jamming waves" observed after calving events in field data [140]. In some cases, the surface velocity fields in real ice mélange can predict the timing of calving events [14]. In our experiments, we examined the velocity fields from above to quantify this behavior, and to directly compare to the measured force on the terminus. In the field, velocity fields can be measured using portable radar interferometers, which provide centimeter-scale resolution of iceberg displacements on timescales of minutes [14, 140]. Velocity fields can then be extracted from these measurements. In our experiments, image analysis alone makes it challenging to track individual, box-shaped icebergs with an equivalent level of precision. As stated above, our velocity fields were calculated using PIV implemented with Lucas-Kanade optical flow. Briefly, optical flow can track features in an image (i.e., the corners of particles high contrast exists due to shadows) over a given number of frames, and assigns a displacement track to that feature. We can then interpolate the set of all feature velocities at a particular frame, using the pixel resolution of the image as our interpolation grid.

For all of our velocity fields, we track features over 20 frames, and we repeat the calculation every 5 frames. A typical view from above and the corresponding velocity

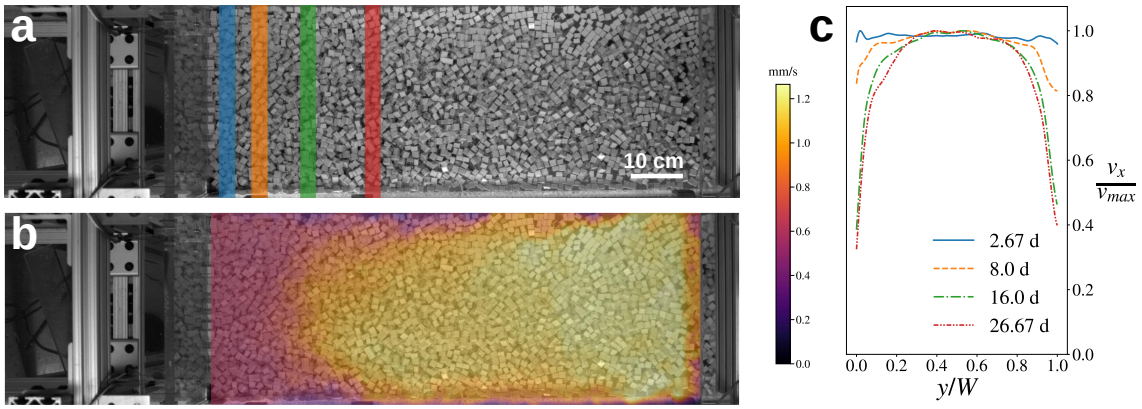

Figure 3.8: Process of calculating the across fjord velocity profile transects for different fixed distances from the terminus. Panel **a** shows the distances at which the corresponding colored transects are calculated. Each transect is 2.54 cm in width, and the distances from the terminus are in the legend of panel **c**. Panel **b** shows the velocity field at the same time point as panel **a**. Panel **c** are the velocity profiles at each corresponding transect distance. Velocity profiles are averaged over the whole experimental trajectory, and then normalized by the maximum value along the transect.

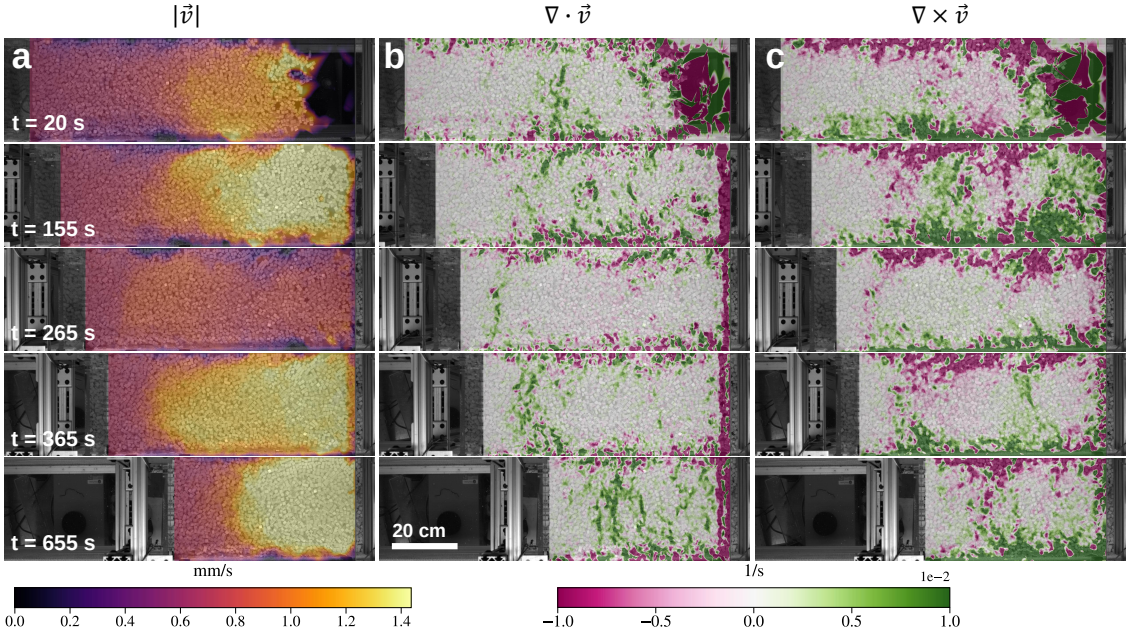

Figure 3.9: Representative images of velocity, divergence, and curl fields for a chosen experiment. Column **a** shows velocity fields, column **b** shows the divergence, and column **c** shows the curl. Images shows mélange experiences periods of slow compression followed by large extension, likely due to relaxation from rearrangements of particles. Velocity color bar is in units of mm/s, and the divergence and curl color bar is in units of 1/s scaled by $1x10^{-2}$.

magnitude for square particles is shown in Fig. 3.8a-b. Across-fjord velocity measurements can reveal the degree of shear near the fjord walls, and near the terminus. This was done at different distances from the terminus since similar measurements can be made on ice mélange in the field using satellite imagery. Figure 3.8a indicates the different distances where across-fjord profiles were calculated. The velocity profiles are calculated at each frame, then averaged over the entire experiment. We plot the longitudinal velocity, v_x, as a function of lateral position in y in Fig. 3.8c. Near the terminus, the flow of the mélange is more plug-like (blue and orange curves) since the particles near the terminus are fixed to move at the terminus velocity. There is a transition zone where shear develops near the fjord walls further down the fjord. Qualitatively, the size of the plug-flow region should scale with the particle size, and should be inversely related to the fjord width. Further down the fjord, the frictional shear bands near the wall lead to an increase in velocity in the middle of the fjord. Similar profiles were predicted from simplified models of quasistatic flow, but depended somewhat on the granular rheology used [12]. The predictions depended on a number of parameters, including slip at the wall, and thus here we are not able to distinguish between different potential granular rheologies from velocity profiles alone.

Importantly, although the velocity profiles in Fig. 3.8c are averaged over the entire experiment, the velocity displays large fluctuations during an experiment; fluctuations that cannot be captured using a continuum model. Figure 3.9a shows the velocity magnitude of the mélange at different times using square particles. The behavior varied between almost plug-flow for the whole length of the mélange ($t = 265$ s), to a state showing a transition between plug and shear-dominated flow ($t = 655$ s). To better understand the spatial variability in velocity in x and y, we plot the derivatives of our velocity fields to highlight areas of activity and showcase the inhomogeneity and stochastic nature of granular materials. Figure 3.9b shows the two-dimensional

divergence, and column 3.9c shows the two dimensional curl. In the divergence, magenta colors show areas of compression, and green colors show areas of extension in the mélange. The far right-hand side of all images show large numerical values of the fields, but this is an experimental artifact caused by either the lack of dense particles (t = 20 s), or the lack of visibility near the right side of the frame. Generally, across the whole mélange there is a slight magenta tone, indicating an overall compression. As the mélange advances, the compression is punctuated by pockets of deep green color, indicating rapid extension. We interpret this as a slow build-up of compressional stress, which is constantly being relieved by extensional rearrangements of particles. This stick-slip motion is typical of quasistatic granular flows [141, 142], cannot be captured in continuum models, and leads to stochastic fluctuations in the forces that the mélange applies on the terminus [15]. Similar heterogeneous behavior is observed in the curl of the velocity (Fig. 3.9c). Near the terminus, there is a uniform color due to the plug-like flow, and further down the fjord there are opposite colors on the walls due to the localized frictional shear. Additionally, the center of the mélange is punctuated by regions of opposite vorticity that can span the width of the fjord (t = 155 s).

3.3.3 Buttressing Strength and Fluctuations

One of the largest potential feedbacks from the presence of ice mélange on the glacier terminus is its mechanical buttressing force. For example, the buttressing force (or local stress) can influence the rate of iceberg calving [4, 12–14]. However, time evolution of the total mélange stress on real tidewater glaciers is impossible to measure in the field, and can only be estimated from continuum models or observations of the freeboard height of ice mélange [4]. In contrast, although experiments are down-scaled and idealized, they allow direct and dynamical measurements of the buttressing force generated by ice mélange. In our 1D continuum model, $\sigma_{xx} = -P$, and the pressure

can be deduced directly from the thickness at the terminus (Eq. 3.12). Thus, the total force on the terminus should be proportional to the total pressure multiplied by the contact area between the mélange and the terminus:

$$F_0 = \bar{P}(x=0)H_0W = \frac{1}{2}\rho\left(1-\frac{\rho}{\rho_w}\right)\phi g H_0^2 W, \tag{3.17}$$

where H_0 is the thickness of the mélange at $x = 0$. As discussed in Meng et al. [4], ϕ and H_0 are the two parameters that control the variability in the buttressing strength of ice mélange. This expression for F_0 and visual observations of the evolution of H_0 (Fig. 3.5) implies that the force should be relatively constant or change slowly throughout the experiment.

Figure 3.10a shows the normalized average surface velocity of the mélange, and the normalized total force on the terminus versus distance traveled down the fjord. Data is shown for both smooth and rough walls. The velocity generally fluctuates around the terminus velocity, which is expected since the flow is quasistatic and the length of the mélange doesn't change during the experiment. These fluctuations aren't present when the walls are smooth, indicating that granular rearrangements from frictional shear at the walls drive variations in mélange velocity. Importantly, similar large fluctuations can be observed in the force on the terminus. These fluctuations can be 50% or more of the average force. While the correlation is small between force and velocity is small (Pearson correlation coefficient 0.3), we note that there is a qualitative inverse relationship between the two. For example, at roughly $x/W = 1.5$, we see a sharp peak in velocity with a corresponding dip in the force. We emphasize that these fluctuations cannot be captured by continuum models of ice mélange, i.e., they lack the ability to account for short time rearrangements and localized deformations of the mélange. For the square particles in Fig. 3.10a, the average force when rough walls are present agrees well with the continuum prediction ($F \approx F_0$), suggesting that a

continuously sheared mélange is sufficiently fluid and explores jammed configurations that on average agree with a depth-averaged, hydrostatic continuum model.

In contrast, the dashed line in Fig. 3.10a shows that smooth walls always produce a buttressing force smaller than F_0, in this case it is only half as large. Without the increased friction provided by wall roughness, the system can get stuck in static frictional states where the force on the terminus is small. We believe a process similar to the Janssen effect [138] causes the pressure to saturate before the terminus, caused by the bridging of mélange particles across the width of the fjord. When the amount of shear increases, the mélange can explore more configurations, and thus fluctuates around the continuum prediction. A similar decrease in the mélange's buttressing strength can be seen when we change the particle shape (Fig. 3.10b and 3.10c), but now the disparity occurs with both smooth and rough walls. Figure 3.3 demonstrates the decrease in friction when the particle shape is changed, which supports the prediction that when the friction is low enough, the amount of shear and rearrangments decreases, which causes the Janssen effect to emerge. These results indicate that our continuum theory agrees well when the mélange is well sheared, but seems to be only an upper bound when the mélange is in a plug flow regime.

Finally, we want to ensure that we are truly within the quasistatic regime, so that our assumptions hold true. Granular materials within the quasistatic regime should have dynamics that are qualitatively independent of shear rate, so if we increase the velocity of our terminus, then the overall dynamics of our mélange shouldn't change. This is exemplified in Fig. 3.11, where we plot the forces from a typical experiment (blue) and forces from an experiment at roughly double the speed (red). Fig. 3.11a shows the force as a function of distance travelled down the fjord, scaled by the predicted mean force from our continuum 1-D model. Visually, the fluctuations don't look too different between the two curves. To verify, we plotted the histograms of the forces in Fig. 3.11b. While the distribution for the higher velocity experiment is a bit

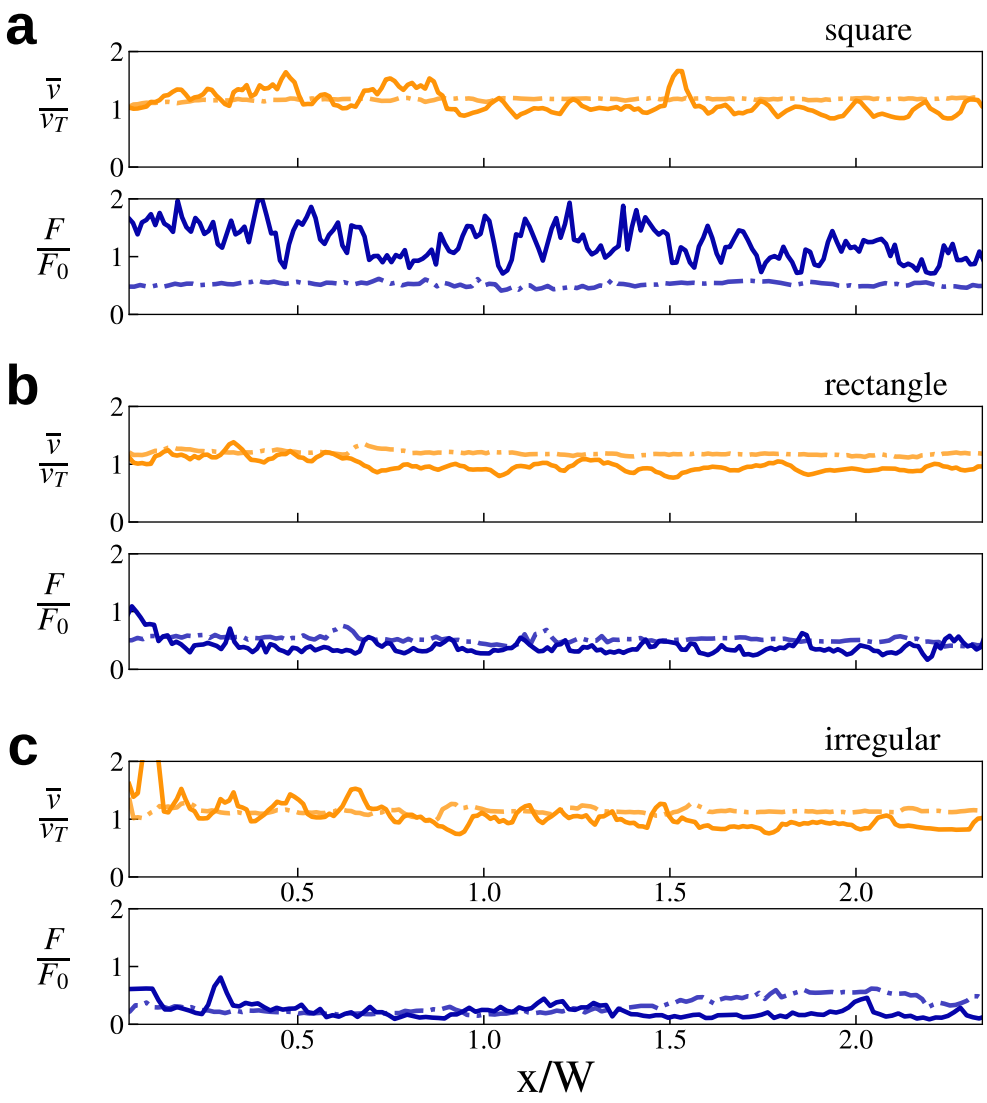

Figure 3.10: Velocity and force time traces for our three particle types. Solid lines are for experiments using rough fjord walls, dashed lines are experiments using smooth fjord walls. Velocity plotted is the average velocity at a given time step over the area of our mélange that is viewable divided by the terminus velocity. Forces are scaled by the predicted buttressing force F_0 (Eq. 3.17); squares - $1.42N$, rectangles - $1.49N$, irregular - $1.36N$.

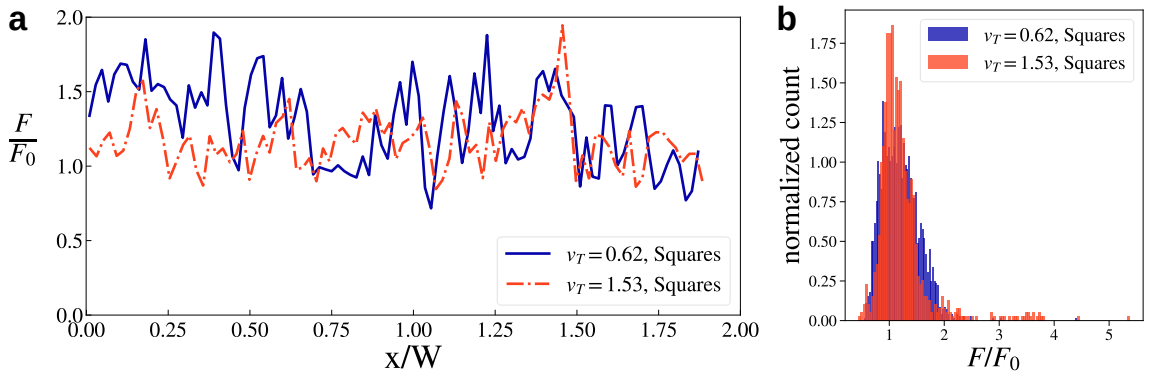

Figure 3.11: **a** Normalized force on terminus versus distance traveled down fjord. Solid line represents slower terminus speed (v_T=0.62 mm/s), dotted line represents faster terminus speed (v_T=1.53 mm/s). **b** Histograms of the forces normalized by the predicted buttressing strength from our continuum model (Eq. 3.17). The area of each distribution is normalized to one.

narrower and extends a bit further, the mean of the two distributions is roughly the same. We would expect with higher shear rate that the mean force would increase if we were outside the quasistatic regime, so we safely assume that the mélange is quasistatic.

3.3.4 DEM Simulations of Ice Mélange

Our experiments provide a controllable environment to explore the most salient and important features that influence the dynamics of ice mélange and its buttressing force on glacier termini. However, due to limitations in particle fabrication, we are unable to produce a mélange with the same type of iceberg size distributions that are seen in fjords of marine terminating glaciers [2, 70]. Our fabrication techniques were constrained by the melting of the polypropylene plastic, and particles on the lower end of the distributions found in nature could not be cut effectively without risk of fires. Simulations can be used to explore situations that are too difficult for laboratory experiments to undertake. To rectify this limitation of our experimental work, I collaborated with Professor Ching-Yao Lai and Dr. Olivia Meng to develop a suite of 3D discrete element method (DEM) simulations. By comparing the DEM simulations

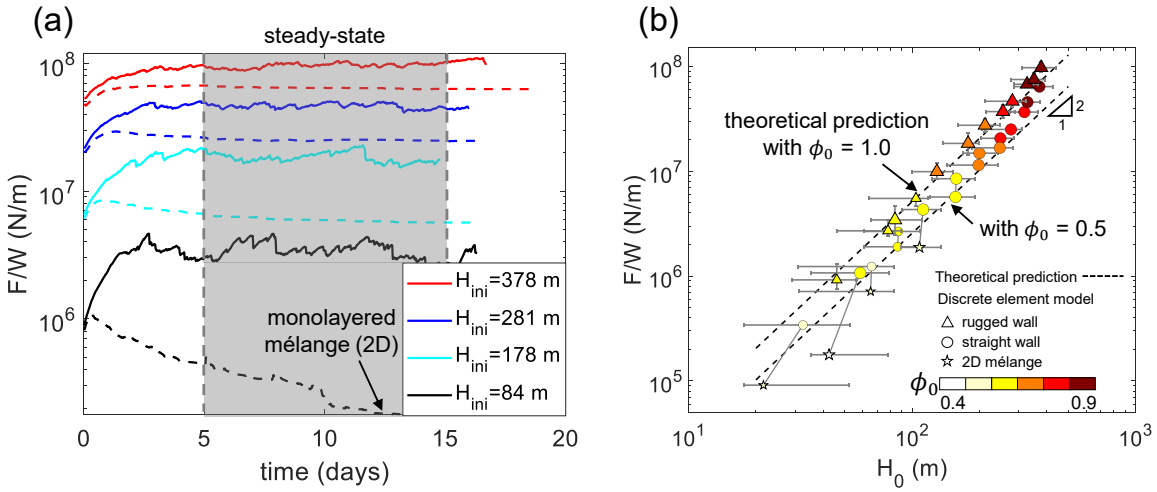

Figure 3.12: Adapted from Meng et al. [4]. Results from field scale DEM simulations of ice mélange performed by Meng et al. [4]. (a) Width averaged buttressing force on the terminus (F/W) versus time. The colors correspond to different initial mélange thicknesses. The dashed lines represent smooth fjord walls, solid lines represent rugged fjord walls. The mélange appears to be in a steady state after 5 days, except for the thinnest mélange ($H_{ini} = 84$ m). (b) Buttressing strength as a function of steady state mélange thickness, H_0. Dashed lines represent theoretical predictions of the steady state force (Eq. 3.17) with varying packing fractions. H_0 is the average thickness over a 200 m slice of the mélange in front of the terminus. All averaged calculations are done within the 5 - 15 days time period to ensure the mélange is in the steady state. Triangles represent rugged walls, circles represent smooth walls, and stars represent mélange that has thinned to a 2D monolayer.

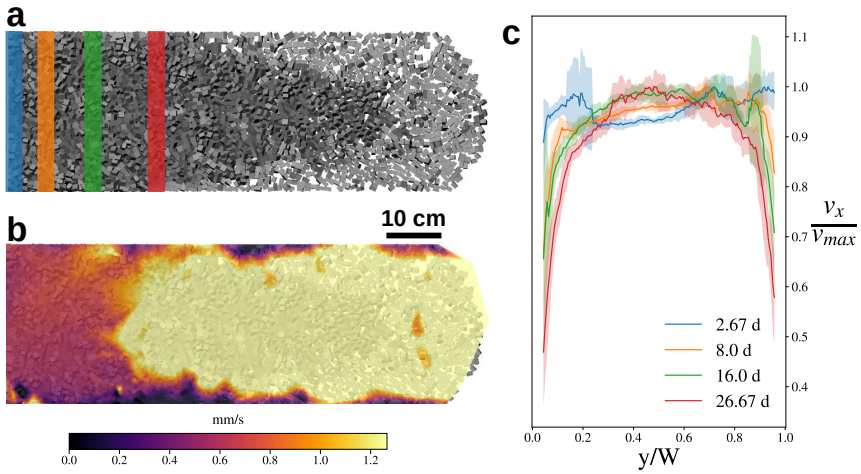

Figure 3.13: Across fjord velocity profiles from DEM simulations by Meng et al. [4]. Panels **a** shows the distances at which across fjord velocity profiles are calculated. Each transect is 2.54 cm in width, and the center of the transect along the x direction are indicated in terms of characteristic iceberg sizes d in the legend of panel **c**. Panel **b** shows a representative velocity field at the same time point as panel **a**. Panel **c** shows the resulting across fjord velocity profiles for each distance. The curves are calculated by first calculating the average velocity across a transect at a given y position for each timestep of the simulation. This provides a single across fjord velocity profile at a given time, which is then averaged over the entire simulation. Solid curves represent the average over the whole simulation, and the shaded in area represents one standard deviation of the velocity.

with our experiments, we can validate our continuum 1D model of ice mélange using parameters from the field. This work resulted in a collaborative publication [4]. In the simulation, icebergs are modelled as cubic particles that follow a power law distribution in their size, in accordance to observed icebergs size distributions [2, 70]. The terminus is modelled as a flat surface with velocity 43.2 m/day [15, 143]. The fjord is a 1 km wide straight channel open on one end that is either smooth (constant width) or has a series of bulges which are intended to explore the effect of friction on mélange buttressing force. These bulges are squares that are 60 m wide, 20 m thick, and are spaced 150 m apart. The initial length of the mélange is always 3 km. The initial thickness of the mélange is varied from 30 m to 380 m to determine the influence of mélange thickness on the buttressing force. The simulations are ran for an equivalent of 16 days so that a steady state of mélange is reached. They found that thin mélange evolved into 2D monolayers without sufficient wall friction, as seen in the dashed black curve in Fig. 3.12a. Figure 3.12b demonstrates the predicted scaling of buttressing strength with mélange thickness and packing fraction from Eq. 3.17. As seen in our experiments, smooth walls consistently had a lower averaged buttressing force than rough walls.

Meng et al. [4] also ran experiment scale simulations to cross validate their simulations and our experiments. The simulations have the same dimensions as our experimental setup, however the roughness on the walls is now instead a uniform grid of square bulges that are 0.5 cm wide, extend 0.2 cm from the walls, and are spaced 0.4 cm apart. Simulations are run for 1200 seconds, roughly the same amount of time an experiment runs. Only two particles were explored, squares and rectangles. Our irregular particles were difficult to parameterize in the DEM simulations, so no simulations were run using that particle shape. The terminus speed, initial mélange shape, and simulation domain size are the same as our experiments. Qualitatively, the DEM simulations show great agreement with our experiments, and support the use

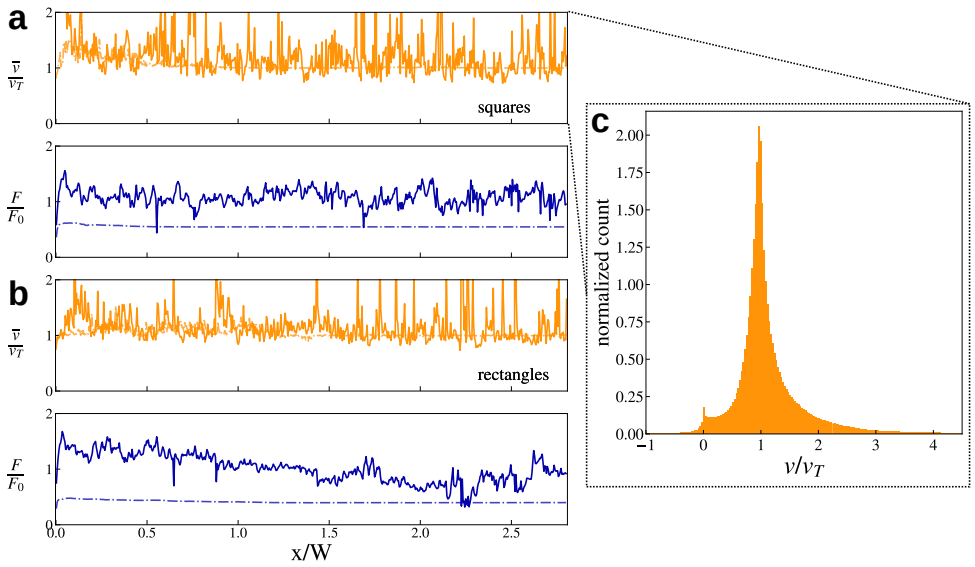

Figure 3.14: Velocity and force versus distance down the fjord from DEM simulations by Meng et al. [4]. Solid lines are simulated velocities and forces for rough fjord walls, dotted lines are for smooth fjord walls. The terminus velocity is equal to $v_T = 0.62$ mm/s. Forces are scaled by the predicted buttressing strength (Eq. 3.17) at the terminus. (a) Velocities and forces for square particles. (b) Velocities and forces for rectangular particles. (c) Histogram of velocities of square particles in a fjord with rough walls. The histogram is normalized so that the sum of the area of the histogram is equal to one.

of their scheme in the field scale simulations. The simulation can track the individual positions, velocities, contact numbers, and stress tensor of each particle. Figure 3.14 compares the velocities and forces of the mélange in the DEM simulations, akin to Fig. 3.10. We note that the velocities here are velocities of all particles above the waterline, which is not the same as the velocity of the surface. In Fig. 3.13 we demonstrate results similar to Fig. 3.8. We are again calculating surface velocity fields (Fig. 3.13b) and calculating across fjord velocity profiles (Fig. 3.13c). We are showing profiles for square particles. Across fjord velocity profiles show the same transition from plug flow to shear banded flow profiles as we saw in Fig. 3.8. Figure 3.14 shows the normalized average surface velocity of the mélange, and the normalized total force on the terminus versus distance traveled down the fjord for both smooth (dotted curves) and rough (solid curves) walls. Once again we see that fluctuations dominate the dynamics when roughness (and thus shear at the walls) is increased. However the magnitude and frequencies of these fluctuations is greatly increased in the simulation data. To visualize these fluctuations, we plotted the distribution of particle velocities in Fig. 3.14c. As the terminus is pushing the mélange in the positive x-direction, we expect the velocities to be centered around the terminus velocity, with a skew towards velocities greater than the terminus velocity, and a small amount of negative velocities. Because velocities are averaged across the mélange every time step, the large spikes must be accounted for by particles with velocities significantly higher than the terminus velocity. What causes some particles to achieve these erroneous velocities in the simulations is currently unknown. We also see a roughly 50% decrease in the average terminus force when smooth walls are used, indicating that the simulations can capture most of the relevant phenomenon of our experiments. One discrepancy is that for rectangular particles (Figure 3.14b) the simulated force is larger than the experiments. It is unclear what causes this difference in behaviour, but we know that the simulations do not include gravitational torques due to buoyancy

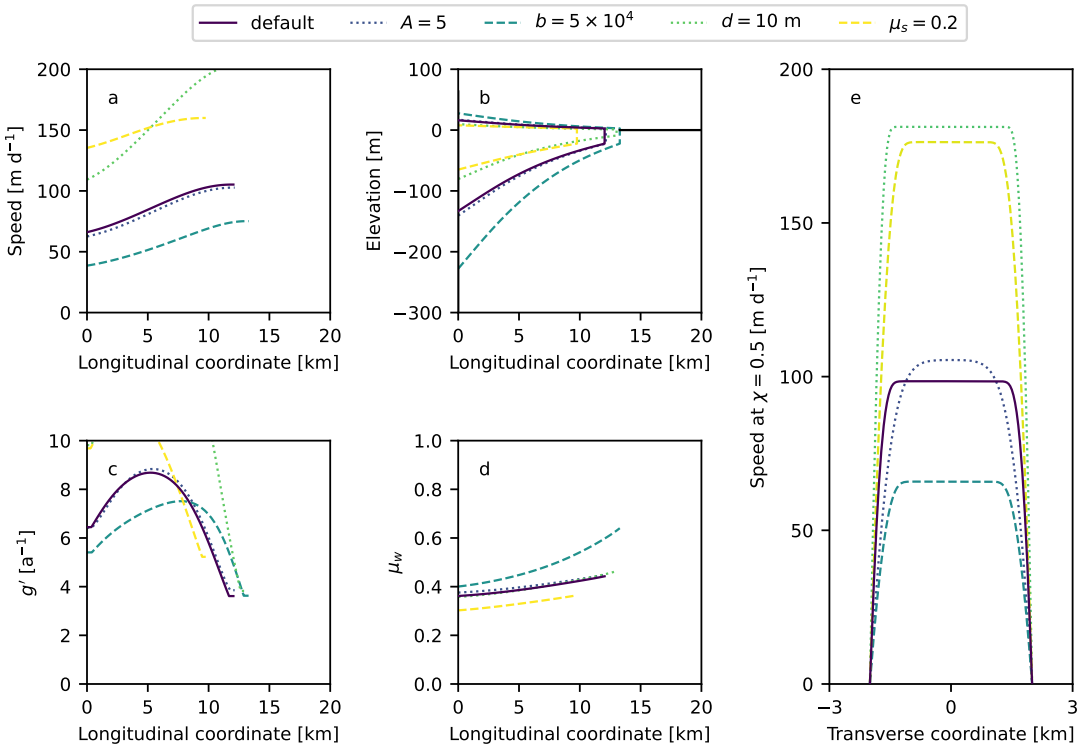

Figure 3.15: Adapted from Amundson et al. [5]. Steady state profiles of the (a) velocity, (b) thickness, (c) fluidity, (d) wall friction μ_w, and (e) across fjord velocity profiles for various choices of non local granular rheology parameters. Default value curves ($A = 0.5$,$b = 1 \times 10^4$,$d = 25$,$\mu_s = 0.3$) are shown in solid purple. Different parameter values are listed in the legend. For each curve, the default values are held constant and the parameter of interest is changed.

in the relaxation of particles. The difference in dynamics might lead to rectangular particles not aligning with the walls as we see in our experiments.

3.3.5 Modifications of the Continuum Model

Experiments and DEM simulations have provided us with considerable evidence that ice mélange imparts a fluctuation force on the glacier termini. The width averaged force can be on the order of 10^7 N/m [12, 15, 143], which is thought to be sufficient to inhibit the calving of new icebergs from glacier termini [11, 144–146]. The dynamics of the mélange can also control when glaciers calve [13, 17, 127]. Modelling efforts

have used discrete element modelling [4, 15, 143], modified ice sheet models[147] and simple paramaterizations [18–25] to quantify ice mélange's impact. However, a continuum granular description that can capture the dynamics of ice mélange and its coupling to the glacier-ocean system is still needed. Our continuum model is a first step, but it does not contain the necessary ingredients to be incorporated into coupled glacier-ocean models. The model needs to be able to couple mechanically and thermodynamically to both the glacier and the ocean, and it must include effects that come from the finite grain size of ice mélange. Recently, I have participated in a collaboration with Professor Jason Amundson and Professor Alex Robel on an implementation of non-local granular rheology [60, 67] to model ice mélange and its coupling with glacial calving and basal melt [5]. These modifications will violate our assumptions of quasistatic flow and zero strain rate. However, the mathematical framework of the model is effectively the same as our continuum model up until the introduction of the rheology. It starts with a depth integrated, viscoplastic rheology:

$$\tau_{ij} = \frac{\mu P}{\dot{\epsilon}_e}\dot{\epsilon}_{ij}, \tag{3.18}$$

where τ is the deviatoric stress, μ is an effective coefficient of friction, P is the total pressure, $\dot{\epsilon}$ is the strain rate, and $\dot{\epsilon}_e$ is the second invariant of the strain rate ($\dot{\epsilon}_e = \sqrt{1/2\,(Tr(\dot{\epsilon})^2 - Tr(\dot{\epsilon}\cdot\dot{\epsilon}))}$). Non-local granular rheologies depend on a parameter called the *granular fluidity* g', which modifies the effective friction coefficient, $\mu = \dot{\epsilon}_e/g'$. The fluidity adjusts the behaviour of the material depending on the amount of stress applied, and it incorporates both local and far away stresses [67]. The fluidity evolves based on a diffusion equation:

$$\nabla^2 g' = \frac{1}{\xi^2}(g' - g'_{loc}). \tag{3.19}$$

Here, ξ is the cooperativity length within the granular material, which determines the distance the fluidity spreads, and g'_{loc} is the local granular fluidity [67, 148]. Granular fluidity models ultimately depend on four parameters, the grain size d, the static yield stress μ_s, and two dimensionless coefficients A and b. Amundson et al. [5] shows the variability in mélange properties with choice of parameters in Fig. 3.15. The two most important panels are Fig. 3.15b and Fig. 3.15e, which show the mélange steady state thickness and across fjord velocity profiles respectively. The steady states developed here are a balance between calving rates, basal and surface melt of the mélange, and the rearrangments of the mélange. The fjord profiles are calculated at a distance halfway down the mélange length. Changing the static yield coefficient changes the point at which mélange can flow, and so decreasing it allows the mélange to speed up and thin. A is a quantification of the cooperativity length within a granular material, and is generally thought to be of order 1 [148–150]. Cooperativity length is a way to dictate how far we expect grains to interact, and for the default values here, it comes out to a few kilometers in the x direction. The dimensionless constant b is the ratio of the range of effective friction coefficients to the inertial number [148], and for this model increasing b creates a mélange that is thick, extensive, and rigid. Finally, it is hard to attribute a single characteristic grain size d in mélange, given that the consensus is that the iceberg sizes follow a power law distribution [2, 70]. Nevertheless, if d is reduced, then the mélange thins and speeds up. The model also predicts how the width average buttressing force scales with the granular fluidity. Equation 28 from Amundson et al. [5] says:

$$F/W = \left(-\frac{2H_0 \bar{P} \dot{\epsilon}_{xx}}{g^x + \dot{\epsilon}_{xx}} + H_0 \bar{P} \right) \tag{3.20}$$

where g^x is the fluidity for shear dominant flow in the x direction. Recalling the fact that the depth averaged pressure $\bar{P}$ scales as the thickness of the mélange H_0

(Eq. 3.12), we come back to the fact that the force mélange exerts on the glacier terminus scales as H_0^2. However, Amundson et al. [5] observes a slight decrease in the buttressing strength when basal melt and calving are nonzero, caused by extension of the mélange. They also find observe a sinusoidal variation in the basal melt rate, calving rate, and buttressing force, with a lag time between the two mass flux rates (melt and calving) and the buttressing force. But, the continuum model, now more robust and able to incorporate thermodynamic and mechanical coupling to the glacier-ocean system with a non-local granular rheology, still cannot account for the inherent fluctuations and stick slip behaviour of real ice mélange. Given that we know motion in the mélange precedes calving events only a few hours beforehand [14], these short term fluctuations and how to incorporate them into modelling efforts are an open area of investigation.

Chapter 4

Summary

This thesis has covered the experimental efforts I have undergone in understanding the dynamics of several geophysical flows. My focus was on flows where the particle shape mattered a lot, and where inertia is dissipated quickly, leading to long ranged correlations throughout the system. Using iterative design, a host of measurement techniques, and physical intuition, I have verified theoretical predictions and showcased unseen dynamics in mass-polar sediments and ice mélange. While these systems are ultimately two disparate phenomena, physics provides a way to understand them both through a similar framework. The main conclusions are summarized as follows:

4.1 Sedimentation of Mass-Polar Spheroids

Sedimentation has a long, storied history within fluid dynamics. It has a great deal of importance in both industrial and natural environments, and is tricky to understand due to the coupling between particles, fluids, and the long ranged hydrodynamics that arise from the Stokes equation. I conducted experiments to understand the role of mass distributions and particle shape in sedimenting suspensions. First, I studied the motion of a single particle in a quasi-2D environment. Using a simple analytic expression, I was able to reconstruct the particle's mobility matrix from a trajectory.

I then moved to characterizing the interaction between pairs of mass-polar sediments, and found a generic repulsion for prolate spheroids. The observed scaling with different center-of-mass offsets, χ, and particle aspect ratios, κ, confirmed the predictions made by Goldfriend et al. [41]. Finally, I calculated probability distributions of mass polar sediments in 3D environments, and found that the effective repulsion between particles persisted, and resulted in sedimented layers that are more uniform than non-mass polar sediments. There are several avenues to explore in the future. For instance, our particles are all non-chiral. Chiral particles have been shown to exhibit exotic, complex trajectories [42, 45, 46, 101, 112, 113], and can be implemented with our particle fabrication technique. Also, I was able to confirm the repulsive effect predicted by Goldfriend et al. [41], however the attractive prediction was not observed. Further efforts into creating oblate spheroids with non-zero χ are needed. While strong assumptions and approximations ultimately narrow the scope of the results, I have set a framework here for future experiments on the sedimentation of complex particles.

4.2 Quasistatic Flow of Ice Mélange

The interface between tidewater glaciers and the ocean will continue to be an important area to watch when monitoring sea level rise in the near future. Ice mélange is thus a crucial component of understanding the total mass flux of ice out of Greenlandic fjords. It is known that ice mélange provides a significant buttressing force to glacier termini, and can potentially inhibit and control calving rates [11, 12, 15, 143–146]. However, measurements of ice mélange in the field cannot yield the time evolution of its buttressing force, or direct visualizations of its thickness. Scaling down ice mélange into laboratory scale experiments allows for the observation of these measurements, and control over other parameters of the system, such as particle shape

and strength of wall friction. By examining thickness profiles, surface velocity fields, and time evolution of the buttressing strength, and comparing them to predictions made by a continuum depth and width averaged model, we deduced the following: the model predicts the average force ($F_0 \approx H_0^2$) well, but it cannot account for the stochasticity in the mélange, which can cause fluctuations in the force up to 50% of the mean. We explored several particle shapes and wall roughness, and determined that the continuum model works best when there is a large amount of shear generated in the mélange. By fitting the thickness profiles to predictions made by the continuum model (Eq. 3.15), we are able to extract a friction coefficient at the walls of the fjord. Comparing to friction coefficients measured outside of the model fjord, the model overestimates the friction. DEM simulations were performed by Meng et al. [4] to corroborate and confirm our results. Results show remarkable agreement, except between rectangular particles. The discrepancy is most likely caused by a limitation of the simulation software. The next step is to incorporate turbulent mixing of fresh, glacial water, and salty ocean water. Subglacial plumes [135], bring cold, fresh meltwater off the bottom of the glacier up through the mélange. The water turbulently mixes with the warm ocean water, which might change the dynamics and properties of the ice mélange. Adding this ingredient into our model fjord would provide an estimate the effect of sub-glacial plumes on the buttressing strength of ice mélange.

4.3 Conclusion

The work presented in this thesis incorporates a wide range of mathematical, experimental, and analytic techniques that have helped develop our understanding of geophysical phenomenon. The findings here can be used as a stepping stone towards a holistic model of geophysical flows of complex particulate matter. The physics which underpins much of this work has been studied for hundreds of years, but there are

always opportunities for new applications and perspectives which can advance our understanding of the natural world.

Bibliography

[1] Sediment sorting, Sep 2022. URL `https://www.nps.gov/teachers/classrooms/sediment-sorting.htm`.

[2] Daniel J Sulak, David A Sutherland, Ellyn M Enderlin, Leigh A Stearns, and Gordon S Hamilton. Iceberg properties and distributions in three greenlandic fjords using satellite imagery. *Annals of Glaciology*, 58(74):92–106, 2017.

[3] Anne Voigtländer, Morgane Houssais, Karol A. Bacik, Ian C. Bourg, Justin C. Burton, Karen E. Daniels, Sujit S. Datta, Emanuela Del Gado, Nakul S. Deshpande, Olivier Devauchelle, Behrooz Ferdowsi, Rachel Glade, Lucas Goehring, Ian J. Hewitt, Douglas Jerolmack, Ruben Juanes, Arshad Kudrolli, Ching-Yao Lai, Wei Li, Claire Masteller, Kavinda Nissanka, Allan M. Rubin, Howard A. Stone, Jenny Suckale, Nathalie M. Vriend, John S. Wettlaufer, and Judy Q. Yang. Soft matter physics of the ground beneath our feet, 2023.

[4] Yue Meng, Lai Ching-Yao, Riley Culberg, Michael G. Shahin, Leigh A. Stearns, Justin C. Burton, and Kavinda Nissanka. Seasonality of mélange thickness impacts calving dynamics in greenland. *Nature Communications*, 2024.

[5] Jason M. Amundson, Alex A. Robel, Justin C. Burton, and Kavinda Nissanka. A quasi-one-dimensional ice mélange flow model based on continuum descriptions of granular materials. *The Cryosphere*, 2024.

[6] Douglas J Jerolmack and Karen E Daniels. Viewing earth's surface as a soft-matter landscape. *Nature Reviews Physics*, 1(12):716–730, 2019.

[7] George Gabriel Stokes. *On the Effect of the Internal Friction of Fluids on the Motion of Pendulums*, page 1–10. Cambridge Library Collection - Mathematics. Cambridge University Press, 1851.

[8] Eckart Meiburg and Ben Kneller. Turbidity currents and their deposits. *Annual Review of Fluid Mechanics*, 42:135–156, 2010.

[9] Thomas G Pretlow and Theresa P Pretlow. Sedimentation for the separation of cells. *Methods*, 2(3):183–191, 1991.

[10] Anupam Sengupta, Francesco Carrara, and Roman Stocker. Phytoplankton can actively diversify their migration strategy in response to turbulent cues. *Nature*, 543:555 EP, 3 2017.

[11] Jason M Amundson, Mark Fahnestock, Martin Truffer, Jed Brown, Martin P Lüthi, and Roman J Motyka. Ice mélange dynamics and implications for terminus stability, jakobshavn isbræ, greenland. *Journal of Geophysical Research: Earth Surface*, 115(F1), 2010.

[12] J. M. Amundson and J. C. Burton. Quasi-static granular flow of ice mélange. *Journal of Geophysical Research: Earth Surface*, 123(9):2243–2257, 2018.

[13] Ryan Cassotto, Mark Fahnestock, Jason M Amundson, Martin Truffer, and Ian Joughin. Seasonal and interannual variations in ice melange and its impact on terminus stability, jakobshavn isbræ, greenland. *Journal of Glaciology*, 61(225): 76–88, 2015.

[14] Ryan K. Cassotto, Justin C. Burton, Jason M. Amundson, Mark A. Fahnestock, and Martin Truffer. Granular decoherence precedes ice mélange failure and

glacier calving at jakobshavn isbræ. *Nature Geoscience*, 14(6):417–422, Jun 2021. ISSN 1752-0908.

[15] Justin C. Burton, Jason M. Amundson, Ryan Cassotto, Chin-Chang Kuo, and Michael Dennin. Quantifying flow and stress in ice mélange, the world's largest granular material. *Proceedings of the National Academy of Sciences*, 115(20): 5105–5110, 2018.

[16] Twila Moon, Ian Joughin, and Ben Smith. Seasonal to multiyear variability of glacier surface velocity, terminus position, and sea ice/ice mélange in northwest greenland. *Journal of Geophysical Research: Earth Surface*, 120(5):818–833, 2015.

[17] Surui Xie, Timothy H. Dixon, David M. Holland, Denis Voytenko, and Irena Vaňková. Rapid iceberg calving following removal of tightly packed pro-glacial mélange. *Nature Communications*, 10(1):3250, Jul 2019. ISSN 2041-1723.

[18] Faezeh M Nick, Cornelis J Van der Veen, Andreas Vieli, and Douglas I Benn. A physically based calving model applied to marine outlet glaciers and implications for the glacier dynamics. *Journal of Glaciology*, 56(199):781–794, 2010.

[19] Andreas Vieli and Faezeh M Nick. Understanding and modelling rapid dynamic changes of tidewater outlet glaciers: issues and implications. *Surveys in geophysics*, 32:437–458, 2011.

[20] Susan Cook, IC Rutt, T Murray, A Luckman, T Zwinger, N Selmes, A Goldsack, and TD James. Modelling environmental influences on calving at helheim glacier in eastern greenland. *The Cryosphere*, 8(3):827–841, 2014.

[21] Joe Todd and Poul Christoffersen. Are seasonal calving dynamics forced by buttressing from ice mélange or undercutting by melting? outcomes from full-

stokes simulations of store glacier, west greenland. *The Cryosphere*, 8(6):2353–2365, 2014.

[22] J Krug, G Durand, O Gagliardini, and J Weiss. Modelling the impact of submarine frontal melting and ice mélange on glacier dynamics. *The Cryosphere*, 9(3):989–1003, 2015.

[23] Jamie Barnett, Felicity A Holmes, and Nina Kirchner. Modelled dynamic retreat of kangerlussuaq glacier, east greenland, strongly influenced by the consecutive absence of an ice mélange in kangerlussuaq fjord. *Journal of Glaciology*, 69(275):433–444, 2023.

[24] Joe Todd, Poul Christoffersen, Thomas Zwinger, Peter Råback, Nolwenn Chauché, Doug Benn, Adrian Luckman, Johnny Ryan, Nick Toberg, Donald Slater, et al. A full-stokes 3-d calving model applied to a large greenlandic glacier. *Journal of Geophysical Research: Earth Surface*, 123(3):410–432, 2018.

[25] Joe Todd, Poul Christoffersen, Thomas Zwinger, Peter Råback, and Douglas I Benn. Sensitivity of a calving glacier to ice–ocean interactions under climate change: new insights from a 3-d full-stokes model. *The Cryosphere*, 13(6): 1681–1694, 2019.

[26] GM Rodríguez-Liñán, R Torres-Orozco, VH Márquez, L Capra, and V Coviello. The physics of granular natural flows in volcanic environments. In *Mathematical and Computational Models of Flows and Waves in Geophysics*, pages 103–127. Springer, 2022.

[27] Nakul S Deshpande, David J Furbish, Paulo E Arratia, and Douglas J Jerolmack. The perpetual fragility of creeping hillslopes. *Nature Communications*, 12(1):3909, 2021.

[28] Nathan J. Mlot, Craig A. Tovey, and David L. Hu. Fire ants self-assemble into waterproof rafts to survive floods. *Proceedings of the National Academy of Sciences*, 108(19):7669–7673, 2011.

[29] Ian C Bourg and Jonathan B Ajo-Franklin. Clay, water, and salt: Controls on the permeability of fine-grained sedimentary rocks. *Accounts of chemical research*, 50(9):2067–2074, 2017.

[30] Osborne Reynolds. Xxix. an experimental investigation of the circumstances which determine whether the motion of water shall be direct or sinuous, and of the law of resistance in parallel channels. *Philosophical Transactions of the Royal society of London*, (174):935–982, 1883.

[31] Robert Spehar, Susan Cormier, and Debra Taylor. Caadis: Sediments, Mar 2023. URL `https://www.epa.gov/caddis-vol2/sediments`.

[32] Carmine Donatelli, Paola Passalacqua, Kyle Wright, Gerard Salter, Michael P Lamb, Daniel Jensen, and Sergio Fagherazzi. Quantifying flow velocities in river deltas via remotely sensed suspended sediment concentration. *Geophysical Research Letters*, 50(4):e2022GL101392, 2023.

[33] Sriram Ramaswamy. Issues in the statistical mechanics of steady sedimentation. *Adv. Phys.*, 50(3):297–341, 2001.

[34] Russel E. Caflisch and Jonathan H. C. Luke. Variance in the sedimentation speed of a suspension. *Phys. Fluids*, 28(3):759–760, 1985.

[35] Michael P. Brenner. Screening mechanisms in sedimentation. *Phys. Fluids*, 11 (4):754–772, 1999.

[36] Donald L. Koch and Eric S. G. Shaqfeh. The instability of a dispersion of sedimenting spheroids. *J. Fluid Mech.*, 209:521–542, 1989.

[37] Donald L. Koch and E. S. G. Shaqfeh. Screening in sedimenting suspensions. *J. Fluid Mech.*, 224:275–303, 1991.

[38] Nhan-Quyen Nguyen and Anthony Ladd. Sedimentation of hard-sphere suspensions at low reynolds number. *J. Fluid Mech.*, 525:73 – 104, 02 2005.

[39] Alex Levine, Sriram Ramaswamy, Erwin Frey, and Robijn Bruinsma. Screened and unscreened phases in sedimenting suspensions. *Phys. Rev. Lett.*, 81:5944–5947, 12 1998.

[40] P. J. Mucha, S. Y. Tee, D. A. Weitz, B. I. Shraiman, and M. P. Brenner. A model for velocity fluctuations in sedimentation. *J. Fluid Mech.*, 501:71–104, 2004. Times Cited: 60.

[41] Tomer Goldfriend, Haim Diamant, and Thomas A. Witten. Screening, hyperuniformity, and instability in the sedimentation of irregular objects. *Phys. Rev. Lett.*, 118:158005, 4 2017.

[42] Thomas A Witten and Haim Diamant. A review of shaped colloidal particles in fluids: anisotropy and chirality. *Rep. Prog. Phys.*, 83(11):116601, oct 2020.

[43] Rahul Chajwa, Narayanan Menon, and Sriram Ramaswamy. Kepler orbits in pairs of disks settling in a viscous fluid. *Phys. Rev. Lett.*, 122:224501, 6 2019.

[44] Rahul Chajwa, Narayanan Menon, Sriram Ramaswamy, and Rama Govindarajan. Waves, algebraic growth, and clumping in sedimenting disk arrays. *Phys. Rev. X*, 10:041016, Oct 2020.

[45] Nathan W. Krapf, Thomas A. Witten, and Nathan C. Keim. Chiral sedimentation of extended objects in viscous media. *Phys. Rev. E*, 79:056307, 5 2009.

[46] Masao Doi and Masato Makino. Sedimentation of particles of general shape. *Phys. Fluids*, 17(4):043601, 2005.

[47] Martina Palusa, Joost de Graaf, Aidan Brown, and Alexander Morozov. Sedimentation of a rigid helix in viscous media. *Phys. Rev. Fluids*, 3:124301, 12 2018.

[48] Piotr Migoń. Geomorphology of conglomerate terrains–global overview. *Earth-Science Reviews*, 208:103302, 2020.

[49] B Cichocki and K Hinsen. Stokes drag on conglomerates of spheres. *Physics of Fluids*, 7(2):285–291, 1995.

[50] Rajendra P Chhabra. Non-newtonian fluids: an introduction. *Rheology of complex fluids*, pages 3–34, 2010.

[51] Charles S Campbell. Granular shear flows at the elastic limit. *Journal of fluid mechanics*, 465:261–291, 2002.

[52] Pierre Jop, Yoël Forterre, and Olivier Pouliquen. A constitutive law for dense granular flows. *Nature*, 441(7094):727–730, 2006.

[53] MB Geilikman, MB Dusseault, and FA Dullien. Sand production as a viscoplastic granular flow. In *SPE International Conference and Exhibition on Formation Damage Control*, pages SPE–27343. SPE, 1994.

[54] Kaiqiao Wu, Victor Francia, and Marc-Olivier Coppens. Dynamic viscoplastic granular flows: A persistent challenge in gas-solid fluidization. *Powder Technology*, 365:172–185, 2020.

[55] Pierre Jop, Yoël Forterre, and Olivier Pouliquen. Initiation of granular surface flows in a narrow channel. *Physics of Fluids*, 19(8), 2007.

[56] Robert P Behringer and Bulbul Chakraborty. The physics of jamming for granular materials: a review. *Reports on Progress in Physics*, 82(1):012601, 2018.

[57] AL Thomas, Zhu Tang, Karen E Daniels, and NM Vriend. Force fluctuations at the transition from quasi-static to inertial granular flow. *Soft Matter*, 15(42): 8532–8542, 2019.

[58] Georg Koval, Jean-Noël Roux, Alain Corfdir, and François Chevoir. Annular shear of cohesionless granular materials: From the inertial to quasistatic regime. *Physical Review E*, 79(2):021306, 2009.

[59] Johan Gaume, Guillaume Chambon, and Mohamed Naaim. Quasistatic to inertial transition in granular materials and the role of fluctuations. *Physical Review E*, 84(5):051304, 2011.

[60] Ken Kamrin. Non-locality in granular flow: Phenomenology and modeling approaches. *Frontiers in Physics*, 7, 2019. ISSN 2296-424X.

[61] Frédéric Da Cruz, Sacha Emam, Michaël Prochnow, Jean-Noël Roux, and François Chevoir. Rheophysics of dense granular materials: Discrete simulation of plane shear flows. *Physical Review E*, 72(2):021309, 2005.

[62] KA Reddy, Yoel Forterre, and O Pouliquen. Evidence of mechanically activated processes in slow granular flows. *Physical Review Letters*, 106(10):108301, 2011.

[63] Teruhisa S Komatsu, Shio Inagaki, Naoko Nakagawa, and Satoru Nasuno. Creep motion in a granular pile exhibiting steady surface flow. *Physical review letters*, 86(9):1757, 2001.

[64] GDR MiDi gdrmidi@ polytech. univ-mrs. fr http://www. lmgc. univ-montp2. fr/MIDI/. On dense granular flows. *The European Physical Journal E*, 14: 341–365, 2004.

[65] Daniel M Mueth. Measurements of particle dynamics in slow, dense granular couette flow. *Physical Review E*, 67(1):011304, 2003.

[66] Zhu Tang, Theodore A Brzinski, Michael Shearer, and Karen E Daniels. Nonlocal rheology of dense granular flow in annular shear experiments. *Soft matter*, 14(16):3040–3048, 2018.

[67] Ken Kamrin and Georg Koval. Nonlocal constitutive relation for steady granular flow. *Physical review letters*, 108(17):178301, 2012.

[68] Mehdi Bouzid, Adrien Izzet, Martin Trulsson, Eric Clément, Philippe Claudin, and Bruno Andreotti. Non-local rheology in dense granular flows: Revisiting the concept of fluidity. *The European Physical Journal E*, 38:1–15, 2015.

[69] Olivier Pouliquen. Velocity correlations in dense granular flows. *Physical review letters*, 93(24):248001, 2004.

[70] Ellyn M Enderlin, Gordon S Hamilton, Fiammetta Straneo, and David A Sutherland. Iceberg meltwater fluxes dominate the freshwater budget in greenland's iceberg-congested glacial fjords. *Geophysical Research Letters*, 43(21): 11–287, 2016.

[71] Emlyn H Koster, Ron J Steel, et al. *Sedimentology of gravels and conglomerates*, volume 10. Canadian Society of Petroleum Geologists Calgary, 1984.

[72] Sabrina Bonetto, Cesare Comina, Chiara Colombero, Francesco Dela Pierre, Anna Maria Ferrero, Nicolò Giordano, Andrea Rispoli, and Federico Vagnon. Study of the mechanical properties of a conglomerate. *Procedia Engineering*, 158:248–253, 2016.

[73] Gábor Domokos, Douglas J. Jerolmack, Ferenc Kun, and János Török. Plato's cube and the natural geometry of fragmentation. *Proc. Natl. Acad. Sci. U.S.A.*, 117(31):18178–18185, 2020. ISSN 0027-8424.

[74] Scott V Franklin and Mark D Shattuck. *Handbook of granular materials*. CRC Press, 2016.

[75] Nakul S. Deshpande and Benjamin T. Crosby. Logjams are not jammed: measurements of log motions in big creek, idaho, 2019.

[76] J Yang and XD Luo. Exploring the relationship between critical state and particle shape for granular materials. *Journal of the Mechanics and Physics of Solids*, 84:196–213, 2015.

[77] Eric Deal, Jeremy G Venditti, Santiago J Benavides, Ryan Bradley, Qiong Zhang, Ken Kamrin, and J Taylor Perron. Grain shape effects in bed load sediment transport. *Nature*, 613(7943):298–302, 2023.

[78] J F Brady and G Bossis. Stokesian dynamics. *Annu. Rev. Fluid Mech.*, 20(1): 111–157, 1988.

[79] Imre M. Jánosi, Tamás Tél, Dietrich E. Wolf, and Jason A. C. Gallas. Chaotic particle dynamics in viscous flows: The three-particle stokeslet problem. *Phys. Rev. E*, 56:2858–2868, Sep 1997.

[80] M. L. Ekiel-Jeżewska and B. U. Felderhof. Periodic sedimentation of three particles in periodic boundary conditions. *Phys. Fluids*, 17(9):093102, 2005.

[81] Sunghwan Jung, S. E. Spagnolie, K. Parikh, M. Shelley, and A-K. Tornberg. Periodic sedimentation in a stokesian fluid. *Phys. Rev. E*, 74:035302, 9 2006.

[82] Ivan L. Claeys and John F. Brady. Suspensions of prolate spheroids in stokes flow. part 1. dynamics of a finite number of particles in an unbounded fluid. *Journal of Fluid Mechanics*, 251:411–442, 1993.

[83] Scott V Franklin. Geometric cohesion in granular materials. *Physics today*, 65 (9):70–71, 2012.

[84] Mohammad Ali Maroof, Ahmad Mahboubi, Ali Noorzad, and Yaser Safi. A new approach to particle shape classification of granular materials. *Transportation Geotechnics*, 22:100296, 2020.

[85] Hoang Bao Khoi Nguyen, Md Mizanur Rahman, and Andy B Fourie. How particle shape affects the critical state, triggering of instability and dilatancy of granular materials–results from a dem study. *Géotechnique*, 71(9):749–764, 2021.

[86] Ahmed Hafez, Qi Liu, Thomas Finkbeiner, Raed A Alouhali, Timothy E Moellendick, and J Carlos Santamarina. The effect of particle shape on discharge and clogging. *Scientific reports*, 11(1):3309, 2021.

[87] Athanasios G Athanassiadis, Marc Z Miskin, Paul Kaplan, Nicholas Rodenberg, Seung Hwan Lee, Jason Merritt, Eric Brown, John Amend, Hod Lipson, and Heinrich M Jaeger. Particle shape effects on the stress response of granular packings. *Soft Matter*, 10(1):48–59, 2014.

[88] Kavinda Nissanka, Xiaolei Ma, and Justin C Burton. Dynamics of mass polar spheroids during sedimentation. *Journal of Fluid Mechanics*, 956:A28, 2023.

[89] J.-Z. Xue, E. Herbolzheimer, M. A. Rutgers, W. B. Russel, and P. M. Chaikin. Diffusion, dispersion, and settling of hard spheres. *Phys. Rev. Lett.*, 69:1715–1718, Sep 1992.

[90] Élisabeth Guazzelli, Jeffrey F. Morris, and Sylvie Pic. *A Physical Introduction to Suspension Dynamics*. Cambridge Texts in Applied Mathematics. Cambridge University Press, 2011.

[91] Pedro Monroy, Gabor Drótos, Emilio Hernández-García, and Cristóbal López. Spatial inhomogeneities in the sedimentation of biogenic particles in ocean flows:

Analysis in the benguela region. *J. Geophys. Res. Oceans*, 124(7):4744–4762, 2019.

[92] G. K. Batchelor. Sedimentation in a dilute dispersion of spheres. *J. Fluid Mech.*, 52(2):245–268, 1972.

[93] Anthony J. C. Ladd. Hydrodynamic screening in sedimenting suspensions of non-brownian spheres. *Phys. Rev. Lett.*, 76:1392–1395, 2 1996.

[94] Anthony J. C. Ladd. Sedimentation of homogeneous suspensions of non-brownian spheres. *Phys. Fluids*, 9(3):491–499, 1997.

[95] F. R. Cunha, G. C. Abade, A. J. Sousa, and E. J. Hinch. Modeling and Direct Simulation of Velocity Fluctuations and Particle-Velocity Correlations in Sedimentation . *J. Fluids Eng.*, 124(4):957–968, 12 2002. ISSN 0098-2202.

[96] Donald L. Koch. Hydrodynamic diffusion in dilute sedimenting suspensions at moderate reynolds numbers. *Phys. Fluids A: Fluid Dynamics*, 5(5):1141–1155, 1993.

[97] Donald L. Koch. Hydrodynamic diffusion in a suspension of sedimenting point particles with periodic boundary conditions. *Phys. Fluids*, 6(9):2894–2900, 1994.

[98] Hélène Nicolai and Elisabeth Guazzelli. Effect of the vessel size on the hydrodynamic diffusion of sedimenting spheres. *Phys. Fluids*, 7(1):3–5, 1995.

[99] P. N. Segrè, E. Herbolzheimer, and P. M. Chaikin. Long-range correlations in sedimentation. *Phys. Rev. Lett.*, 79:2574–2577, 9 1997.

[100] J.M. Ham and G.M. Homsy. Hindered settling and hydrodynamic dispersion in quiescent sedimenting suspensions. *Int. J. Multiph. Flow*, 14(5):533 – 546, 1988. ISSN 0301-9322.

[101] Tomer Goldfriend, Haim Diamant, and Thomas A. Witten. Hydrodynamic interactions between two forced objects of arbitrary shape. i. effect on alignment. *Phys. Fluids*, 27(12):123303, 2015.

[102] Tomer Goldfriend, Haim Diamant, and Thomas A. Witten. Hydrodynamic interactions between two forced objects of arbitrary shape. ii. relative translation. *Phys. Rev. E*, 93:042609, Apr 2016.

[103] Johannes Schindelin, Ignacio Arganda-Carreras, Erwin Frise, Verena Kaynig, Mark Longair, Tobias Pietzsch, Stephan Preibisch, Curtis Rueden, Stephan Saalfeld, Benjamin Schmid, Jean-Yves Tinevez, Daniel James White, Volker Hartenstein, Kevin Eliceiri, Pavel Tomancak, and Albert Cardona. Fiji: an open-source platform for biological-image analysis. *Nature Methods*, 9(7):676–682, 2012. ISSN 1548-7105.

[104] Daniel B. Allan, Thomas Caswell, Nathan C. Keim, Casper M. van der Wel, and Ruben W. Verweij. soft-matter/trackpy: Trackpy v0.5.0, 2021.

[105] Tsevi Beatus, Roy H. Bar-Ziv, and Tsvi Tlusty. The physics of 2d microfluidic droplet ensembles. *Physics Reports*, 516(3):103–145, 2012. ISSN 0370-1573. The physics of 2D microfluidic droplet ensembles.

[106] William Mitchell and Saverio Spagnolie. Sedimentation of spheroidal bodies near walls in viscous fluids: glancing, reversing, tumbling, and sliding. *J. Fluid Mech.*, 772:600–629, 09 2014.

[107] Maria Veronica D'Angelo, Mario Cachile, Jean-Pierre Hulin, and Harold Auradou. Sedimentation and fluttering of a cylinder in a confined liquid. *Phys. Rev. Fluids*, 2:104301, Oct 2017.

[108] Bram Bet, Sela Samin, Rumen Georgiev, Huseyin Burak Eral, and René van

Roij. Steering particles by breaking symmetries. *Journal of Physics: Condensed Matter*, 30(22):224002, may 2018.

[109] Rumen N. Georgiev, Sara O. Toscano, William E. Uspal, Bram Bet, Sela Samin, René van Roij, and Huseyin Burak Eral. Universal motion of mirror-symmetric microparticles in confined stokes flow. *Proc. Natl. Acad. Sci. U.S.A.*, 117(36): 21865–21872, 2020. ISSN 0027-8424.

[110] Maria L Ekiel-Jeżewska and Eligiusz Wajnryb. Hydrodynamic orienting of asymmetric microobjects under gravity. *Journal of Physics: Condensed Matter*, 21(20):204102, apr 2009.

[111] J Garcia de la Torre and B Carrasco. Hydrodynamic properties of rigid macromolecules composed of ellipsoidal and cylindrical subunits. *Biopolymers: Original Research on Biomolecules*, 63(3):163–167, 2002.

[112] O Gonzalez, ABA Graf, and JH Maddocks. Dynamics of a rigid body in a stokes fluid. *Journal of Fluid Mechanics*, 519:133–160, 2004.

[113] Brian Moths and TA Witten. Full alignment of colloidal objects by programed forcing. *Physical review letters*, 110(2):028301, 2013.

[114] J. T. Padding and W. J. Briels. Translational and rotational friction on a colloidal rod near a wall. *J. Chem. Phys.*, 132(5):054511, 2010.

[115] Tim van Emmerik and Anna Schwarz. Plastic debris in rivers. *WIREs Water*, 7(1):e1398, 2020.

[116] Lia Papadopoulos, Mason A Porter, Karen E Daniels, and Danielle S Bassett. Network analysis of particles and grains. *Journal of Complex Networks*, 6(4): 485–565, 04 2018. ISSN 2051-1329.

[117] Daniel W. Howell, R. P. Behringer, and C. T. Veje. Fluctuations in granular media. *Chaos: An Interdisciplinary Journal of Nonlinear Science*, 9(3):559–572, 09 1999. ISSN 1054-1500.

[118] Cristian F. Moukarzel. Isostatic phase transition and instability in stiff granular materials. *Phys. Rev. Lett.*, 81:1634–1637, Aug 1998.

[119] Leah K. Roth, Endao Han, and Heinrich M. Jaeger. Intrusion into granular media beyond the quasistatic regime. *Phys. Rev. Lett.*, 126:218001, May 2021.

[120] Karen E. Daniels, Jonathan E. Kollmer, and James G. Puckett. Photoelastic force measurements in granular materials. *Review of Scientific Instruments*, 88 (5):051808, 05 2017. ISSN 0034-6748.

[121] Robert Ettema. Jam initiation in unobstructed channels: laboratory observations. *Journal of Hydraulic Research*, 28(6):673–684, 1990.

[122] Agnieszka Herman. Numerical modeling of force and contact networks in fragmented sea ice. *Annals of Glaciology*, 54(62):114–120, 2013.

[123] Martin Jutzeler, Robert Marsh, Rebecca J Carey, James D L White, Peter J Talling, and Leif Karlstrom. On the fate of pumice rafts formed during the 2012 havre submarine eruption. *Nature communications*, 5:3660, April 2014. ISSN 2041-1723.

[124] RB Alley, KM Cuffey, JN Bassis, KE Alley, S Wang, BR Parizek, S Anandakrishnan, K Christianson, and RM DeConto. Iceberg calving: Regimes and transitions. *Annual Review of Earth and Planetary Sciences*, 51:189–215, 2023.

[125] Youngmin Choi, Mathieu Morlighem, Eric Rignot, and Michael Wood. Ice dynamics will remain a primary driver of greenland ice sheet mass loss over the next century. *Communications Earth & Environment*, 2(1):26, 2021.

[126] J. Todd, P. Christoffersen, T. Zwinger, P. Råback, and D. I. Benn. Sensitivity of a calving glacier to ice–ocean interactions under climate change: new insights from a 3-d full-stokes model. *The Cryosphere*, 13(6):1681–1694, 2019.

[127] Ian Joughin, David E Shean, Benjamin E Smith, and Dana Floricioiu. A decade of variability on jakobshavn isbræ: ocean temperatures pace speed through influence on mélange rigidity. *The Cryosphere*, 14(1):211–227, 2020.

[128] Zhong Zheng, Herbert E. Huppert, Nathalie M. Vriend, Jerome A. Neufeld, and P. F. Linden. Flow of buoyant granular materials along a free surface. *Journal of Fluid Mechanics*, 848:312–339, 2018.

[129] S. B. Savage and K. Hutter. The motion of a finite mass of granular material down a rough incline. *Journal of Fluid Mechanics*, 199:177–215, 1989.

[130] Gert Lube, Herbert E. Huppert, R. Stephen J. Sparks, and Mark A. Hallworth. Axisymmetric collapses of granular columns. *Journal of Fluid Mechanics*, 508: 175–199, 2004.

[131] Guido Van Rossum and Fred L Drake Jr. *Python reference manual*. Centrum voor Wiskunde en Informatica Amsterdam, 1995.

[132] G. Bradski. The OpenCV Library. *Dr. Dobb's Journal of Software Tools*, 2000.

[133] J. C. Burton, J. M. Amundson, D. S. Abbot, A. Boghosian, L. M. Cathles, S. Correa-Legisos, K. N. Darnell, N. Guttenberg, D. M. Holland, and D. R. MacAyeal. Laboratory investigations of iceberg-capsize dynamics, energy dissipation, and tsunamigenesis. *J. Geophys. Res.*, 117(F01007), 2012. https://doi.org/10.1029/2011JF002055.

[134] Jason M Amundson, Justin C Burton, and Sergio Correa-Legisos. Impact of

hydrodynamics on seismic signals generated by iceberg collisions. *Annals of Glaciology*, 53(60):106–112, 2012.

[135] Rebecca H Jackson, Roman J Motyka, Jason M Amundson, Nicole Abib, David A Sutherland, Jonathan D Nash, and Christian Kienholz. The relationship between submarine melt and subglacial discharge from observations at a tidewater glacier. *Journal of Geophysical Research: Oceans*, 127(10): e2021JC018204, 2022.

[136] E. Lajeunesse, A. Mangeney-Castelnau, and J. P. Vilotte. Spreading of a granular mass on a horizontal plane. *Physics of Fluids*, 16(7):2371–2381, 05 2004. ISSN 1070-6631.

[137] Douglas R MacAyeal. Large-scale ice flow over a viscous basal sediment: Theory and application to ice stream b, antarctica. *Journal of Geophysical Research: Solid Earth*, 94(B4):4071–4087, 1989.

[138] HA Janssen. Versuche uber getreidedruck in silozellen. *Z. ver. deut. Ing.*, 39: 1045, 1895.

[139] EM Enderlin and GS Hamilton. Estimates of iceberg submarine melting from high-resolution digital elevation models: application to sermilik fjord, east greenland. *Journal of Glaciology*, 60(224):1084–1092, 2014.

[140] Ivo R Peters, Jason M Amundson, Ryan Cassotto, Mark Fahnestock, Kristopher N Darnell, Martin Truffer, and Wendy W Zhang. Dynamic jamming of iceberg-choked fjords. *Geophysical Research Letters*, 42(4):1122–1129, 2015.

[141] John Leeman, Marco Maria Scuderi, Chris Marone, and Demian Saffer. Stiffness evolution of granular layers and the origin of repetitive, slow, stick-slip frictional sliding. *Granular Matter*, 17:447–457, 2015.

[142] Khalid A. Alshibli and Lynne E. Roussel. Experimental investigation of slip-stick behaviour in granular materials. *International journal for numerical and analytical methods in geomechanics*, 30(14):1391–1407, 2006.

[143] Alexander A. Robel. Thinning sea ice weakens buttressing force of iceberg mélange and promotes calving. *Nature Communications*, 8(1):14596, Mar 2017. ISSN 2041-1723.

[144] JN Bassis, B Berg, AJ Crawford, and DI Benn. Transition to marine ice cliff instability controlled by ice thickness gradients and velocity. *Science*, 372(6548): 1342–1344, 2021.

[145] Tanja Schlemm, Johannes Feldmann, Ricarda Winkelmann, and Anders Levermann. Stabilizing effect of mélange buttressing on the marine ice-cliff instability of the west antarctic ice sheet. *The Cryosphere*, 16(5):1979–1996, 2022.

[146] Anna J Crawford, Douglas I Benn, Joe Todd, Jan A Åström, Jeremy N Bassis, and Thomas Zwinger. Marine ice-cliff instability modeling shows mixed-mode ice-cliff failure and yields calving rate parameterization. *Nature communications*, 12(1):2701, 2021.

[147] D. Pollard, R. M. DeConto, and R. B. Alley. A continuum model (PSUMEL1) of ice mélange and its role during retreat of the Antarctic Ice Sheet. *Geosci. Model Dev.*, 11:5149–5172, 2018.

[148] K. Kamrin and D. L. Henann. Nonlocal modeling of granular flows down inclines. *Soft Matter*, 11(179), 2015.

[149] K. Kamrin and G. Koval. Effect of particle surface friction on nonlocal constitutive behavior of flowing granular media. *Comp. Part. Mech.*, 1:169–176, 2014.

[150] D. L. Henann and K. Kamrin. A predictive, size-dependent continuum model for dense granular flows. *Proc. Nat. Acad. Sci.*, 110(17):6730–6735, 2013.